PhD degree in Medical Nanotechnology

European School of Molecular Medicine (SEMM)

University of Milan (Italy)

Cycle XXVII

Development of biodegradable nanoparticles for targeting Tumor Associated Macrophages: synthesis, investigation of the role of the surfactant and surface decoration in complex media

Cella Claudia

Matricola n. R09890

Supervisor: *Lenardi Cristina, PhD,* University of Milan (Italy)

Internal advisor: Milani Paolo, PhD, University of Milan (Italy)

External advisor: Richardson Simon, PhD, University of Greenwich (UK)

Academic Year: 2015-2016

Table of contents

List of abbreviations

100FBS: 100% v/v FBS

100FBSM: mixture 100% v/v FBS with 20% w/v D-mannose

^{1}HNMR: Proton nuclear magnetic resonance

Ag: antigen

APS: ammonium persulfate

CD4-FITC: monoclonal anti-human CD4-FITC conjugate

CSt: calcium stearate

DCM: Dichloromethane

DCR: derived count rate

DCS: differential centrifugal sedimentation

DLS: Dynamic Light Scattering

DMAPMA: N-(3-(dimethylamino)propyl)methacrylamid

DMEM: Dulbecco minimal essential medium

DMSO: Dimethyl sulfoxide

dsRNA: double-stranded ribonucleic acid

EPR: enhanced permeability and retention effect

EtOH: ethanol

FBS (Results and discussion, paragraph 5. D-Mannose and protein corona decorations page 111):

10% v/v FBS

FBS: Fetal Bovine Serum

FBSM: mixture 10% v/v FBS with 20% w/v D-mannose

FDA: Food and drug administration

FFF: Field Flow Fractionaction

Fib-647: fibrinogen from human plasma Alexa Fluor® 647 conjugate

FITC: Fluorescein isothiocyanate

FT-IR: Fourier-transform infrared spectroscopy

h: hours

IC: immune complexes

IgG1-488: Alexa Fluor® 488 goat anti-mouse IgG1

IgG1-Cy3: Cy™3 AffiniPure Goat Anti-Mouse IgG (H+L)

IL: interleukin

IR: infrared region

M: 20% w/v D-mannose

m: medium refractive index

MDSC: myeloid-derived suppressor cells

min: minutes

MPS: mononuclear phagocyte system

mRNA: messenger ribonucleic acid

MTT: [3-(4,5-dimethylthiazol-2-yl)-2,5-diphenyltetrazolium bromide]

MW: molecular weight

NA: not available

NMs: nanomaterials

NPs: nanoparticles

OW: oil-in-water

P60: Polysorbate 60

PBS: Phosphate Buffer Saline

pdI: polydispersity index

PLGA: Poly(Lactide-co-Glycolide)acid

PSD: particle size distribution

PVA: Poly(Vinyl) Alcohol

RID: refractive index distribution

RISC: RNA-induced silencing complex

RNA: ribonucleic acid

RNAi: ribonucleic acid interference

rpm: rotation per minute

S60: Span 60®

sec: seconds

SEM: Scanning Electron Microscopy

siRNA: small interfering ribonucleic acid

SPES: single particle extinction and scattering

STED: stimulated emission depletion

TAMs: Tumor Associated Macrophages

TNFα: tumor necrosis factor

UT: untreated

UV-Vis: UV-visible

v/v: volume/volume

vRNA: vegetal ribonucleic acid

w/v: weight/volume

WOW: water-in-oil-in-water

XPS: X-ray Photoelectron Spectroscopy

z-ave: z-average

Additional abbreviations in Appendix 2

AgNPs: silver nanoparticles

CT: citrate

F10: 10% v/v Fetal Bovine Serum

F100: 100% v/v Fetal Bovine Serum

MP: mouse plasma

np: not reported

PVP: Polyvinylpyrrolidone

RT: room temperature

SPR: surface plasmon resonance

TEM: Transmission Electron Microscopy

Figures Index

Tables index

Abstract

Tumor Associated Macrophages (TAMs) are involved in cancer proliferation, thus strategies to deplete them represent promising tools for chemotherapy. Pharmacological agents with multiple activities such as curcumin and RNA interference have been proposed; however their employment in therapeutics has been limited because of low systemic bioavailability. Accordingly, this thesis described as an innovative therapeutic approach for cancer treatment the development of polymeric nanoparticles (NPs) able to (i) increase pharmacokinetics properties of biomacromolecules and poor water soluble drugs, and (ii) guarantee TAMs specific targeting.

The safe and versatile polymer Poly(Lactic-co-Glycolic)Acid (PLGA) has been used for the synthesis of NPs by both single (OW) and double (WOW) emulsion-solvent evaporation techniques. Different synthetic parameters have been taken into consideration, with particular focus on the surfactant role. As alternative to the commonly used Poly Vinyl Alcohol (PVA), a newly synthetized polymer (amino-PVA) and Calcium Sterate (CSt) have been investigated for their ability to modulate surface charge and biocompatibility. NPs with solid or core-shell structures, whose size was tailored between 200 and 300 nm, were obtained and a thorough characterization has been performed, with the help of innovative techniques such as single particle optical extinction and scattering (SPES) method. Both amino-PVA and CSt stabilized NPs were found to be able to load curcumin and biomacromolecules, either alone or in combination. Strategies for surface decoration with the employment of D-mannose as specific molecule to guarantee TAMs recognition were proposed. Finally, cytocompatibility of the amino-PVA and CSt stabilized NPs have been assessed.

Introduction

1. The clinical need: Tumor Associated Macrophages and cancer treatment

1.1 TAMs role in tumor development

Macrophages are resident phagocytes originating from blood monocytes. They are widely distributed in tissues, where they are active both as immune effectors cells with a broad microbial recognition capacity, and as housekeeping phagocytes responsible for maintenance of tissue integrity[1]. In terms of both phenotype and gene expression programs, macrophages display a striking heterogeneity that reflects on the one hand the specialization of tissue macrophages in the microenvironment of tissues as different as liver, brain, spleen and many others; and on the other the dynamic changes in their physiology that occur after they come in contact with microbial stimuli or endogenous stress signals (*i.e.* necrotic cells). Therefore the generic definition of macrophages comprises a variety of cells with different functions and functional states that are specified by the complex interplay between micro-environmental signals and a general, robust differentiation program that determines macrophage identity[1]. In fact, macrophages are polarized following activation into classic inflammatory (M1) or alternatively activated (M2) programs. M1 cells are activated in response to microbial products and tumor necrosis factor (TNFα), and are characterized by a strong propensity to present antigen (Ag). In a polarized response,M1 cells are thought to kill intracellular micro-organisms and produce abundant pro-inflammatory cytokines TNFα, interleukin (IL-12, IL-23), and pro-inflammatory mediators. On the other hand, alternatively activated M2 cells are promoted by various signals such as IL-4, IL-13, glucocorticoids, IL-10, immune complexes (IC) which drive autoimmune diseases and some pathogen associated molecular patterns. Their mainly characteristics include phagocytic activity, production of ornithine and polyamines, high expression of scavenging molecules, as well as the expression of mannose and galactose receptors on their surface. Their functions are to resolve inflammation

and promote angiogenesis and tissue remodeling (Fig. 1). Differences between M1 and M2 macrophages also include their chemokine expression profiles[2–6].

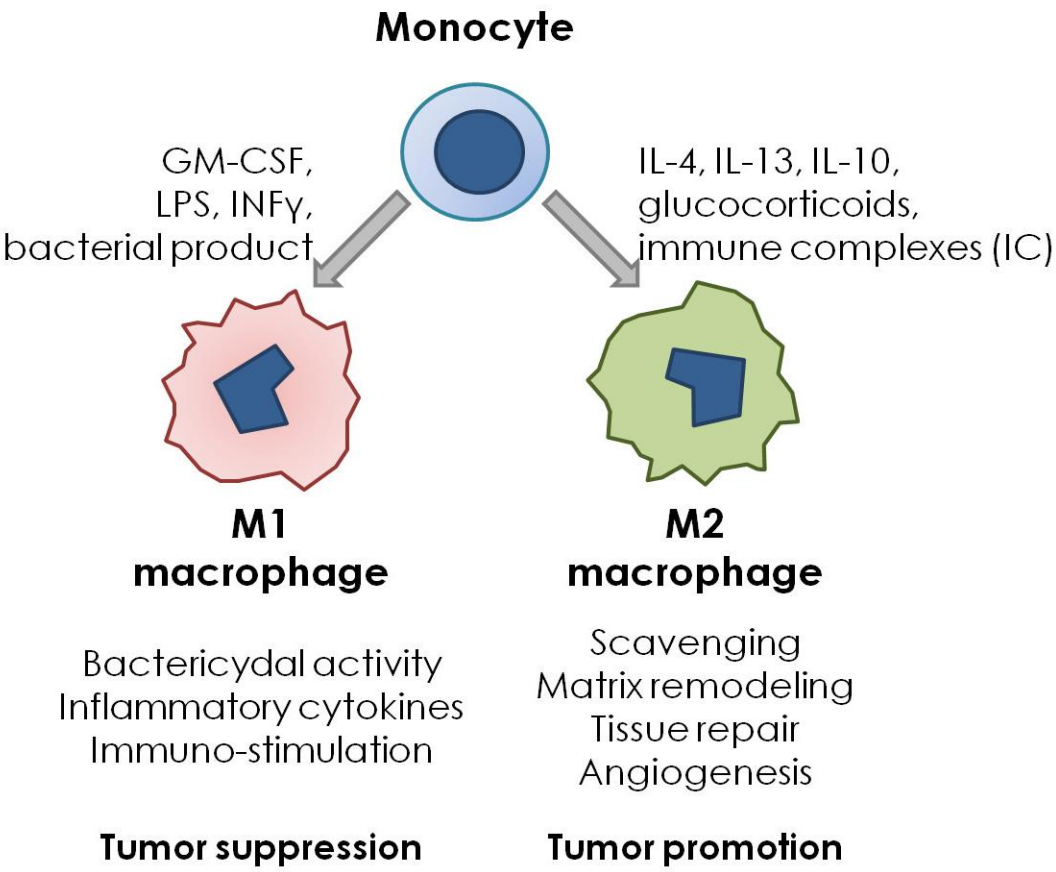

Fig. 1. Monocyte differentiation towards M1 and M2 phenotype. The scheme underlines factors involved in monocyte differentiation, as well as M1 and M2 physiological role.

In the context of solid tumors, bidirectional communication between cells and their microenvironment as well as the coordinated intercellular interactions are disrupted and modified. By the release of cytokines, chemokines and other molecules, tumor can educate cells to acquire pro-tumorigenic functions, and in turn the microenvironment evolves to accommodate the tumor growing[7,8].

When cancer development is related with inflammation, recruitment to tumor tissues of cells of the monocyte-macrophage lineage occurs[3,9,10]. This influence also the premetastatic niche and promote secondary localization of cancer[2]. The different growth factors and chemokines secreted by cancer cells determine a change in macrophage phenotypes[1]. In this pathological context,

Mantovani *et al.*[11] have originally proposed the role of infiltrating leukocytes in facilitating tumor growth and progression. Nowadays it is well assessed that tumor cell products, including extracellular matrix components, IL-10, CSF-1, and chemokines (CCL2, CCL18, CCL17, and CXCL4), switch macrophages phenotype into a M2-like, thus promoting Tumor Associated Macrophages (TAMs) formation. TAMs are characterized by low IL-12 and high IL-10 expression. They exert a cancer-promoting behavior by presenting low tumoricidal activity and contemporary promotion of tissue remodeling and angiogenesis[2,9] (Fig.2). In addition, TAM infiltration has been associated with poor prognosis, as shown in Hodgkin disease, glioma, cholangiocarcinoma, and breast carcinoma[2,12,13].

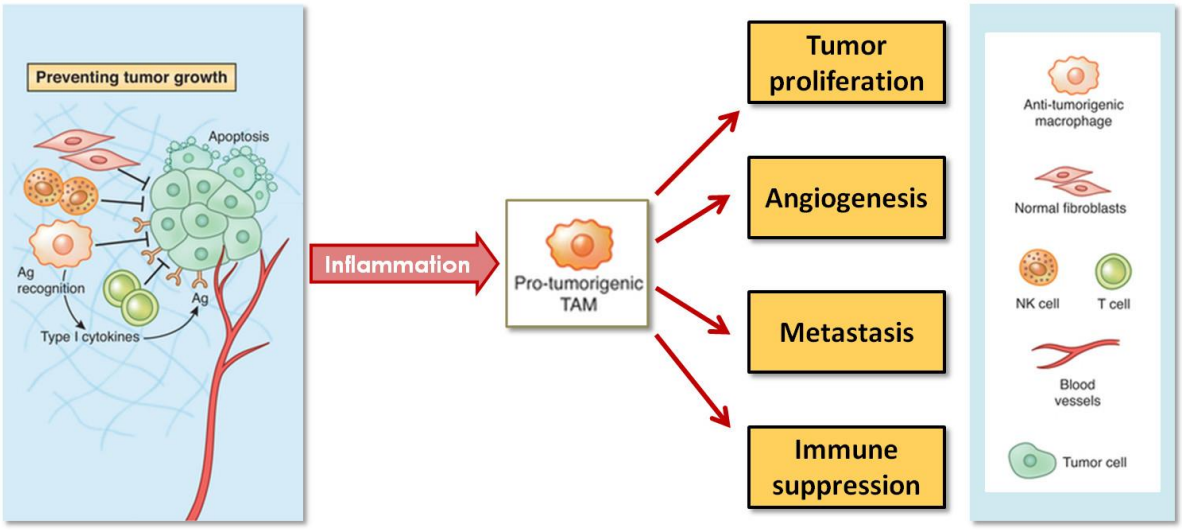

Fig.2. **Tumor Associated Macrophages role in tumor development (adapted from[7]).** In a tumor environment, inflammation can promote Tumor Associated Macrophages (TAMs) formation, thus inducing tumor proliferation, angiogenesis, metastasis formation and immune suppression (Ag, antigen; NK, natural killer).

1.2 TAMs are a promising target for cancer treatment

Since TAMs are so deeply involved in the pathology of cancer proliferation, strategies to deplete them or to inhibit their recruitment into neoplastic lesions have been investigated and some

successes in experimental settings have been obtained[2,12,14–18]. Indeed, when their density in tumor tissues was reduced, a marked decrease in the presence of pro-tumor growth and angiogenic factors (such as TGF-β, TNF-α, MMP-9, and VEGF) was observed. This consequently inhibited tumor angiogenesis, growth and metastasis[18].

In addition, macrophages represent a good target because their stable genome is not likely to develop drug resistance[19].

So far, no specific drugs are available for TAMs targeting, with the except of trabectedin that is authorized only in the secondary treatment of soft tissue sarcoma and relapsed platinum-sensitive ovarian cancer[17,20–22]. Moreover, cost of trabectedin as primary therapy was found to be higher than the combination doxorubicin/ifosfamide, thus supporting the recommendation that trabected in should remain a second-line treatment[23].

1.3 Possible alternative strategies for TAMs targeting

1.3.1 Curcumin

Curcumin (diferuloylmethane) is a polyphenol (Fig.3) and constitutes the mainactive principle of the perennial herb *Curcuma longa* (also called turmeric)[24].

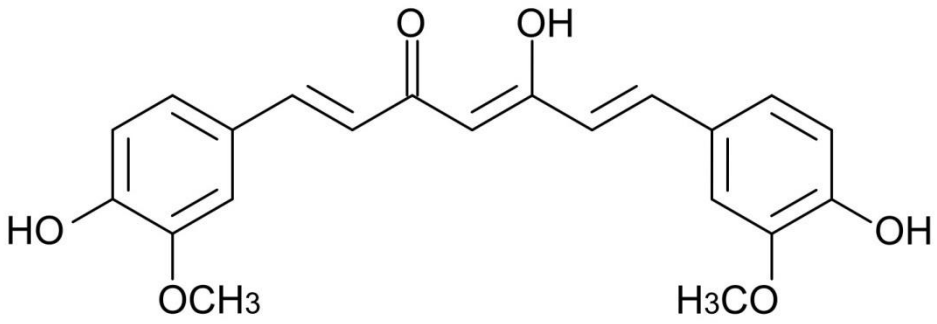

Fig.3. Chemical structure of curcumin.

Accumulating evidence suggests that curcumin possesses several pharmacological properties with a wide range of molecular target. It has been investigated as anti-inflammatory, antimicrobial, antiviral, antifungal and antioxidant. Moreover, its properties of chemo and radio-sensitizing as well as its wound healing activities have been reported[25]. The variety of curcumin molecular targets comprehends more than 100 molecules, including transcription and growth factors within their receptors, cytokines, enzymes, and genes related tocell proliferation and apoptosis[24]. In addition, curcumin acts as antiproliferative agent, since it interrupts the cell cycle by disrupting mitotic spindle structures and inducing apoptosis and micronucleation[25,26]. So far, curcumin has been deeply investigated as pharmacological agent with multiple activity[24,25,27].

Curcumin has anti-inflammatory activity

Being turmeric present in the traditional Indian Ayurveda[24], it has been known from long time that this plants exhibits anti-inflammatory activity. However, it was just in the past three decades that an extensive research has been performed on the turmeric anti-inflammatory mechanism. It was found that curcumin is the actual responsible for turmeric effects[27].

As summarized by Aggarwal and Harikumar[27], curcumin was found to exhibit therapeutic potential in various chronic disease in which inflammation plays a major role, such as Alzheimer's and Parkinson's disease, multiple sclerosis, epilepsy, cerebral injury, cardiovascular diseases, allergy, asthma, bronchitis, colitis, rheumatoid arthritis, renal ischemia, psoriasis, diabetes, obesity, depression, fatigue, and lastly cancer.

Anti-inflammatory mechanism of curcumin was firstly demonstrated by Singh and Aggarwal[28]. They found that curcumin acts as a potent blocker of the ubiquitous transcription factor NF-κB, whose activation is induced by different inflammatory stimuli. Later on, a large body of literature revealed that curcumin could suppress inflammation through multiple pathways[27] (Table1).

Pathway inhibited by curcumin action				
TNF-α	IL-1β	IL-6	STAT3	MIP-1α
HAT	COX2	5-LOX	ICAM-1	ELAM-1
VCAM-1	GHS-PO	NQO-1	BACE-1	iNOS
LOX	LPO	CTGF	UPA	MMP-9
CRP	VEGF	PI3K-AKT	ODC	NRF2
HIF-1α	NF-κB	CXCR4	IFN-γ	IL-8

Table1. Different mechanisms through which curcumin acts as anti-inflammatory drug[27]

Curcumin exhibits antitumor activity

Until now, the anticancer potential of curcumin has been reported in more than 800 articles[27]. Curcumin anti-proliferative effects have been demonstrated in extensive *in vitro* studies, as well as in different animal models[24]. In particular, curcumin is able to target several steps of the biomolecular pathways involved in carcinogenesis by blocking the transformation, proliferation, and invasion of tumor cells[29]. Accordingly, curcumin is nowadays object of various clinical trials for cancer therapy, as reported by Goel *et al*[24].

Curcumin interacts with cells of the immune system altered during cancer development

Among the variety of curcumin activities against cancer progression, its ability to suppress myeloid-derived suppressor cells (MDSC)[30] and active macrophages[31] is of particular importance. Different studies[25] have also shown the ability of curcumin to modulate macrophages activation.

Curcumin is extremely safe and well tolerated

In addition to the massive study about curcumin pharmacological effects, a number of clinical trials have addressed pharmacokinetics and toxicological profile of curcumin in humans.

First evidence for curcumin safety is related to the fact that turmeric has been present in human diet for long time, as part of the common used spice curry, in a concentration that ranges up to 100 mg/day[24]. Orally assumed curcumin can be considered as pharmacologically safe. Moreover, recent phase I clinical trials as well as additional reports indicate that a dose of curcumin as high as 12 g/day is well tolerated without toxic side effects[24,32].

Considering all of these conditions, curcumin presents a great potential for employment in TAMs depletion.

1.3.2 "The silencing revolution": siRNA

Since the Nobel-prize winning discovery of RNA interference (RNAi)[33], small interfering RNA (siRNA) is considered a potential revolution in therapy, being theoretically able to deregulate the expression of all the genes involved in pathogenesis of different disorders, including cancers and autoinflammatory diseases[34].

RNAi is a natural phenomenon of gene silencing mediated by RNA and it is highly conserved among multicellular organisms. Basically, RNAi is able to inhibit the conversion of messenger RNA (mRNA) into proteins. In physiological process, the double-stranded RNA (dsRNA) presents a sense (passenger) and an antisense (guide) strand, the latter one complementary to the target mRNA. Firstly, dsRNA molecule is recognized by an RNase type III enzyme (Dicer), and cleaved into small fragments[35–37]. These fragments bind to the RNA-induced silencing complex (RISC), located in the cells cytosol. The dsRNA passenger strand is then cleaved while the guide strand is directed to the 3' untranslated region of the complementary target mRNA[35,38].

When dsRNA is not endogenous but exogenously introduced, it takes name of siRNA. After siRNA interaction with RISC,the cleavage enzyme “argonaute 2” within the RISC complex degrades the target mRNA, thereby preventing protein transcription[35].

So far, therapeutic strategies based on siRNA have been taken into consideration as an alternative approach to the pharmacological one in TAMs targeting. A valuable alternative to TAMs depletion is the use of siRNA to silence gene expression and normalize TAMs abnormal phenotype. In that way, TAMs protumorigenic effects can be countered and replaced by a stimulated anti-tumor immunity[1,19].

1.3.3 Multiple drug release

Especially in cancer treatment, it is fundamental to consider problems related to drugs toxicology. To achieve therapeutic levels, anticancer drugs need to be administered in high dose, and risk for developing drugs resistance is prominent. In fact, being tumors originated from a concomitance of different mechanisms, one single drug is commonly not sufficient to completely destroy cancer cells[39,40]. A combination of therapeutics is often the preferred treatment.

Compared to administering each single drug individually, the possibility to encapsulate more than one therapeutic molecule in the same delivery system represents a great advantage[41]. First of all, each drug can be specifically targeted at the active site in a correct ratio. Moreover, synergistic therapeutic effects, suppression of drug resistance and the ability to temporally control drug exposure can be exploited. This includes the opportunity to regulate proliferation, invasion, and metastatic process of cancer cells at the same time thanks to the synergetic and complementary effects of the selected drug molecules[40].

1.3.4 Curcumin and siRNA need to be vehiculated

Despite of its efficacy and safety[42], curcumin has not been approved as a therapeutic agent yet. The main reason is related to its low systemic bioavailability, since curcumin is poorly adsorbed

and rapidly metabolized. Many studies in rats and humans indicated that curcumin reached extremely low serum levels and effective concentration was obtained only in the gastrointestinal tract[43]. In this context, NPs represent a suitable tool for encapsulating highly hydrophobic agents like curcumin and circumventing major pitfalls of poor aqueous soluble drugs. Indeed, NPs can increment curcumin solubility, modulate its route of administration, and improve drug bioavailability.

Similarly, siRNA use in clinics is still challenging due to its *in vivo* behavior. First, siRNA molecules undergo a rapid degradation within the host organisms, due to serum nucleases, renal excretion and passive entrapment in organs such as liver and kidneys. In addition, siRNA molecules are not able to specifically recognize and target cells or tissues involved in the pathology development. Finally, their hydrophilic characteristics do not allow siRNA molecules to cross the cell membrane and reach the cell cytosol, where the RISC is located[1]. To overcome these limits, biodegradable polymeric nanoparticles represent a promising tool for improvement in siRNA stability and specific delivery at the target site[44]. So far, very few nanosystems have been developed to increase siRNA stability, and the most majority of them relate to lipid nanoparticles or bioconjugates[44,45].

2. Nanomaterials as a promising tool for drug and gene delivery

2.1 Nanomaterials

Improvement in pharmacokinetics properties of the drugs is one of the major issues in drug formulations and pharmaceutical technology[46]. This is of particular importance when proteins and genes are used as therapeutics. In fact, their application in clinics seems hard to be reached because of the arduous *in vivo* fate of these biomacromolecules. First, after administration of proteins and genes, a rapid degradation occurs within the host organisms, due to serum nucleases, renal excretion and passive entrapment in organs such as liver and kidneys. Moreover, since cell membrane is highly selective and has poor permeability to hydrophilic molecules a number of physical barriers prevent biomacromolecules from reaching the cell cytosol, where

they are supposed to exert their effects. Finally, when endocytosis occurs, it is possible that biomacromolecules degradation takes place in the lysosome[47–49].

To overcome these limits, encapsulation of biomacromolecules and poorly water soluble drugs in nanomaterials (NMs) represents a promising tool.

Definition of NMs include systems with at least one of the three spatial dimensions below 1 µm and the term nanotechnology refers to the intentional synthesis, manipulation and use of objects with size in the nano range[50,51]. Fig. 4 summarized the great variety of NMs that can be synthesized to obtain structures with novel physical or chemical properties.

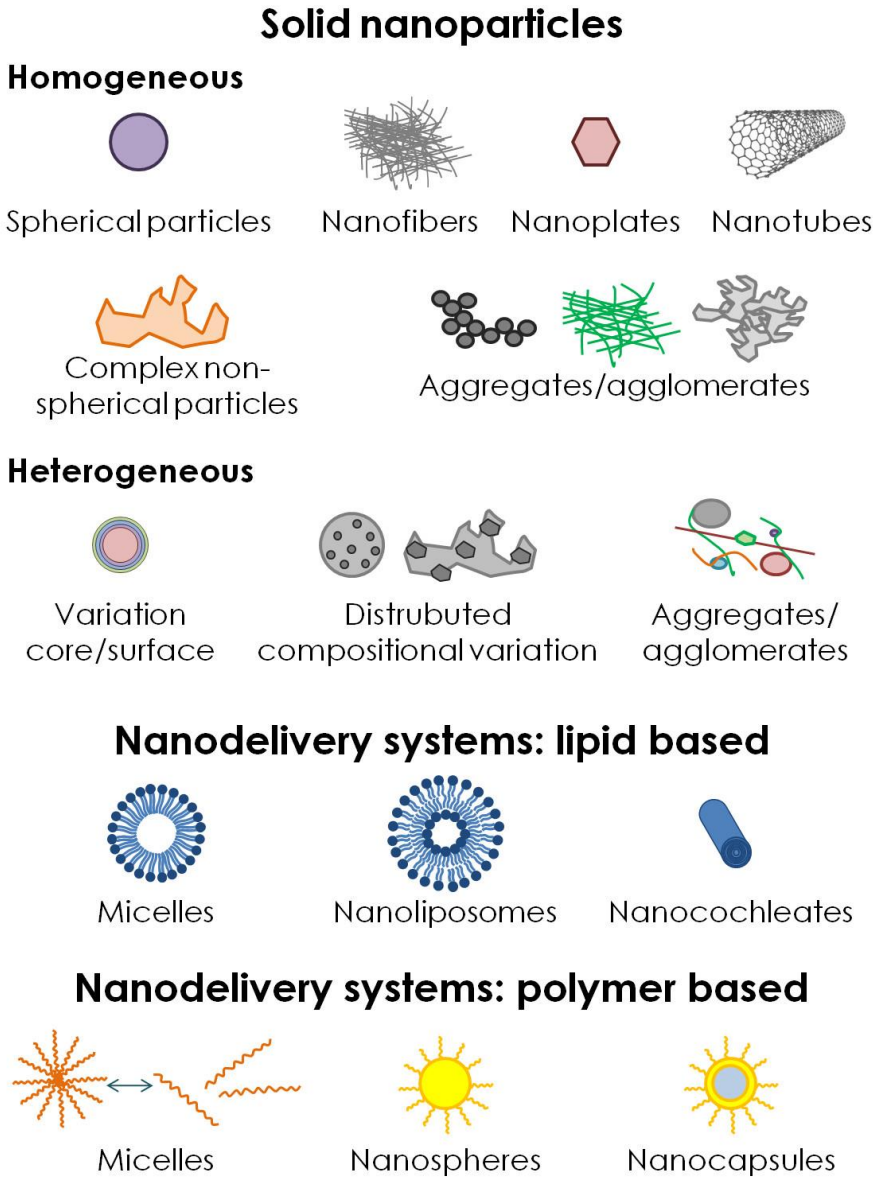

Fig. 4. Overview of available nanomaterials. In the scheme, nanomaterials are classified in base of their chemical nature.

The characteristics of NMs from the physical-chemical point of view may radically differ from those of the corresponding bulk materials[52]. Indeed, the latter usually present features that are independent on their shape and size. Differently, NMs properties are strictly related to the high increase in surface-to-volume ratio, as well as the fraction of atoms on the surface with respect to the total number of atoms in the material[52]. In this way, different characteristics such as materials coordination number, cohesive energy, melting point and temperatures of phase transitions are modulated. In the case of NMs, all of these characteristics have been found to be size and shape-dependent[50,52].

By properly engineering NMs synthesis, it is possible to design systems for drugs and genes administration. So far, NMs have been functionalized to avoid renal excretion[53,54], improve molecules bioavailability as well as their stability[55], and specifically target tumor vasculature[56,57], other specific tissues[58–60] or even cellular compartments[48,61,62]. In fact, larger surface-to-volume ratio improves the opportunity for surface functionalization of NMs, which is fundamental for technological application, especially in drugs or genes delivery[50].

Moreover, with respect to micron-size particles, NMs present increased capability to extravasate from the endothelium. This is of particular importance to target pathological sites such as inflamed tissues and tumors via the enhanced permeability and retention (EPR) effect. NMs can also penetrate microcapillaries and epithelium in the intestinal tract and in the liver[63,64]. Being smaller than the smallest capillaries in the body (5-6 μm), NMs are extremely suitable for systemic administration because they can be distributed in the bloodstream without forming aggregates, thusavoiding embolism[63].

Finally, the nanometric size improves NMs uptake by different cell types, thus helping drug accumulation at target sites[63,65–67].

2.2Polymeric nanoparticles

Among the great variety of NMs, this thesis especially explores the potential of polymeric nanoparticles (NPs) as a tool for gene and drug delivery. In fact, the NMs presented here combine the advantages of nano-sized objects with biodegradability and biocompatibility of polymeric materials[51,68–70].

NPs are solid, colloidal particles consisting of macromolecular substances that vary in size from 10 nm to 1000 nm[71–73]. Their matrix interacts with drug and macromolecules of different nature by dissolution, entrapment, adsorption, attachment and/or encapsulation[63].

NPs properties can be controlled and adjusted during their synthesis, thus conferring versatility to the system. In fact, the design of nano-sized polymer-based particles has attracted more and more attention due to their wide applicability in modern material and medical science[74,75]. In therapeutic applications, the use of drug or gene-loaded NPs has improved drug efficacy, specificity, tolerability and therapeutic index of corresponding drugs[76,77]. In fact, NPs systems considerably increase the drug payload, being each single NPs able to carry thousands therapeutic molecules[41]. Moreover, NPs avoid drug degradation while increasing its bioavailability, retention time and intracellular penetration. Appropriate NPs surface functionalization allows specific targeting and NPs chemical properties enhance their interaction with biomolecules, such as genetic materials, proteins or drugs. Fig. 5 schematically represents various opportunities to modulate polymeric NPs properties thus underlining the great versatility of these systems.

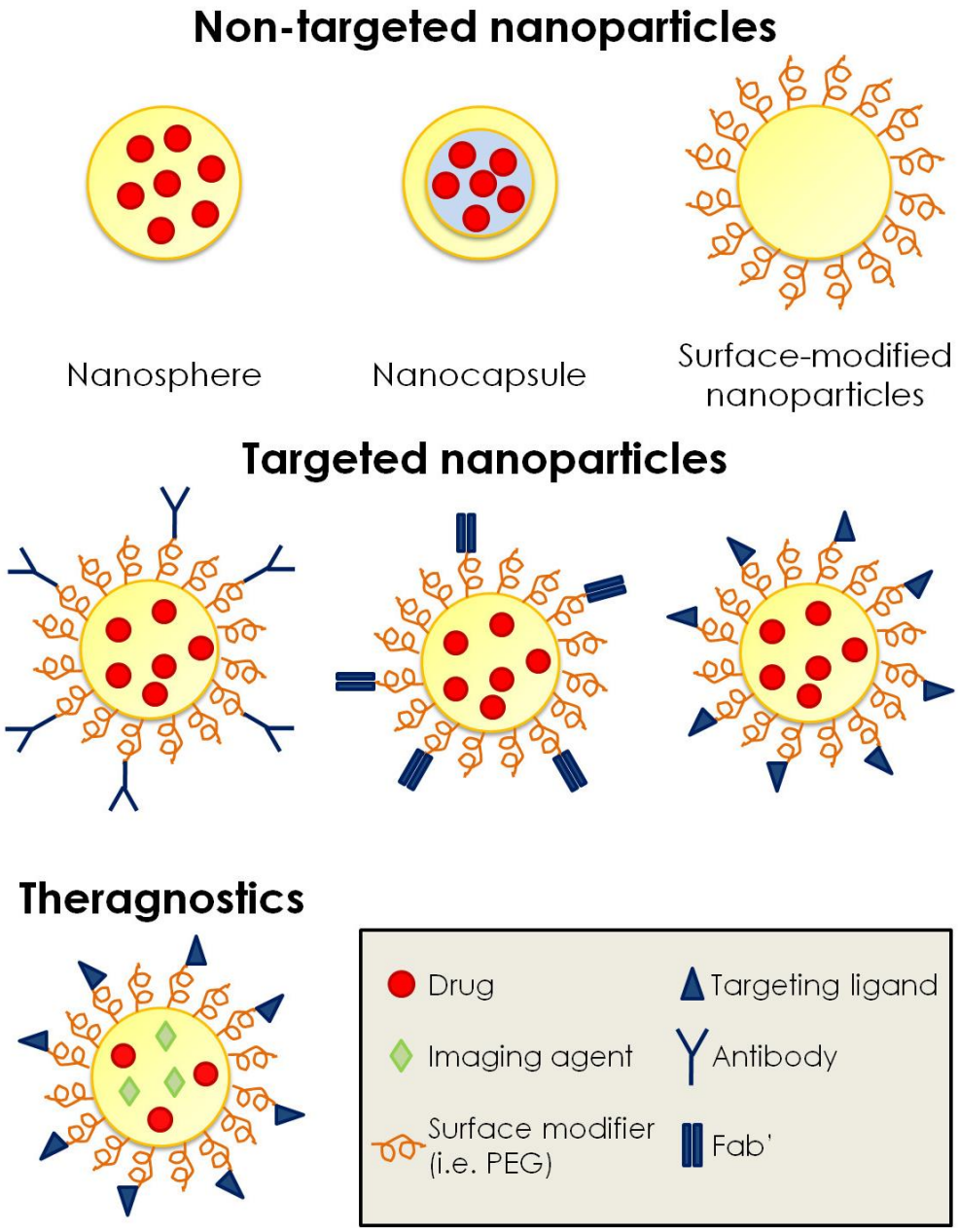

Fig. 5. Overview of polymeric nanoparticles and their functionalization. (PEG, polyethylene glycol)

Polymeric NPs can present different structures depending on their synthetic method (see paragraph 2.2.2.2 Synthetic methods for PLGA NPs page 34 in the introduction section).

Surface functionalization can be additionally obtained by proper chemical modification, thus improving NPs stability as well as their capabilities for specific targeting. These features are also influenced by particle size, surface charge, and hydrophobicity. In particular, both the size and size

distribution of NPs are important to determine their interaction with the cell membrane and to control the penetration across the physiological barriers[78,79].

2.2.2. Poly(Lactic-co-Glycolic) Acid Nanoparticles

2.2.2.1 Poly (Lactic-co-Glycolic) Acid (PLGA)

In order to avoid most of the problems associated with natural polymers, in terms of cost, production, safety and allergic reaction, synthetic polymers have been increasingly used for the design of polymeric NPs[80]. For this purpose, different polymeric classes have been explored, such as poly(amides)[81], poly(amino acids)[82,83], poly(alkyl-α-cyano acrylates)[84,85], poly(esters)[86,87], poly(orthoesters)[88], poly(urethanes)[89,90], and poly(acrylamides)[91,92]. Amongst them, great success has been obtained by thermoplastic aliphatic poly(esters) like Poly Lactic Acid, Poly Glycolic Acid, and particularly poly(lactic-co-glycolic) acid (PLGA) (Fig.6), because of their biocompatibility and biodegradability[87].

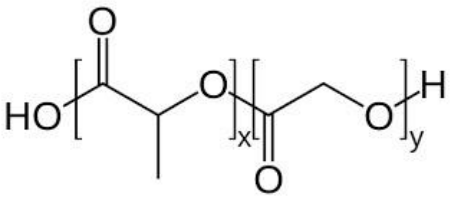

Fig.6. Chemical structure of Poly (Lactic-co-Glycolic) Acid (PLGA).

In this dissertation, main focus was on developing PLGA-based NPs. Indeed, PLGA products for drug delivery and diagnostics have been already approved by Food and Drug Administration (FDA) and are available in the market[67,87,93,94]. PLGA is associated with reduced *in vivo* toxicity thanks to its biodegradability properties. In fact, the degradation mechanism through hydrolysis leads to the release of lactic acid and glycolic acid. These monomers are endogenous and can be easily metabolized because they enterin a number of physiological and biochemical pathways[68,94,95]. Additionally, PLGA is commercially available with different molecular weights and monomeric

ratio, thus allowing the possibility to tune polymer degradation time[94,96]. In fact, lactic acid is more hydrophobic than glycolic acid. Accordingly, PLGA copolymers containing higher amount of lactide monomer are consequently less hydrophilic, absorb less water, and degrade slower[87,93].

2.2.2.2 Synthetic methods for PLGA NPs

Several methods are available for PLGA NPs synthesis and they resultin different NPs structures[63,94,97]. In particular, as can be seen in the scheme (Fig.7), a nanocapsular structure is present when the drug or biomacromolecule is encapsulated in the inner NPs core. In this way NPs present a core-shell structure. Differently, when the selected drug or molecules is either entrapped or adsorbed in the polymeric matrix, the NPs structure obtained is a nanosphere. In this case, NPs matrix is compact and homogeneous.

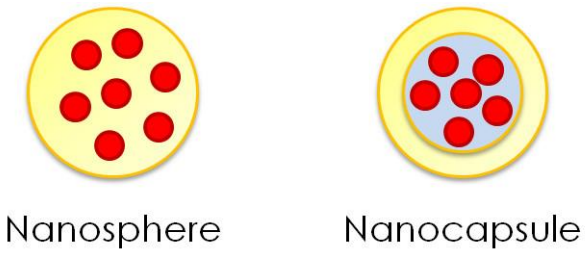

Fig.7. Graphical scheme of nanosphere and nanocapsule.

One of the most common techniques for PLGA NPs synthesis is the emulsion-solvent evaporation method[87,93,94]. This synthesis allows the encapsulation of hydrophobic and/or hydrophilic molecules in mild conditions, thanks to the use of small volume of organic solvents, and no elevated temperature or high vacuum. In general, polymer is dissolved in an organic solvent and the oil-in-water (OW) emulsion is obtained by adding a surfactant solution. Sonication or homogenization is used to induce the formation of nano-sized droplets. The solvent is then evaporated or extracted and the NPs collected after centrifugation. NPs obtained in this way are nanospheres, with a homogeneous matrix structure. To encapsulate hydrophilic molecules (such

as hydrophilic drugs, peptide, antibodies, nucleic acids) and obtain a core-shell structure, a double water-in-oil-in-water (WOW) emulsion is necessary. The aqueous inner solution is firstly emulsified with the organic polymeric solution and the obtained water-in-oil emulsion is further emulsified with the surfactant phase.

Another commonly used technique for PLGA NPs synthesis is based on nanoprecipitation[93,94]. In this case, PLGA and the drug are both dissolved in an organic solvent, and the solution is then added drop by drop to a high volume of aqueous solution. After solvent evaporation, NPs can be collected. This system is successful for nanospheres formation, with encapsulation of hydrophobic molecules, while biomacromolecules can be loaded only by adsorption on NPs surface after production[94,95]. In this way entrapment efficiency is low and hydrophilic molecules are susceptible to denaturation, aggregation, oxidation and cleavage, particularly at the NPs surface-aqueous phase interface. Moreover, nanoprecipitation synthesis is an expensive method because of the higher amount of organic solvent employed[95].

Other available techniques includes the spray-drying method, salting-out, dialysis and supercritical fluids technologies[73,94,97]. The application of these techniques is limited by various inconvenient, such as working with costly dedicated apparatus, low yield on encapsulation, high energy consumption or difficulties in purification of non-biocompatible reagents[98]. Accurate description of these techniques is beyond the aims of this thesis and further details can be found in the literature[73,94,97].

3. Challenges in drug and gene delivery with PLGA NPs

3.1 PLGA NPs interface with complex medium

One of the major challenges for NPs use in drug and gene delivery is related to their interaction with cells, lipid bilayers, biological membrane and biological medium in general[99].

Once in the bloodstream, NPs can encounter different fates. First of all, they can be recognized by the host immune system and rapidly cleared from the circulation by phagocytes[63]. Moreover, NPs

with a very active surface can be rapidly opsonized and consequently removed by the mononuclear phagocyte system (MPS) present in different organs such as liver, spleen, lungs and bone marrow[63]. Degree of opsonization and NPs lifetime in the blood are strictly dependent on the NPs interaction with macromolecules, especially proteins, in the bloodstream. In fact, it is nowadays well known that macromolecules spontaneously accumulate at the NPs-water interface, thus creating a sort of additional coating that alter the NPs adsorption properties[99,100]. This "protein corona" is composed by soft and hard components. While the first is dynamically and rapidly exchanged from the particles to the medium, the latter presents a high affinity for the NPs surface and is not removable by simple centrifugation[100].

This protein corona greatly influence NPs biological response, including cellular uptake, clearance route and accumulation in target organs[100–102]. In fact, NPs internalization is generally mediated by an active process, because NPs size does not allow passive passage through physiological membrane. In such an active internalization, the primary contact between NPs and cells mediated by NPs surface is fundamental. Thus, alteration in the surface means alteration in NPs-biological interaction[101].

The protein corona formation is influenced by chemical property of the nanomaterial, as well as its size and surface features. In particular, the latter two characteristics are proved to be more important than NPs material on influencing the composition of the hard corona, and consequently the NPs biological interactions[100].

During NPs synthesis, maintaining a rigid control on the NPs surface properties is fundamental to foresee their fate when in contact with biological medium[99]. The most reliable parameter for assessing NPs surface properties as well as their stability is represented by the ζ-potential[63]. In fact, ζ-potential values lower than -20.0 mV or higher than +20.0 mV usually ensure electrostatic repulsion between NPs and prevent NPs aggregation[63,103–105] (see also paragraph 5.1 "Dynamic light scattering" page 54 in the materials and methods section).

3.2Endosomal escape

For both curcumin and siRNA treatment, it is essential to deliver NPs content in the cells cytosol, where the drugs can exert their effect. As presented in paragraph 3.1, due to their size NPs cannot enter the cells via passive transport through physiological membrane and an active process is required.

One of the possible way through which macromolecules and particles can be internalized from the extracellular environment is endocytosis, either mediated or not by receptors. In this process, the plasma membrane invaginates and internalizes externally disposed solutes, macromolecules, and pathogens[106]. The so formed vesicle represents the early endosome and becomes progressively acidic, thus maturing into the late endosome. In fact, the proton pump vacuolar ATPase accumulates protons in the vesicle until a pH around 5-6 is reached. Process generally ends when the late endosome fuses with the lysosome, where the content is degraded by enzymes and highly acidic pH (4-5)[48,107]. Considering this mechanism, after internalization NPs have to escape from the endosomal pathway to avoid degradation and more importantly torelease their cargo into the cytoplasm (Fig. 8).

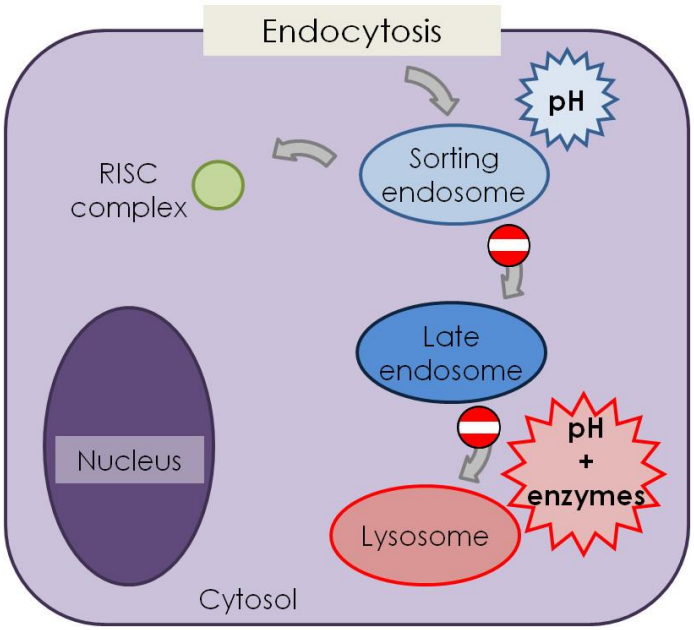

Fig. 8. Graphical scheme of endosomal escape for cytosol targeting. In the scheme, RISC complex localization in the cell cytosol was underline for therapy based on siRNA.

4. Proposed strategies for drug and gene delivery

4.1 Modulate NPs surface charge: amino-PVA as surfactant

PLGA NPs are frequently obtained by emulsion-solvent evaporation method to encapsulate hydrophilic biomacromolecules (paragraph 2.2.2.2 Synthetic methods for PLGA NPs page 34 in the introduction section),which could be irreparably denatured in their tertiary structure when harsh conditions are applied[94,108,109]. In this type of synthesis, an emulsifier is required and polyvinyl alcohol (PVA) is commonly the preferred one because it forms uniformly dispersed NPs of relatively small size and allows good drug entrapment efficiency[97,108,110–112].

Due to its polymeric nature, PVA forms an interconnected network with PLGA at the interface, and even after purification its residual constitute up to 13% of the NPs weight[113,114]. Such a high percentage of surfactant localized on the NPs surface could influence their interactions with the biological environment[115,116].

In this context, chemical modification of the PVA structure additionally improve the NPs ability to enter the cells and especially to escape the endosomes[97,117]. In particular, the presence of positive charges on the surfactant chemical structure, and consequently on the NPs surface, helps the binding with negatively charged group on the cells surface. In that way a great efficiency in cell-membrane penetration and cellular internalization can be achieved[99]. Moreover, cationic NPs produce an osmotic imbalance that destabilized the endosomal membrane. In this way, the organelles membranes become leaky and allow the encapsulated molecules to exit and reach the cell cytosol[62].

To date, positively charged PLGA NPs have been synthesized by either nanoprecipitation[118,119] or self-assembly[120,121]. However, both these methods present some drawbacks. In fact, in the nanoprecipitation synthesis, hydrophilic biomacromolecules may be denatured by organic solvent exposure, whereas the self-assembly involves multi-step and time-consuming procedures. So far, only few efforts have been done to achieve positively charged PLGA NPs by emulsion-based methods[105].

In this thesis, a PVA-based surfactant containing tertiary amines (amino-PVA) was synthesized and characterized from the chemical point of view. The surfactant properties of the developed amino-PVA were investigated either alone or in combination with PVA, in different kinds of emulsion syntheses.

4.2 Modulate NPs compatibility: calcium stearate as surfactant

PVA has been the favorite emulsifier in the synthesis of PLGA NPs because of its ability to form stable and uniformly distributed NPs. However, disadvantages in the use of PVA may be related to a partial evidence of toxicity, especially when the surfactant is used at high molecular weight[122]. Moreover, PLGA NPs with high amount of residual PVA were found to present relatively low cellular uptake[115].

Another important aspect from an economic and ecological point of view that is strongly underestimated during NPs engineering and manufacturing processes is the waste of raw materials and their consequent disposal cost. Some authors[112] considered that in emulsion-evaporation synthesis the external water phase is commonly added in great excesswith respect to NPs concentration. In this way a huge amount of surfactant is used, meaning that it has to be bought and removed after NPs synthesis. This results in increased productive costs and high volume of contaminated water that must be safely disposed of. Moreover, additional energy is necessary to collect and purify NPs after synthesis.

It is therefore imperative to look for an alternative surfactant to be used in formulating biocompatible PLGA NPs. This surfactant should guarantee NPs stability, size and polydispersity similar to PVA-synthesized NPs, while improving biocompatibility and safety. To date, several chemicals have been studied as alternatives to PVA, in particular polymers, such as Polyvinylpyrrolidone and poloxamer[112], and surfactants like Tween 60®, Tween 80® or thePluronic® family[108]. However, to the best of our knowledge, low molecular weight molecules have not been explored so far to synthesize PLGA NPs.

In the present dissertation, the employment of calcium stearate (CSt) (Fig.9) as an alternative to PVA was investigated in order to gain cost-effective, stable and safe PLGA NPs.

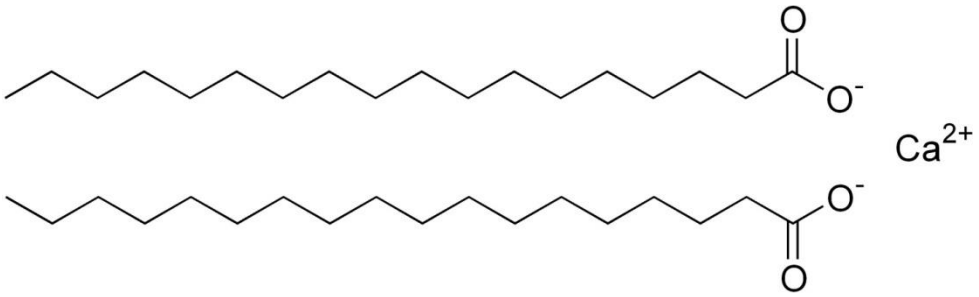

Fig.9. Chemical structure of calcium stearate (CSt).

CSt is a promising surface active agent presenting two linear chains with an 18-carbon length tail and a carboxylated hydrophilic head each. Its low MW (607.03 g/mol) is expected to provide a lower toxicity with respect to high MW surfactants[123]. In addition, CSt has very low cost and it has already been used for several patented medical devices and scaffolds for tissue engineering. However, the influence of CSt on encapsulation efficiency, size and structure of nano- and microparticles was not thoroughly studied so far.

4.3 NPs surface decoration

4.3.1 Protein corona as biocompatible additional coating

The prediction of NPs fate in the body in terms of pharmacokinetics and biodistribution is challenging, mainly because protein binding and consequent protein corona formation are difficult to predict[124]. Indeed, biomacromolecules adsorbed on NPs surfaces are different from those adsorbed on flat surfaces with the same chemical composition[101]. Even if a number of studies have been performed and many techniques (such as differential centrifugal sedimentation DCS, Field Flow Fractionaction FFF, proteomics) are available for determining the protein corona composition, a huge number of variables make difficult this task.

Moreover, it is nowadays accepted that hard corona constitutes the effective unit through which NPs interact with cells (see paragraph 3.1 PLGA NPs interface with complex medium page 35 in the introduction section). Since proteins can physically cover active targeting moieties on the NPs surfaceor interfere with their specific functions, the biological outcomes of NPs can be significantly altered with respect to predicted activity.

The protein corona formation is related to chemical composition, surface features and size of NPs[125]. It should be thereby possible to manipulate the NPs biological coating by controlling these parameters, thus providing NPs with desired properties. Alternatively, careful selection of the molecular content in the suspending medium may modulate the protein corona composition and NPs surfaces can be enriched with molecules of interest. Accordingly, the protein corona formation can be transformed froma problem to an opportunity for NPs specific targeting.

4.3.2 D-mannose for specific TAMs targeting

In this work, D-mannose (Fig.10), a hexose monosaccharide isomer of glucose, was selected as specific ligand for TAMs targeting.

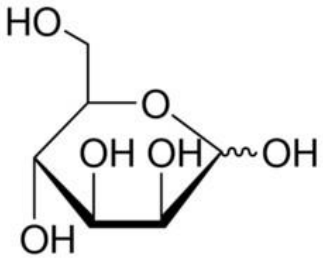

Fig.10. Chemical structure of D-mannose.

It is largely established that mature macrophages highly up regulated on their surface the mannose receptor CD206[120,126]. Consequently,the development of mannose coated PLGA NPs may emerge as a prospective strategy for the selective delivery of anti-cancer agents towards TAMs.

The mannose receptor family is a subgroup of the C-type lectin superfamily, uniquely presenting a multiple C-type lectin-like domains within a single polypeptide backbone. Mannose receptor CD206 recognizes proteins bearing terminal mannose residues such as glycosylated lysosomal enzymes, saccharide chains terminating in mannose, fucose or *N*-acetylglucosamine. Initial interest in this receptor derived from its ability to recognize and internalize a unique spectrum of monosaccharides and lysosomal enzymes bearing terminal mannose residues. Once activated, all the mannose receptor family members are rapidly internalized from the plasma membrane via clathrin-coated vesicles and enter into the endosomal pathway[127].

Mannosylation has been described as a safe procedure to ensure targeted delivery of anti-cancer drug to tumor site, with reduced access to not specific target tissues. In this way it was possible to optimized therapeutic response and efficacy, with minimal side effects[120,128].

5. Thesis aims

This dissertation is related to the development of polymeric NPs for the specific targeting of Tumor Associated Macrophages (TAMs) as an innovative therapeuticapproach for cancer treatment.

TAMs are deeply involved in the pathology of cancer proliferation, thus strategies to deplete them or inhibit their recruitment into neoplastic lesions represent promising tools for chemotherapy. So far, no specific drugs are available for TAMs targeting, with the exception of trabectedin. Accordingly, here innovative treatment based on curcumin or RNA interference has been proposed. To date, the employment of these molecules in therapeutics has been limited because of their low systemic bioavailability and their rapid degradation.

To overcome this limits, nanomaterials (NMs) have been presented as a tool for encapsulation of biomacromolecules and poorly water soluble drugs. Among them, polymeric NPs have been selected because they present the advantages of nano-sized objects combined with biodegradability and biocompatibility of polymeric materials.

In this thesis, poly (Lactic-co-Glycolic) Acid (PLGA) as safe and versatile materials have been used for the development of polymeric NPs by either single (OW) or double (WOW) emulsion-solvent evaporation methods. Different synthetic parameters have been thoroughly investigated, with particular focus on the surfactant role.

In order to modulate NPs surface charge and improve their potential for endosomal escape, a cationic newly synthesized polymer (amino-PVA) has been proposed.

Additionally, PLGA NPs biocompatibility and cost-effectiveness have been improved by the employment of CSt as innovative surfactant.

Finally, to ameliorate NPs biocompatibility and specific targeting for both amino-PVA and CSt stabilized PLGA NPs, strategies for surface decoration with proteins and D-mannose have been investigated.

Materials and Methods

1. Materials

Poly(Lactide-co-Glycolide)acid (PLGA) with different monomer ratio and molecular weight were purchased from Sigma Aldrich, namely (i) 50:50, MW 38-54,000 (Resomer RG504®, ester terminated); (ii) 50:50, MW 7-17,000 (Resomer RG502®, ester terminated); (iii) 81:15, MW 190-300,000 (Resomer RG858®, ester terminated). If not differently stated, Resomer RG504® was employed.

Poly(Vinyl) Alcohol (PVA, Mowiol® 4-88 MW 31,000, 86.7-88.7 mol% hydrolysis), curcumin from Curcuma longa (Turmeric), ethyl acetate, calcium stearate 6.6-7.4% Ca basis (CSt), polysorbate 60 (P60), Span® 60 (sorbitanemonostearate, S60), D-mannitol, vinyl acetate, ethylen glycol, acetonitrile (CH_3CN), N-(3-(dimethylamino)propyl)methacrylamid (DMAPMA), ammonium persulfate (APS), acetone, Fetal Bovine Serum (FBS), ethanol (EtOH), Dimethyl sulfoxide (DMSO), fluorescein isothiocyanate (FITC), dichloromethane (DCM), chloroform, D-mannose, sodium chloride (NaCl), trehalose, were obtained from Sigma Aldrich and used without further purification.

The PVA with MW 22,000 and 98 mol% hydrolysis was purchased from VWR international.

Alexa Fluor® 488 goat anti-mouse IgG1 (isoform γ1, IgG1-488) and fibrinogen from human plasma Alexa Fluor® 647 conjugate (Fib-647) were obtained from Life Technologies.

Phosphate Buffer Saline (PBS) was prepared by mixing 136.9 mM sodium chloride, 2.7 mM potassium chloride, 3.2 mM sodium phosphate dibasic dehydrate, 1.5 mM potassium phosphate monobasic. The pH value was adjusted by means of sodium hydroxide or hydrochloric acid, as appropriate. IgG1-488 was diluted in a medium containing 0.1 M sodium phosphate, 0.1 M NaCl and 5.0 mM sodium azide. All of these chemical were purchased by Sigma Aldrich.

Vegetal RNA extract was a kind gift of the Plant Model System Platform (Filarete Foundation, Milan, Italy).

ProLong® Gold was a kind gift of the Imaging Platform (Filarete Foundation, Milan, Italy).

Bidistilled water (MilliQ, Millipore) was used in all the experiments.

For cytotoxicity studies, RAW264.7 (American Type Culture Collection, ATCC) murine macrophages were selected as a model cell line. Cells were grown in Dulbecco minimal essential medium (DMEM) containing 10.0% fetal bovine serum (FBS) and 2 mM glutamine. In addition, primary culture of mouse bone marrow-derived macrophages was investigated. Cells were grown in high glucose DMEM supplemented with 20.0% v/v low endotoxin FBS, 30.0% v/v L929-conditioned medium, 1.0% v/v glutamine, 1.0% v/v Pen/Strep, 0.5% v/v sodium pyruvate, and 0.1% v/v b-mercaptoethanol. These experiments were performed thanks to the collaboration of Dr. Serena Ghisletti at the European Institute of Oncology (Milan), department of Experimental Oncology.

Statistical analyses were performed by means of the Origin software. The free available software Image J was used for particle analysis on Scanning Electron Microscopy images.

2. Instruments

Centrifuges: Eppendorf 5415R and Heraeus multifuge X3R, Thermo scientific

Confocal microscope: Leica TCS SP5 AOBS, Leica Microsystems GmbH and Leica TCS SP8 microscope equipped with a gated-STED module, Leica Microsystems GmbH

Dynamic Light Scattering: Zetasizer Nano ZS90, Malvern Instruments

Fourier transformed infrared spectroscope: Cary 660, Agilent

Freeze dryer: Telstar Cryodos 50

Nuclear Magnetic Resonance: Bruker Avance 400

Scanning electron microscope: Zeiss Sigma, Carl Zeiss NTS GmbH

Spectrofluorometer: FluoroMax 4, Horiba, JobinYvon

Transmission Electron Microscope: FEI Tecnai 200kV

Ultrasound probe: Vibracell VCX130, net power output 130 Watts, frequency 20KHz

UV-Vis spectrophotometer for small volume: Nanodrop® 1000, Thermo Fisher

UV-Vis Spectrophotometer: Cary 100, Agilent

UV-Vis Spectrophotometer: TECAN Sunrise (for MTT test)

X-ray photoelectron spectroscope: UHV apparatus Leybold LH 10/12

3. Samples name (Table2)

Surfactant	Sample name	Synthetic procedure	Structure	Encapsulated biomolecule
Polyvinyl Alcohol (PVA)	P0.2-OW-Cur	Oil-in Water (OW)	Solid	Curcumin
	P0.2-OW-ctr	OW	Solid	None
	P1-OW-ctr	OW	Solid	None
	P0.2-IgG-488	Water-in-Oil-in-Water (WOW)	Core-shell	IgG1-488
	P1-IgG-488	WOW	Core-shell	IgG1-488
	P1-vRNA	WOW	Core-shell	Vegetal RNA
	P0.2-ctr	WOW	Core-shell	None
	P1-ctr	WOW	Core-shell	None
Amino-PVA	A-OW-Cur	OW	Solid	Curcumin
	A-OW-ctr	OW	Solid	None
	A-fib	WOW	Core-shell	Fib-647
	A-FITC	WOW	Core-shell	FITC
	A-cur-fib	WOW	Core-shell	Fib-647 and curcumin
	A-ctr	WOW	Core-shell	None
Calcium stearate	C-OW-cur	OW	Solid	Curcumin
	C-OW-ctr	OW	Solid	None
	C-fib	WOW	Core-shell	Fib-647
	C-FITC	WOW	Core-shell	FITC
	C-ctr	WOW	Core-shell	None
	C-cur	WOW	Core-shell	Curcumin
	C-cur-fib	WOW	Core-shell	Fib-647 and curcumin

4. PLGA NPs synthesis

The PLGA nanoparticles were synthesized by either single (OW) or double (WOW) emulsion solvent evaporation methods[78,94]. Different surfactants were employed in order to obtain systems able to encapsulate hydrophobic or hydrophilic drugs and syntheses were modified accordingly.

4.1 Synthesis of PLGA NPs with PVA

To obtain PLGA NPs by OW method (P0.2-OW-ctr and P1-OW-ctr), PLGA was dissolved in 300 µL of ethyl acetate at the concentration of 50.0 mg/mL. The PLGA solution was emulsified with 600 µL of PVA at different concentrations by ultrasound (30% amplitude, 15 sec, ice bath) and the obtained emulsion was diluted with 50 mL of PVA 0.3% w/v. Then, the organic solvent was evaporated via magnetic stirring for 3.5 h.

Differently, the PLGA NPs with an aqueous inner core (P0.2-ctr and P1-ctr) were prepared by a two steps procedure. First, an aqueous solution of PBS 0.1X (15 µL) was added to the PLGA/ethyl acetate solution (50.0 mg/mL) and sonicated at 30% amplitude for 15 sec in ice bath, to obtain the primary water-in-oil emulsion. This emulsion was then added to 600 µL of PVA at different concentrations and sonicated using the same protocol described above, to achieve the multiple water-in-oil-in-water emulsion. Finally, the WOW emulsion was diluted in the dispersing phase (50.0 mL PVA 0.3% w/v) and the organic solvent was evaporated via magnetic stirring for 3.5 h.

To note, P0.2 and P1 in the PVA stabilized PLGA NPs name referred to the PVA quantity used in the syntheses, namely 0.2% and 1.0% w/v.

4.1.1 Encapsulation of hydrophobic molecule: curcumin

To obtain samples encapsulating a hydrophobic drug (P0.2-OW-cur), curcumin was dissolved in the PLGA-ethyl acetate solution at the concentration of 5.0 mg/mL. In this way, curcumin-PLGA ratio was 1 to 10, that is described as the best drug-polymer ratio[129–131].

4.1.2 Encapsulation of hydrophilic molecules: IgG1-488, vegetal RNA

In the systems obtained by WOW emulsion, two different model macromolecules were encapsulated in the aqueous inner core. In particular, IgG1 conjugated with Alexa488® (IgG1-488) was selected as a model antibody with fluorescence properties. IgG1-488 was added at the concentration of 0.1 mg/mL (P0.2-IgG-488 and P1-IgG-488) and diluted in a solution of 0.1 M sodium phosphate, 0.1 M NaCl and 5.0 mM sodium azide, as reported by the manufacturer.

In addition, RNA was encapsulated (P1-vRNA) to evaluate the system suitability for gene therapy application. In particular, a mixture of RNA extracted by Arabidopsis was used and named "vegetal RNA". Final vegetal RNA concentration was 0.15 mg/mL, as assessed by Nanodrop®.

4.2 Synthesis of PLGA nanoparticles with amino-PVA

4.2.1 Synthesis and characterization of amino-PVA

The polymer was synthesized by APS-initiated free radical polymerization.

Free radicals are unpaired electrons that are highly reactive and have short lifetimes. In free radical polymerizations, each polymer chain grows by addition of monomer to the free radical of the growing chain. Upon addition of the monomer, the free radical is transferred to the new chain end. This kind of reaction typically occurs when unsaturated monomers are present, such as vinyl or vinylidene. Reaction takes place after formation of free radical, thanks to the presence of a trigger, such as hydrogen donors like amines. Dissociation of an initiator (I) yields two radicals (R•) with dissociation rate constant K_d:

$$I \rightarrow 2R\bullet$$

This radical then attacks to a monomer molecule to create the first radical M• and in this case K_i is the rate constant of initiation.

$$R\bullet + M \rightarrow RM\bullet$$

The free radicals formed are very active and immediately add on monomer molecules leading to growing macroradicals. Each addition creates a new radical that has the same identity as the previous one, except that it is larger by one monomer unit. In the polymerization mechanism, it is assumed that all growing chains have the same propagation constant (k_p). The successive additions may be represented by:

$$M_n\bullet + M \rightarrow M_{n+1}\bullet$$

Termination usually occurs by combination

$$M_n\bullet + M_m\bullet \rightarrow M_{n+m}$$

or disproportionation reactions.

$$M_n\bullet + M_m\bullet \rightarrow M_n + M_m$$

In detail, 4 mL of vinyl acetate 50.0% v/v in water were added to 4 mL of DMAPMA. The mixture was left overnight under magnetic stirring in presence of ammonium persulfate as a trigger. The resultant polymer was then collected after precipitation with acetone, and purified by ultra-filtration using 1000 Da cut-off semi permeable membrane (Millipore). Amino-PVA was obtained as fine yellowish powder after freeze-drying (Telstar Cryodos 50 freeze-dryer).

To assess chemical properties of the obtained polymer after synthesis, Fourier-transform infrared spectroscopy (FT-IR, Cary 660, Agilent) and Nuclear Magnetic Resonance (NMR, Bruker Avance 400, operating at 400.132 MHz) analyses were performed. In the latter case, amino-PVA was solubilized in deuterium oxide at the concentration of 30.0 mg/mL.

^{1}H NMR (400 MHz, D2O, 25°C, δ): 0.84 (br, ***CH2***-CH-***CH2***-C), 1.63 (br, N(CH3)2-CH2-***CH2*** and ***CH3***-C-CO), 1.81 (br, ***CH3***-CO), 2.28 (N(***CH3***)2), 2.46 (br, N(CH3)2-***CH2***-CH2), 3.02 (br, ***CH2***-NH-CO and ***CH***-O-CO).

FT-IR spectroscopy is a technique based on the absorption in the infrared region (IR) that arises predominantly from excitation of molecular vibrations. The IR region covers wavelengths from approximately 800 nm to 1 mm. It is commonly divided into three sub-regions: near IR, from the visible to 2.5 µm; mid IR, from 2.5 to 25 µm; and far IR, beyond 25 µm. Our analysis was performed between 700 and 4000 nm, in between NIR and mid IR. The IR spectrum derived from FT-IR analysis gave evidence on the molecular structures. In fact, each peak can be related to symmetric and antisymmetric stretching, scissoring, rocking, wagging and twisting of atoms bond to each other. Correct spectrum interpretation allows the comprehension of different groups present in the molecular structure.

Nuclear magnetic resonance spectroscopy is another powerful source of information on the structure and dynamics of molecules. Almost every molecule has at least one magnetic nucleus already in place, sensitive to its surroundings and weakly interacting with them. As such, nuclear spins are ideal probes of molecular properties at the atomic level. NMR spectra of molecules in liquids can give information on the intensities of individual resonances (which depend on the number of nuclei responsible), chemical shifts (the interaction of nuclear spins with an applied magnetic field), spin–spin coupling (their interactions with one another), spin relaxation (the restoration of thermal equilibrium), and chemical exchange (the effects of conformational and chemical equilibria).

4.2.2 Synthesis of PLGA nanoparticles with amino-PVA

The A-OW-ctr sample was synthesized by emulsifying 300 µL of PLGA in ethyl acetate (50.0 mg/mL) with 600 µL of surfactant (amino-PVA 1.0% w/v or a mix of PVA/amino-PVA). This mixture was sonicated (30% amplitude, 15 sec, ice bath) and the obtained oil-in-water emulsion was

dispersed in 60.0 mL of PVA 0.3% w/v. The organic solvent was evaporated under magnetic stirring for 3.5 h.

In a different way, the A-ctr sample were prepared by adding at 300 µL of PLGA solution (50.0 mg/mL) in ethyl acetate 45 µL of PBS 0.1X. The mixture was sonicated at 30% amplitude for 15 sec in ice bath to obtain the primary water-in-oil emulsion. This emulsion was then added to 600 µL of surfactant and ultrasounds were applied with the same protocol described above, to achieve the multiple water-in-oil-in-water (WOW) emulsion. Finally, the WOW emulsion was diluted in the dispersing phase (60.0 mL PVA 0.3% w/v) and the organic solvent was evaporated via magnetic stirring for 3.5 h.

4.2.3 Encapsulation of hydrophobic molecule: curcumin

Curcumin was added as hydrophobic molecule in both OW (A-OW-cur) and WOW (A-cur) samples. A final concentration of 5.0 mg/mL of the drug was obtained by dissolving 1.5 mg of powder in the oil phase.

4.2.4 Encapsulation of hydrophilic molecules: fib-647, FITC

For WOW synthesis A-fib, fib-647 was added at the concentration of 1.0 µM as model molecule. Differently, in A-FITC sample the inner aqueous NPs core was composed by a 0.1 mg/mL solution of FITC, as model fluorophore.

4.2.5 Encapsulation of both hydrophilic and hydrophobic molecules: curcumin and fib-647

The ability of the WOW syntheses to encapsulate simultaneously molecules with different characteristics was tested by adding both curcumin and Fib-647 (A-fib-cur). In this case, the synthetic procedure was similar to those for A-fib, with the addition of 1.5 mg of curcumin at the oil phase.

4.3 Synthesis of PLGA NPs with calcium stearate

C-OW-ctr was obtained by OW method. Firstly, 15 mg of PLGA and 3.0 mg of calcium stearate were dissolved in 300 µL of Span® 60 (1.0 mg/mL in ethyl acetate). The solution was then emulsified with 600 µL of polysorbate 60 (1.6 mg/mL) by ultrasound (30% amplitude, 15 sec, ice bath). The so formed emulsion was diluted with 30.0 mL of D-mannitol 5% w/v and the organic solvent was evaporated via magnetic stirring for 3.5 h.

In a different way, a two step procedure was used to obtain C-ctr, with an inner aqueous core. First, 45 µL of PBS 0.1X were added to the oil phase (300 µL of ethyl acetate, with PLGA 50.0 mg/mL, Span® 60 2.0 mg/mL, calcium stearate 10.0 mg/mL) and sonicated at 30% amplitude for 15 sec in ice bath, to obtain the primary water-in-oil emulsion. This emulsion was then added to 600 µL of polysorbate 60 3.2 mg/mL and sonicated using the same protocol described above, to achieve the multiple water-in-oil-in-water emulsion. Finally, the WOW emulsion was diluted in the dispersing phase (30 mL D-mannitol 5.0% w/v) and the organic solvent was evaporated via magnetic stirring for 3.5 h.

4.3.1 Encapsulation of hydrophobic molecule: curcumin

Curcumin was added in both OW (C-OW-cur) and WOW (C-cur) samples. In details, 1.5 mg of powder were dissolved in the oil phase to obtain a final drug concentration of 5.0 mg/mL.

4.3.2 Encapsulation of hydrophilic molecules: fib-647, FITC

For WOW synthesis (C-fib), fibrinogen linked with Alexa647® (fib-647) was added as hydrophilic model molecule at the concentration of 1.0 µM. Differently, in sample C-FITC the inner aqueous NPs core was composed by a 0.1 mg/mL solution of FITC, as model fluorophore.

4.3.3 Encapsulation of both hydrophilic and hydrophobic molecules: curcumin and fib-647

The ability of the WOW synthesis to simultaneously encapsulate two molecules with different characteristics was tested by concurrent employment of curcumin and Fib-647 (C-fib-cur). In this case, synthetic procedure was similar to those for C-fib, but 1.5 mg of curcumin were additionally added at the oil phase.

4.4 Nanoparticles recollection and purification

For all the described syntheses, NPs were collected and washed with four cycles of centrifugation at 15,000 g for 20 min at 4°C, in order to remove exciding surfactant, as well as not encapsulated drugs and biomacromolecules.

5. Nanoparticle characterization

5.1 Dynamic Light Scattering (DLS)

Immediately after synthesis, the PLGA NPs were thoroughly characterized by Dynamic Light Scattering (DLS) to assess their size and ζ-potential. To this aim, the PLGA NPs pellet was diluted 1 to 1000 in MilliQ water. Measurements were performed with a Malvern Zetasizer Nano ZS90 instrument operating with a light source wavelength of 633 nm and a fixed scattering angle of 90°. All the analyses were run in triplicate.

DLS is a technique based on light scattering that measured hydrodynamic diameter of object ranging from few nm up to 5-6 µm. It is based on the statistical analysis of the scattered light fluctuations in samples of colloidal solution. In fact, particles in suspension undergo Brownian motion caused by thermally induced collisions between the suspended particles and the solvent molecules. These movements are strongly related to the particles size: the smaller the particles, the faster their movements. In this context, particles illuminated with a laser scatter light with an intensity that vary overtime. The rate of this variation is related to the translational diffusion

coefficient (D), thus making possible to calculate the particles hydrodynamic radius (R_h) through the Stokes-Einstein equation:

$$R_h = \frac{K_b T}{3\pi\eta D}$$

where $K_b$is the Boltzmann constant, T is the temperature express in Kelvin, and η is the solvent viscosity.

The diameter obtained by this technique is that of a sphere with the same translational diffusion coefficient of the particle being measured. It is called hydrodynamic diameter because it refers to the way a particle diffuses within a fluid.

DLS analysis results in a statistical distribution of the intensity fluctuations generated by a number of particles. Therefore, NPs size is express as the mean of a size distribution and its polydispersity index (pdI).

A schematic diagram of the DLS apparatus is given in Fig.11.

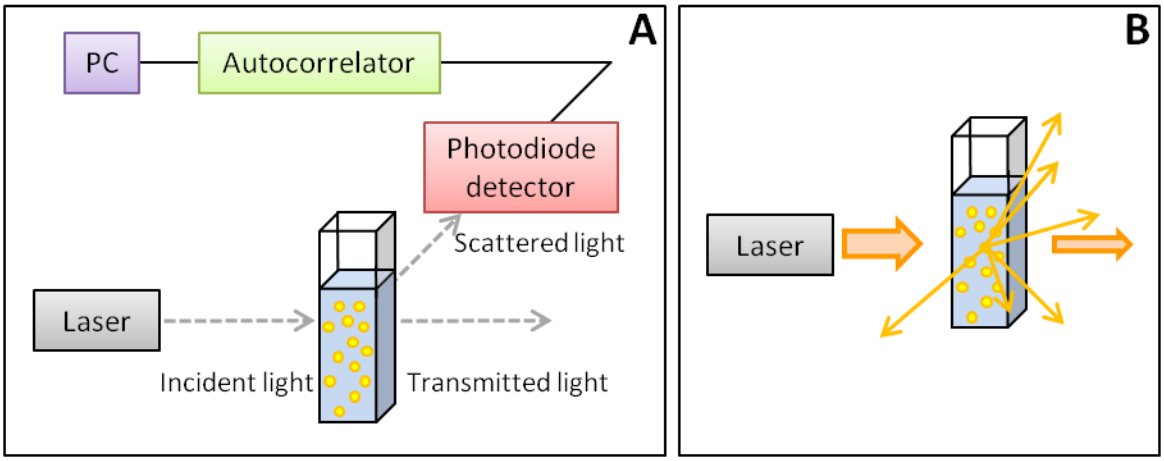

Fig.11. Schematic layout of dynamic light scattering (DLS) setup (the diagram is not to scale). Panel A - The sample is illuminated and the scattered light intensity is detected at 90° from the laser source, and sent to the autocorrelator. The generated autocorrelator function (correlogram)

is then used to calculate the diffusion coefficient. Panel B - Light scattering is the alteration of the direction and intensity of a light beam that strikes an object.

Since the scattered signal can be saturated, the instrument take advantage on attenuation that can vary from 1 up to 11, where 11 indicates no attenuation and 1 maximum attenuation. Accordingly, the scattered intensity and the mean count rate (*i.e.* the mean of the detected photons) recorded during DLS measurements are correct by the attenuator factor. Conversely, by properly correct the mean count rate for the attenuation factor, the Derived Count Rate (DCR) can be calculated. The DCR represents the intensity that would have been measured if no saturation occurred. In this thesis, the DCR was used to compare different analyses made on the same sample during time.

With the DLS apparatus it was possible to measure also NPs surface properties in terms of electrokinetic potential (ζ-potential or surface charge). Fig.12 illustrated the electrical double layer that surrounds stable colloidal particles, and the ζ-potential meaning.

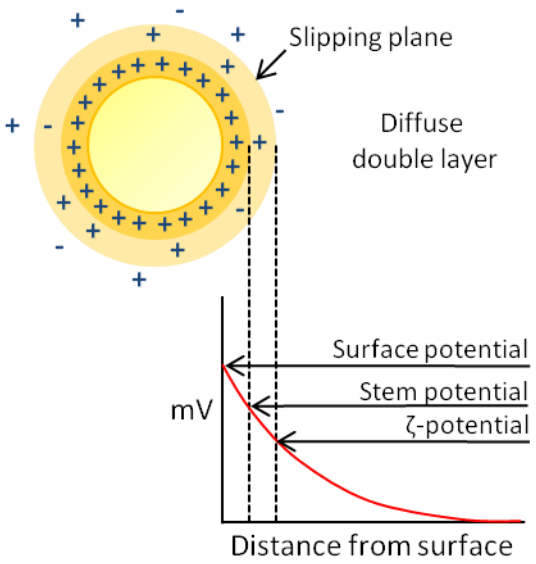

Fig.12. Schematic representation of the electrical double layer that surrounds stable colloidal particles.

Charged groups present in the polymer or in the surfactant used for NPs synthesis are usually present on the NPs surface. These electric charges affect the ions distribution in the surrounding interfacial region, resulting in an increased concentration of counter ions close to the NPs surface (Stern layer). Around each particle, an electrical double layer is then formed. Moreover, a second diffuse layer (Gouy-Chapman layer) of mobile ions is formed on top of the rigid sphere and is generally responsible for the colloid stability of the system. Ions in this outer layer can be displaced as the particle moves through the liquid, whereas the notional boundary (slipping plane) within the diffuse layer represents a stable entity between ions and particle. When a voltage is applied to this particle solution, the charge at the slipping plane is termed zeta (ζ) potential. This is a reliable index to assess NPs surface properties as well as their stability. In fact, ζ-potential values minor than -20.0 mV or higher than +20.0 mV usually ensure electrostatic repulsion between NPs[103–105].

DLS apparatus allows to measure particle mobility by electrophoresis. A Laser Doppler Velocimeter applies an electrical field of known strength across the sample, through which a laser passed. Charged particles in the dispersion will migrate to the oppositely charged electrode with a velocity proportional to the magnitude of the ζ-potential. The measured electrophoretic mobility (μ_e) is related to the ζ-potential by the Henry equation:

$$\mu_e = \frac{2\varepsilon\zeta f(K_a)}{3\mu}$$

where ε is the dielectric constant of the sample, η is the viscosity of the liquid phase, ζ is the ζ-potential, and $f(K_a)$ is the Henry's function.

5.2 Microscopies

5.2.1 Confocal laser scanning microscopy

To investigate the encapsulation of the model drugs, analyses were performed by confocal laser scanning microscopy (Leica TCS SP5 AOBS, Leica Microsystems GmbH) microscopy, thanks to the optical properties of the selected model molecules. Before analyses, PLGA NPs were purified. The NPs pellet was resuspended in MilliQ water (1:200) and dialyzed for three h using a Spectrapor membrane (cut off 100 KDa). The suspensions were then additionally diluted 1:500 and 5.0 µL of the final samples were left drying on a glass slide.

The confocal analyses were obtained with the laser passing through an objective lens 63x, oil immersion, numerical aperture 1.4.

Excitation was obtained by different laser, depending on the fluorophore characteristics, as can be seen in Table1Table3 (for IgG-Cy3 and CD4-FITC see Appendix 1 page 124).

Fluorophore	**Laser**	**Excitation wavelength (nm)**
Curcumin	Argon	458
IgG-488	Argon	488
IgG-Cy3	Diode	561
CD4-FITC	Argon	488
Fib-647	Helium-neon	647
FITC	Argon	488

Table3. Laser and excitation wavelength (nm) used for confocal microscope analysis.

Confocal microscopy is an optical imaging technique based mainly on fluorescence detection. Main advantage in using confocal with respect to other microscopy techniques is related to the

presence of a spatial pinhole placed at the confocal plane of the lens. This allows eliminating out-of-focus light thus increasing optical resolution and contrast.

To better resolve the obtained fluorescent NPs[132], a Leica TCS SP8 microscope equipped with a gated-stimulated emission depletion (STED) module (Leica Microsystems GmbH, Germany) an HCX PL APO 100x/1.4 OIL STED ORANGE objective, a white light laser (WLL) source, and a 592 nm depletion laser was additionally employed. The STED images were acquired using the hybrid detectors with a pixel size of 25 nm. To prepare samples for STED analysis, after the purification steps describe above PLGA NPs suspensions were deposited onto a glass coverslip and left drying for 1h. One drop of ProLong® Gold was then added, another glass coverslip was placed above and samples were allowed to cure in the dark for 24 h.

5.2.2 Scanning Electron Microscopy

Scanning electron microscopy (SEM, Zeiss Sigma, Carl Zeiss NTS GmbH) was used to assess PLGA NPs morphology. Before analyses, PLGA NPs were purified with the same procedure described for confocal analysis samples in paragraph 5.2.1. In this case, 5.0 µL of the final samples were left drying on a silicon support. Before the SEM analysis, samples were placed in a vacuum pump for 2 h. All of the SEM images were acquired with an accelerating voltage of 1 kV. In some cases, dimensional distribution of PLGA NPs was calculated, by meaning of the open source software Image J.

A scanning electron microscope scans the samples with a focused beam of electrons that interact with sample atoms. This produces a variety of signal that can be detected and elaborated to return samples surface topography and composition, as well as samples morphology. In fact, by the combination of beam's position and detected signal it is possible to obtain high resolution images.

6. Degradation studies

To assess NPs degradation, PBS 1X at pH 7.4 was chosen as medium mimicking physiological conditions (dilution 1 to 1000) and samples were incubated at 37°C under continuous rotation (100 rpm). At determined time points, each sample was analyzed by DLS and/or SPES.

6.1 Dynamic Light Scattering

Several parameters including the absolute number of detected photons (*i.e.* the derived count rate, DCR) as well as size and correlogram shape were considered to establish the NPs stability during time.

Moreover, DLS was used to assess PLGA NPs stability in medium at different pH values.

6.2 Single Particle Extinction and Scattering (SPES)

Before performing the degradation studies with Single Particle Extinction and Scattering (SPES), each PLGA NPs batch was added with 1.0% w/v D-mannitol as cryoprotectant and lyophilized. For comparison purpose, same treatment was reserved before DLS analysis. Analysis by SPES was run after an additional dilution 1 to 500 in PBS with respect to the 1 to 1000 dilutions for DLS analysis.

SPES is a method for the characterization of NPs that is based on the analysis of the forward scattered fields[133–135]. A schematic diagram of the SPES apparatus is given in Fig.13.

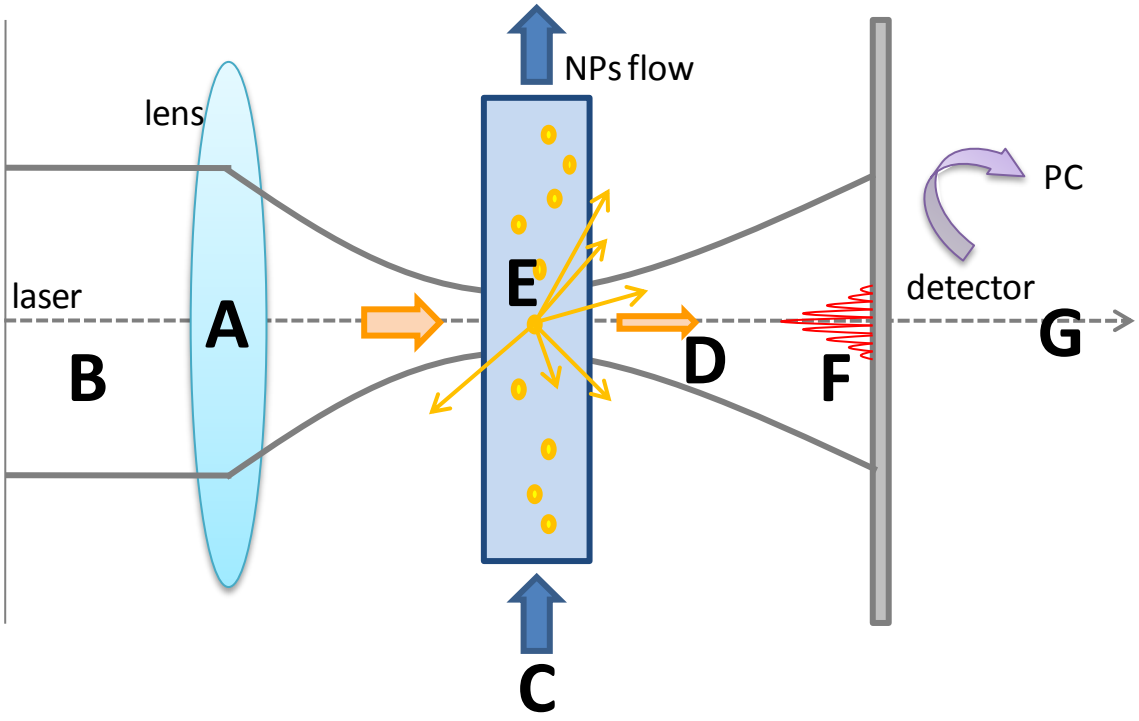

Fig.13. Schematic representation of the SPES apparatus. Particles (C) are driven through a tightly focused laser beam (B); the scattered (E) and transmitted (D) fields interfere (F) onto a segmented detector (G).

A lens (A) focuses a laser beam (B) into a flow cell (C), through which the sample is driven at constant speed. The superposition of the faint scattered light by each single nanoparticle (E) and the intense transmitted field (D) generates time dependent interference patterns (F) on a segmented photodetector (G), thus generating corresponding electrical signals. The light intensity modulations due to the interference are proportional to the amplitude of the forward scattered field of the single particles driven through the scattering volume. In addition, the power reduction of the entire beam, which rigorously gives the total extinction cross section of the particles, provides enough information for a complete characterization of the scattered field.

A dedicated data analysis recovers the basic features of the complex scattered field in terms of its real and imaginary parts. In this way SPES can be employed to realize the complex field approach and to precisely determine two independent parameters for each particle: the extinction cross section and the optical thickness of the particle. The latter is defined as the product

$$s = d (m - 1)$$

where d is the particle diameter and m is the refractive index relative to the surrounding medium. Especially for spherical NPs, from the combination of the two measured parameters, it is possible to estimate the average refractive index of each particle, thus determining the actual particle size with a better accuracy compared to traditional scattering methods. The single particle approach guarantees higher accuracy and resolution, avoiding artifacts due to the invention algorithms required for the analysis of the correlation function as in the case of DLS. SPES method is particularly promising for polydisperse samples, as well as in cases of particles mixture with different compositions and shapes. Finally, single particle approach is able to discriminate between NPs and impurities that present different refractive index, thus allowing analysis of suspensions in complex media (*i.e.* serum, plasma, cells growth medium).

In the case of PLGA NPs degradation studies, SPES was selected as additional analytical technique. In fact, during the degradation process NPs relative refractive index is supposed to decrease, even if this not necessarily results in a variation in NPs size. This means that SPES can observe variation in the PLGA NPs that a classically used technique, such as DLS, is not able to measure.

7. Release studies

In vitro drug release of model drugs, such as curcumin and fib-647, was evaluated by the dissolution technique[136] and followed through spectrofluorimetry (FluoroMax 4, Horiba, JobinYvon).

The release experiments were performed by suspending five µL of the NPs pellet in 5.0 mL of PBS 1X with 5.0 w/v D-mannitol and incubating at 37°C under continuous rotation (100 rpm). At specific time points (0, 2, 4, 7, 24, 168, 336 h) 1.0 mL was taken and centrifuged at 15,000 g for 15 min (25°C). In order to maintain the NPs concentration, the resultant pellet was resuspended in

1.0 mL of fresh medium and added again at the original samples. Instead, the supernatants followed different fate dependently on the nature of the model drugs.

Released curcumin was extracted by means of chloroform and analyzed by spectrofluorometer (excitation 450 nm, emission 460-600 nm) after appropriate dilution.

Differently, released fib-647 was directly analyzed in the aqueous phase, without extraction (excitation 647 nm, emission 660-800 nm).

Samples were run in triplicate and data are presented as mean±standard deviation (SD).

Fluorescence is a form of luminescence, which is defined as the emission of light from any substance. In particular, fluorescence is related to the emission of photons from singlet-excited states. The electron in the excited orbital is paired (of opposite sign) to the second electron in the ground-state orbital. Return to the ground state is spin-allowed and occurs rapidly by emission of a photon. The emission rates of fluorescence are typically 10^8 s^{-1}, so that a typical fluorescence lifetime is near 10 nsec. Basic fluorescence spectral data are generally presented as emission spectra. The intensities and wavelengths of these spectra can vary widely depending on the chemical structure of the fluorophore and the solvent in which it is dissolved.

7.1 Calibration curve for curcumin

In order to perform a quantitative analysis of the cumulant release, calibration curves were obtained.

Curcumin calibration curve were prepared by starting from a stock solution at 50.0 pg/mL in chloroform. Different concentrations were tested: 40.0, 35.0, 30.0, 25.0, 20.0, 15.0, 10.0, 5.0, and 0 pg/mL.The obtained calibration curve was linear with a Pearson's coefficient of 0.99923 and defined by the equation y=28442.11*x+38264.10 (Fig. 14, n=5).

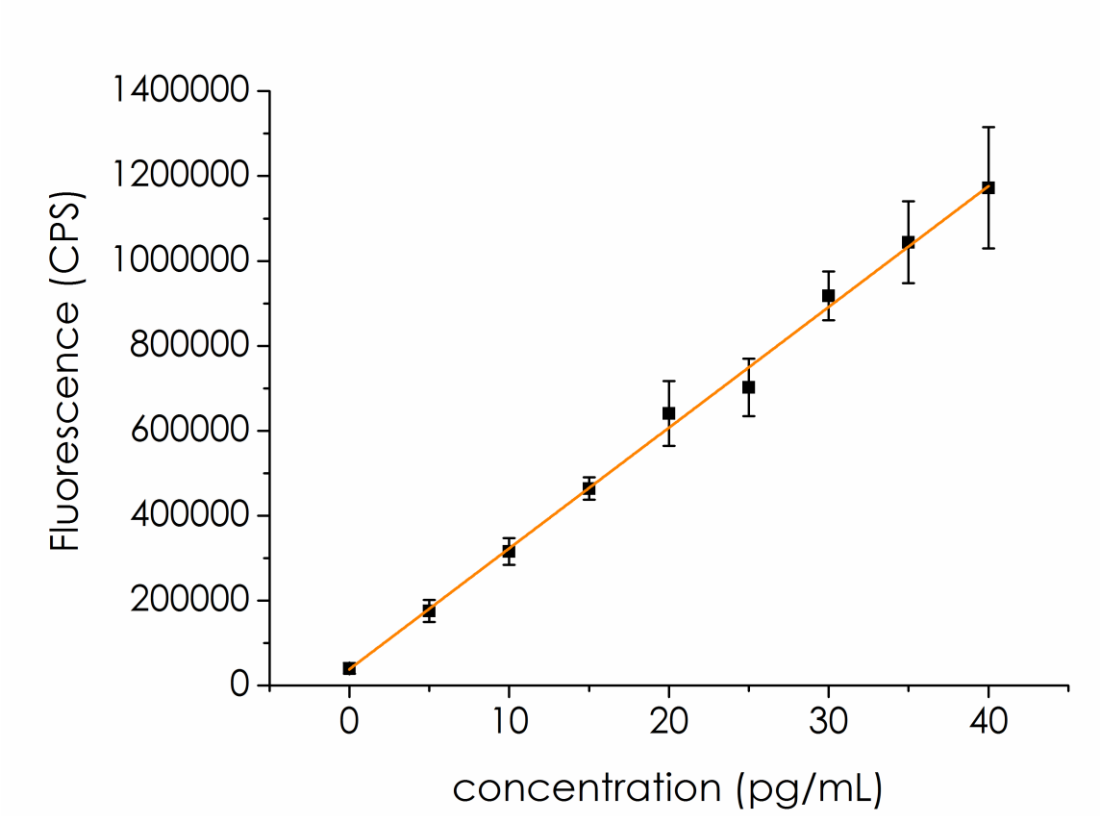

Fig. 14. Curcumin calibration curve. Data are means±SD (n=5)

7.2 Calibration curve for fib-647

Differently, for the fib-647 calibration curve, aqueous 10.0 nM solution was prepared as a stock and the tested concentrations were: 7.0, 6.0, 5.0, 4.0, 3.0, 2.0, 1.0, 0.5, and 0 nM. In this case, calibration curve had a Pearson's coefficient of 0.99396 and was defined by the equation y=171474.93*x-58771.31 (Fig. 15, n=5)

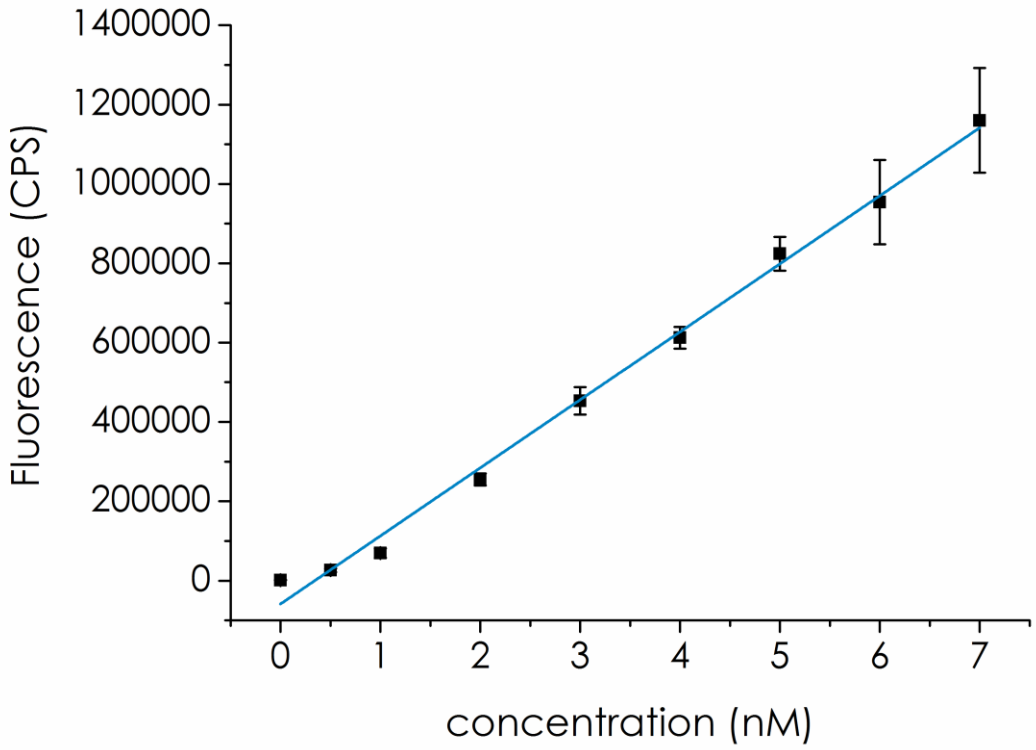

Fig. 15. Fib-647 calibration curve. Data are means±SD (n=5)

8. Surface modifications: protein corona and D-mannose

In order to decorate NPs surface with molecules recognized by TAMs and macrophages, NPs were incubated with a solution of 10.0% v/v FBS and 20.0% w/v D-mannose (FBSM). NPs were suspended in the medium and incubated for 24 h at 37°C under mild rotation (100 rpm). Samples purification from exceeding macromolecules was performed by centrifugation (five cycles at 15,000 g, 15 min, 4°C). For comparison, also different conditions were tested, namely 10.0% v/v FBS without D-mannose (FBS), 100% FBS with (100FBSM) and without (100FBS) 20.0% w/v D-mannose, 20.0% w/v D-mannose (M).

8.1 Dynamic Light Scattering

Analyses to assess surface functionalization were performed by means of DLS in terms of size and ζ-potential.

8.2 X-ray photoelectron spectroscopy (XPS)

In addition, X-ray photoelectron spectroscopy (XPS) spectra were analyzed on samples with a D-mannose decorated surface. NPs were purified by dialysis as described in the 5.2.1 Confocal laser scanning microscopy page 58 in the Materials and Methods section. The NPs pellet was resuspended in MilliQ water (1:200) and dialyzed for three h using a Spectrapor membrane (cut off 100 KDa). The suspensions were then additionally diluted 1:500 and the final samples were left drying on a silicon support, so that surface was completely covered by NPs. Analyses were run with a UHV apparatus Leybold LH 10/12, X-ray source Mg Kα = 1253.6 eV, Pass Energy = 30 eV, Energy resolution 0.7 eV.

Photoelectron spectroscopy is a molecular spectroscopic method based on photoionization. If an atom or molecule is irradiated with photons of energy higher than the ionization energy of the particle, ionization may occur. Types of photoelectron spectrometers are distinguished on the basis of the energy of the radiation sources. When X-ray photons are used for core electron ionizations, photoelectron experiments are called X-ray photoelectron spectroscopy, XPS. This technique can provide information about the elemental composition, empirical formula, chemical state and electronic state of the elements that exist within a material.

9. *In vitro* cytotoxicity studies

For cytotoxicity studies, RAW264.7 (American Type Culture Collection, ATCC) murine macrophages were selected as a model cell line. Cells were grown overnight in Dulbecco minimal essential medium (DMEM) containing 10.0% v/v fetal bovine serum (FBS) and 2 mM glutamine.

In addition, primary culture of mouse bone marrow-derived macrophages was investigated. Female Fvb/Hd mice were sacrificed with CO_2 and bones were collected. After cleaning from exceeding muscles and ligaments, bones were smashed with a pestle, cleaned with PBS and the bone marrow was filtered in a 70 µm cell strainer. Red blood cells were removed with NaCl gradient and remaining cells were suspended in their grown medium (high glucose DMEM supplemented with 20.0% v/v lowendotoxin fetal bovine serum, 30.0% v/v L929-conditioned medium, 1.0% v/v glutamine, 1.0% v/v Pen/Strep, 0.5% v/v sodium pyruvate, and 0.1% v/v b-mercaptoethanol). Cultures were fed with 2.5 mL of fresh medium every 2 days. Stimulations were carried out at day seven.

To assess PLGA NPs cytocompatibility a [3-(4,5-dimethylthiazol-2-yl)-2,5-diphenyltetrazolium bromide] (MTT) test (Roche) was performed. Macrophages (both RAW264.7 and bone marrow-derived) were plated at a cell density of 1 x 10^6 cells/mL into 96-well plate. After appropriate proliferation at 37°C in 5% CO_2 and 98% air-humidified, cells were treated with 10 µL of different PLGA NPs suspensions, as well as positive (EtOH, DMSO, as cytotoxic agents) and negative (PBS) controls. Two dilutions in PBS 1X pH 7.4 were tested, namely 1 to 10 and 1 to 100. Cytotoxicity test was conducted by following manufacturer instruction after 24 h. Colorimetric analysis of the formazan product was performed with a TECAN sunrise spectrophotometer at 550 nm.

The MTT reduction assay was the first homogeneous cell viability assay developed for a 96-well format. The MTT substrate is prepared in a physiologically balanced solution, added to cells in culture and incubated for 4 h. Viable cells with active metabolism convert MTT into a purple colored formazan product with an absorbance maximum near 570 nm. Ability to convert MTT into formazan is conversely lost in died cells, thus color formation is a valuable marker for viable cells. The quantity of formazan, presumably proportional to the number of viable cells, is measured by recording changes in absorbance using a plate reading spectrophotometer.

Results and discussion

1. PLGA NPs synthesis with PVA: parameters investigation

Selected technique for PLGA NPs synthesis was the emulsion-solvent evaporation method. This synthesis allows the encapsulation of hydrophobic and/or hydrophilic molecules by properly varying synthetic parameters. In particular, attention was focused on single emulsion (oil-in-water, OW) synthesis to encapsulate the hydrophobic drug curcumin, while double emulsion (water-in-oil-in-water, WOW) method was employed for biomacromolecules, such as RNA or model antibodies.

In the optimization of the synthetic parameters, the well-known surfactant PVA was selected to study the PLGA behavior in both OW and WOW synthesis. Accordingly, experiments were run by systematically change different key steps of the synthetic procedure (Fig.16). A brief summary of the experimental conditions employed in NPs synthesis is reported in Table4.

Parameter	**Starting condition**
PLGA Molecular Weight	38-54 KDa
PLGA concentration	50.0 mg/mL
Organic solvent	Ethyl acetate
Primary aqueous phase (for WOW synthesis)	Saline solution composed of 0.1 M sodium phosphate, 0.1 M NaCl and 5.0 mM sodium azide (pH 8.3)
Surfactant	PVA 31 KDa, 1.0% w/v
Ultrasounds application	20% amplitude
Cooling bath	Ice bath
Freeze-drying	No freeze-drying

Table4. Summary of PLGA NPs synthetic conditions in the initial formulation. To note, each parameter was varied while keeping all other parameters constant.

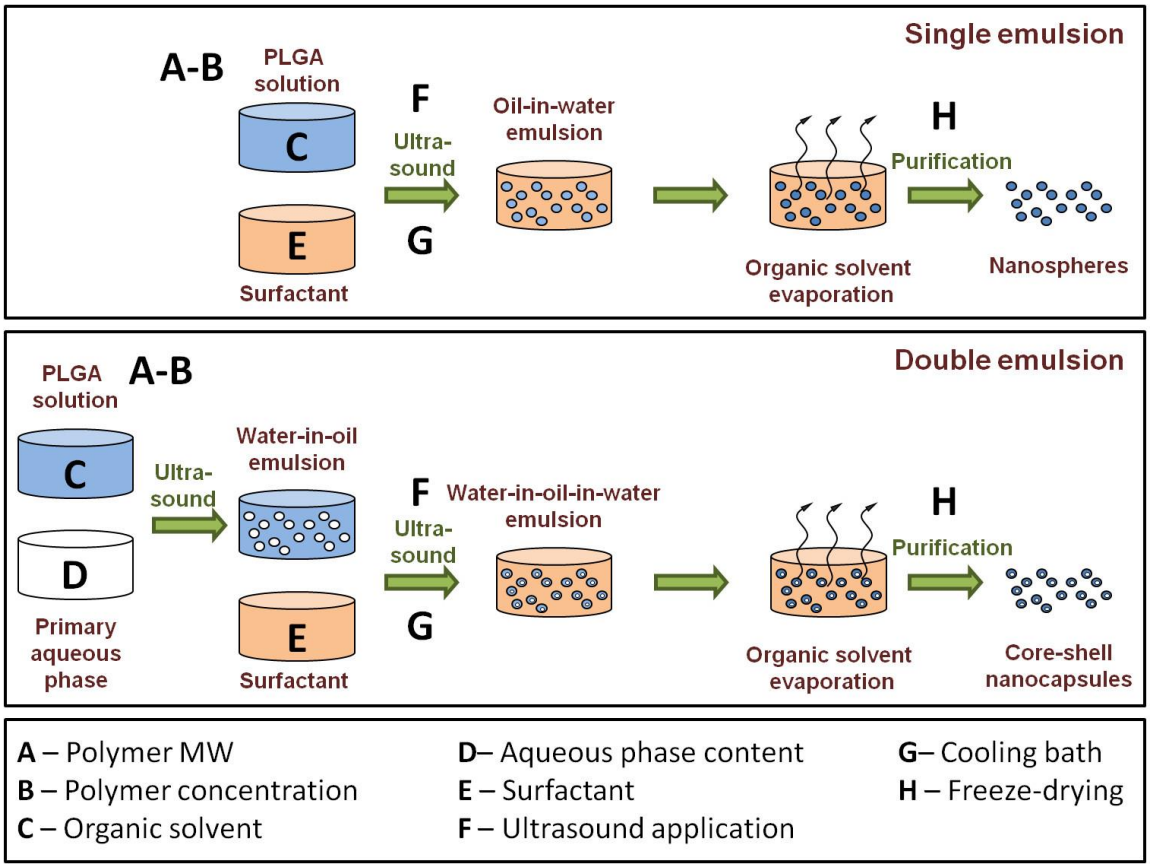

Fig.16. Schematic representation of both single and double emulsion syntheses. Letters underlined the different synthetic steps that were investigated.

To select the most suitable formulations for drug/gene delivery, two main criteria were used. Firstly, NPs size and size distribution were examined, since they are closely related to NPs release properties[94]. In this regard, parameters as obtained by DLS analyses, such as z-average, peaks diameter size, polydispersity index (pdI) as well as the presence of more than one peak, were considered. Secondly, the NPs stability in a medium mimicking physiological conditions (PBS 1X pH 7.4) was investigated.

1.1 PLGA molecular weight

PLGA applications in drug delivery are affected by its physical properties, and especially its MW[87]. Accordingly, PLGA with low (7-17 KDa), medium (38-54 KDa) and high (190-240 KDa) MW were tested.

In OW synthesis, the higher the PLGA MW, the higher the NPs size and polydispersity (Table 5, samples 5A, 5B and 5C).

	Synthesis	**MW (KDa)**	**z-average (nm)**	**Peaks (nm)**	**PdI**
5A	OW	7-17	315.7	328.0	0.170
5B	OW	38-54	328.7	321.4	0.220
5C	OW	190-240	437.9	384.8	0.311
5D	WOW	7-17	930.6	224.2+910.4	0.874
5E	WOW	38-54	484.1	228.1+1225	0.595
5F	WOW	190-240	445.2	334.1+5252	0.434

Table 5. PLGA NPs obtained with different PLGA MW. NPs size was reported as z-average and peaks size, whereas size distribution was indicated by polydispersity index (pdI).

On the contrary, in WOW synthesis, NPs presented very high polydispersity for all the tested PLGA MW, which strongly affected z-average reliability. Accordingly, to assess NPs diameter, the principal peak size was considered. No differences were observed between low and medium MW (samples 5D and 5E), while high MW PLGA originated larger NPs (sample 5F).

According to results reported in Table 5, PLGA having medium MW (38-54 KDa) was chosen for further investigation, because it provided NPs with promising features either by OW or WOW methods.

1.2 Ultrasounds application

In emulsion-solvent evaporation synthesis for PLGA NPs, it is necessary to provide energy by sonication or homogenization for inducing the formation of nano-sized droplets that in turn resulted in NPs after solvent evaporation. In this work, ultrasounds were applied by means of an ultrasonic probe. To note, no stable emulsion was obtained in the absence of ultrasounds application, since unstable replicates and a very high pdI (0.821) were observed by DLS. Low energy (20% amplitude) was sufficient to form emulsion; however, NPs showed high polydispersity (pdI 0.595) and size (z-average 484.1 nm). By increasing the amplitude up to 30%, NPs showed an improvement in polydispersity (pdI lower than 0.2) and a reduction in size up to 300 nm. Accordingly, this amplitude was selected as the best one.

1.3 PLGA concentration

In WOW synthesis, when using PLGA 200.0 mg/mL, micron sized particles were obtained (z-average 1,084 nm). Differently, if 5.0 mg/mL of PLGA were used, NPs had dimensions in the nano range (z-average 191.7 nm); however, they were not stable and degraded in less than 24 h. The corresponding OW synthesis with the same PLGA concentration (5.0 mg/mL), showed NPs with a slightly increase in size (z-average 223.6 nm). An intermediate concentration, namely 50.0 mg/mL, allowed the formation of PLGA NPs with size 233.8 nm for WOW (P1-ctr) and 223.3 nm for OW (P1-OW-ctr) syntheses. Notably, these formulations were found to be stable for one week in PBS at 37°C, therefore they were considered compatible with further applications in gene/drug

delivery. Consequently, the PLGA concentration of 50.0 mg/mL was selected for all the following experiments.

1.4 Organic solvent

One of the most commonly used solvent in PLGA NPs synthesis by emulsion-solvent evaporation method is dichloromethane (DCM). This solvent is completely immiscible with water, thus resulting suitable for emulsion formation. Although DCM presents a boiling point of 39.6°C that guarantees rapid evaporation, safety concerns are raised with its use. In this thesis a safer alternative to DCM, ethyl acetate, was investigated. While ethyl acetate traces are considered acceptable also in food[137], chlorinate solvents such as DCM are carcinogenic and highly toxic[138] and it is fundamental that all the solvent molecules are eliminated from the final product. Besides the safety issues, experimental evidences showed that ethyl acetate was advantageous from the technological point of view. In fact, to obtain NPs of around 200 nm size in both OW and WOW synthesis, a reduced amount of PVA (1.0% w/v) and applied energy by ultrasounds (15 sec) were required by using ethyl acetate with respect to DCM (4.0% w/v PVA and 90 sec of ultrasounds). This is possibly due to the fact that, differently from DCM, ethyl acetate is slightly diffused in water[139], thus helping interaction between the organic phase containing PLGA and the aqueous one. By taking into account the overall milder conditions in which the syntheses were performed, ethyl acetate was definitely selected as organic solvent for further experiments.

1.5 Cooling bath temperature

Mechanical waves in ultrasound application induced heating in the reaction mixture, thus potentially interfering with emulsion formation and stability. This is of particular importance in double emulsion synthesis, where biomacromolecules need to be loaded in the PLGA NPs. In fact, one of the major problems in protein and gene encapsulation is represented by harsh synthetic conditions that can degrade their structure. Another important issue in WOW synthesis is that the

primary aqueous phase tends to immediately disperse in the secondary aqueous phase, thus reducing the encapsulation efficiency. It was hypothesized that the use of a cooling bath during ultrasound application, having a temperature lower than the freezing point of the primary aqueous phase but higher than the freezing point of PLGA/ethyl acetate solution, may freeze and stabilize the first emulsion. Accordingly, improvement in NPs stability and encapsulation efficiency can be achieved. In this regard, different cooling baths were investigated: Ethylene glycol/CO_2 (t = -15°C); CH_3CN/CO_2 (t = -41°C); ice bath (t = 0°C).

Resulted syntheses are reported in Table 6.

	Cooling bath	**Inner core**	**z-average (nm)**	**Peak (nm)**	**PdI**
6A	CH_3CN/CO_2	IgG1-488	237.6	248.2	0.031
6B	Ethylen glycol/CO_2	H_2O	231.8	244.2	0.048
6C	Ethylen glycol/CO_2	IgG1-488	184.6	195.8	0.068
6D	Ice bath	IgG1-488	233.8	245.3	0.026

Table 6. Main DLS characteristics of PLGA NPs synthesized using different cooling baths. NPs size was reported as z-average and peaks size, whereas size distribution was indicated by polydispersity index (pdI). Being core-shell NPs, the inner core content is also reported.

All the tested syntheses provided NPs with small size and narrow size distribution. Use of CH_3CN/CO_2 cooling bath was discarded, because during synthesis the first emulsion froze. This was unexpected, being the ethyl acetate freezing point -83.6°C. Evidently, the presence of PLGA in the solution changed the solvent properties, including the freezing point. Synthesis was possible because first emulsion immediately thawed when PVA was added as secondary aqueous phase.

Confocal characterization (see paragraph 1.7 Encapsulation of hydrophilic molecules: IgG1-488, vegetal RNA page 76 of the Results and discussion section) of samples 6C and 6D showed fluorescent spots, indicating that both synthetic methods with ice bath and ethylene glycol/CO_2were equally effective for encapsulating fluorescent molecules. Considering that ice

bath is cheaper and more easy-to-access with respect to the combination ethylene glycol/CO_2, it was selected for all the following syntheses.

1.6 Surfactant role

1.6.1 PVA with low molecular weight and high hydrolysis rate

Although PVA is a biocompatible polymer, its degradation requires long time[140], and elimination from the organism generally occurs via renal excretion. In this context a molecule with small MW is supposed to be eliminated more easily. Accordingly, besides PVA 31 KDa, PVA 22 KDa was tested in PLGA NPs.

In case of WOW synthesis, DLS analysis showed two peaks (320.8 nm and 1585 nm) and high polydispersity (pdI 0.371), indicating that this surfactant does not stabilize the emulsion. When OW synthesis was investigated, results were even worst and no stable emulsion was obtained (Fig. 17).

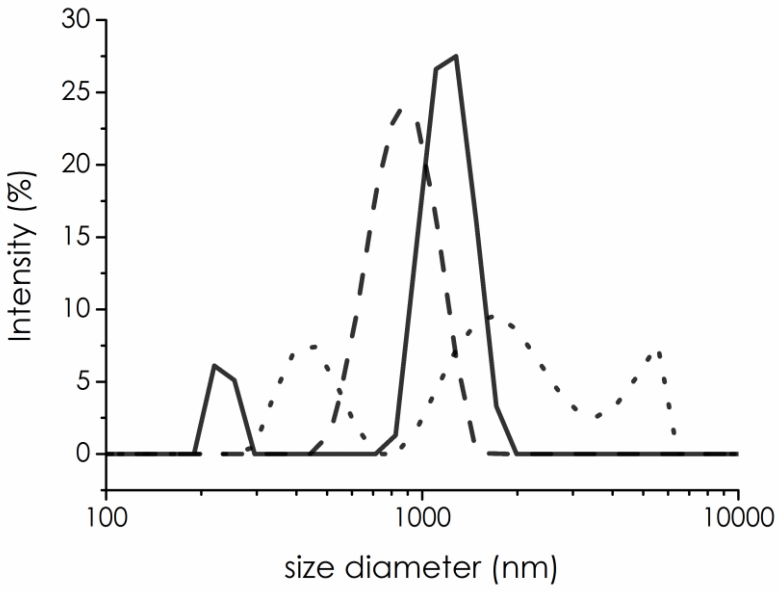

Fig. 17. DLS size distribution for P-ctr synthesized with PVA 22 KDa. The analyses showed no NPs formation. Curves referred to three different technical replicates.

PVA 22 KDa was different from PVA 31 KDa not only for the MW but also for the degree of hydrolysis of the residual acetyl groups. In fact, while PVA 31 KDa had a partial hydrolysis (86.7-88.7 mol%), PVA 22 KDa was totally hydrolyzed (98 mol%). Since the degree of hydrolysis in PVA has strong influence on the solubility and the swellability of the polymer, it can strongly influence the PVA behavior in water, thus interfering with its role in emulsion formation.

According to these findings, PVA 31 KDa was used for all the following syntheses.

1.6.2 PVA percentage

Finally, the role of PVA as surfactant was investigated by testing PVA solutions with different w/v concentrations. As previously reported[110,122,141–144], this was found to be the fundamental parameter for modulating NPs size and stability.

In the absence of surfactant, even if the secondary WOW emulsion was milky, after solvent evaporation many aggregates were observed and DLS analysis showed unstable peaks and high polydispersity (Fig. 18).

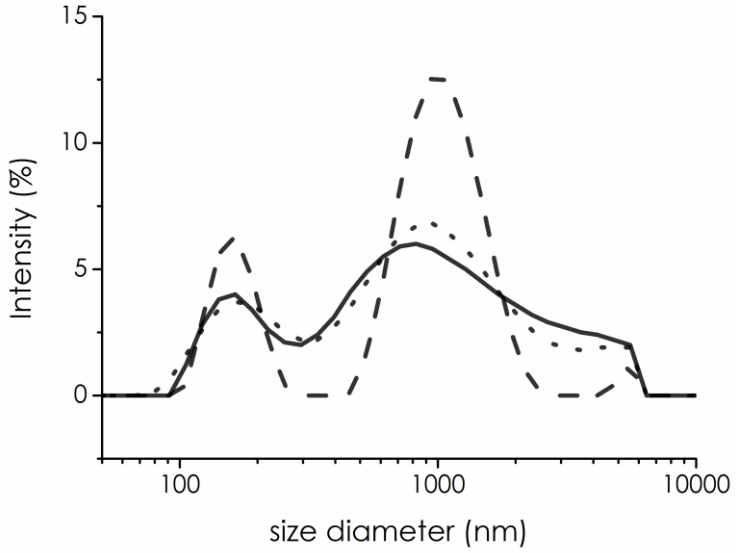

Fig. 18. DLS size distribution of PLGA NPs synthesized in the absence of surfactants. Curves referred to three different technical replicates.

Interestingly, this synthesis resulted in a -53.0 mV ζ-potential that was much more negative than the values found when PVA was employed, in which ζ-potential ranged from 24.6 to -31.0 mV. When the PVA concentration was varied from 1.0 to 0.1% w/v, the hydrodynamic diameter of NPs synthesized by OW ranged from 236.7 to 678.1 nm, respectively. Therefore, the more surfactant was added, the smaller the NPs were (Fig. 19). PdI ranged from 0.069 to 0.197, thus indicating very narrow polydispersity.

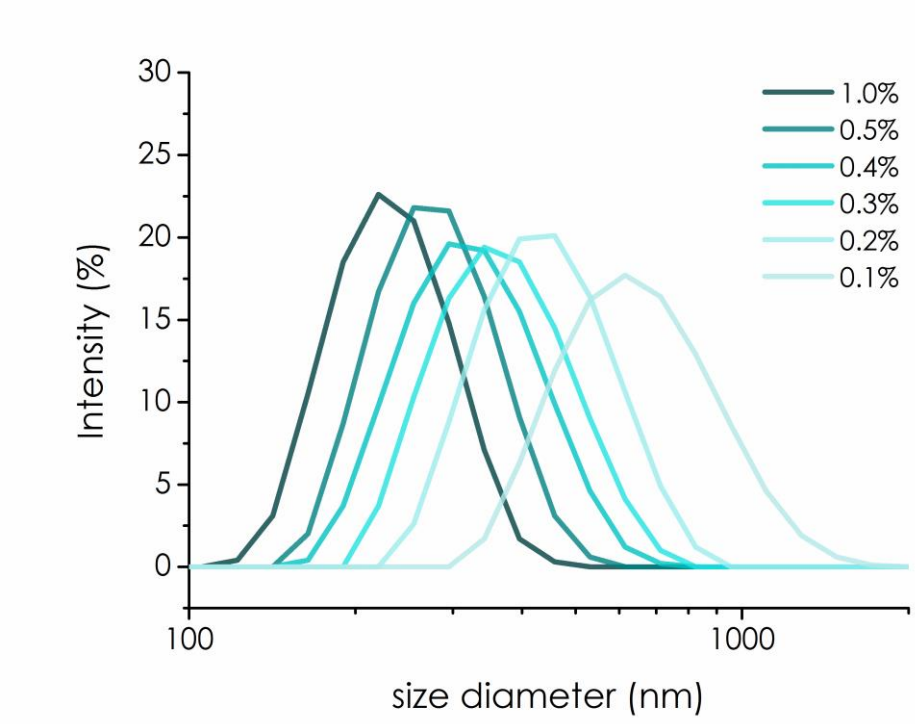

Fig. 19. DLS size distribution with different amount of PVA. PLGA NPs size was found to be reduced by increasing the PVA concentration from 0.1 to 1.0% w/v.

1.7 Encapsulation of hydrophilic molecules: IgG1-488, vegetal RNA

The fluorescent labeled antibody IgG1-488 was encapsulated in P1-IgG-488, to evaluate WOW synthesis ability to encapsulate hydrophilic molecules in the inner aqueous core. As assessed by

confocal analysis (Fig. 20), fluorescent spots were detected in correspondence to nanoparticles as visualized in the contrast phase channel, thus indicating that the model molecule was actually internalized in the NPs.

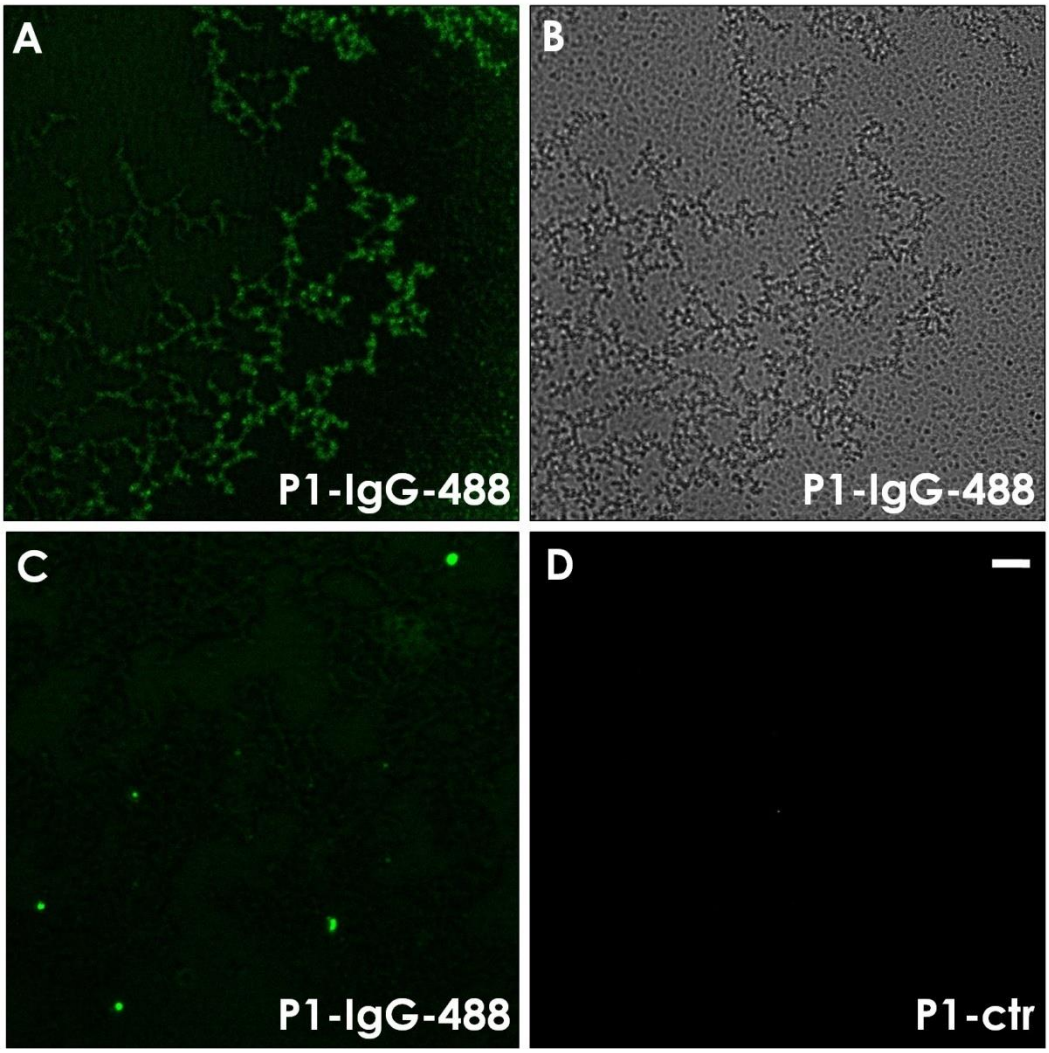

Fig. 20. Confocal characterization of P1-IgG-488 and P1-ctr. Fluorescent spots were correspondent to PLGA NPs, as assess by contrast phase images (panel A and B, sample 6C). Panel C referred to sample 6D. Panel D referred to the control (P1-ctr), where no fluorescence was observed. Scale bar is 5 µm.

As previously discussed, the use of siRNA to silence gene expression and normalize TAMs abnormal phenotype was considered a valuable alternative to TAMs depletion for cancer therapy. Accordingly, a mixture of RNA extracted by Arabidopsis (vegetal RNA) was encapsulated into PLGA NPs as model molecule. P1-vRNA showed a z-average of 197.5 nm and a very good monodispersity (pdI 0.022); therefore, they looked promising for future investigations.

2. PLGA NPs synthesis with PVA: degradation studies

PLGA NPs degradation properties are very important parameters in order to determine their potential for drug delivery. In fact, PLGA NPs must be stable in the bloodstream and fast degrade after endosome internalization, to release their content in the cell cytosol. Accordingly, PBS 1X at pH 7.4 was selected as medium mimicking physiological conditions and in particular bloodstream environment.

Degradation experiments were monitored by DLS analysis and several parameters were considered to establish the NPs stability during time, including the absolute number of detected photons (*i.e.* the derived count rate, DCR) as well as size and correlogram shape.

Fig. 21 showed that a very sharp decrease in the DCR occurred during the first 24-48 h for all the tested formulations, namely P1-vRNA, P1-IgG-488, P1-ctr and P1-OW-ctr. Then DCR decreased more slowly until a complete NPs degradation took place, as confirmed by the collection of an insufficient number of photons. Noteworthy, the more stable formulations were those with a core-shell structure and model molecules encapsulated. In fact, P1-IgG-488 and more evidently P1-vRNA were found to have the longest degradation time. Accordingly, these samples looked promising for potential *in vitro* and *in vivo* applications.

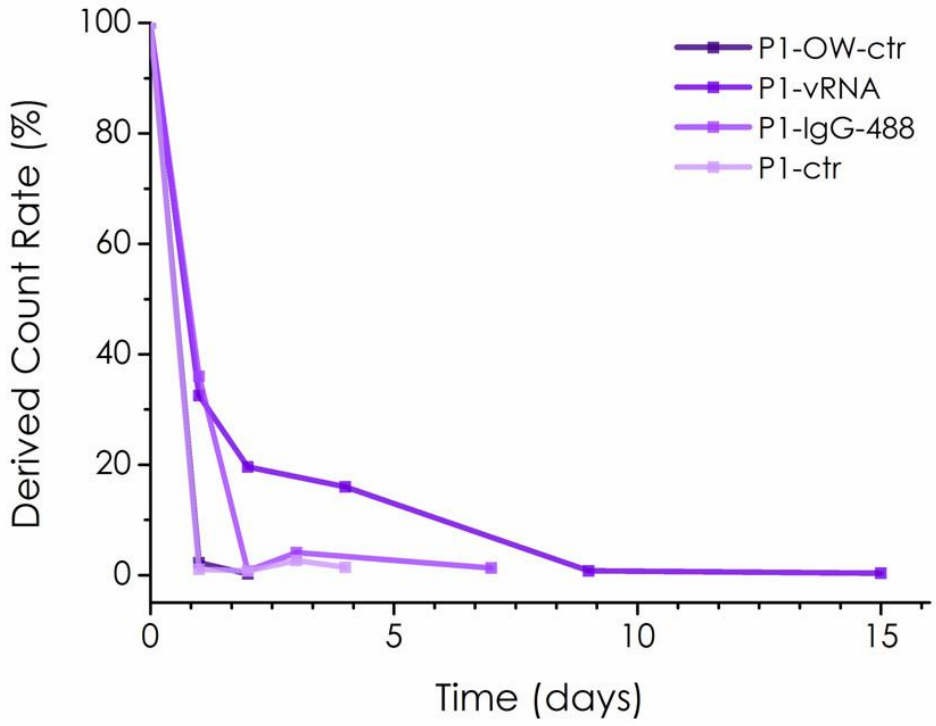

Fig. 21. Degradation profile of different PVA stabilized PLGA NPs. Notably, the degradation profiles of P1-OW-ctr and P1-ctr are partially superimposed.

2.1 Stability at different pH values

PLGA degradation mechanism takes place through hydrolysis of the ester bonds between the two monomers, lactic and glycolic acid. It is well established that ester bonds are susceptible to both acidic and basic conditions. P1-ctr stability was thus checked at different pH values, namely 8.5, 7.5, 6.5, 5.5, 4.5 and 3.5. PBS 0.01X was used as buffer and pH was adjusted by sodium hydroxide or hydrochloric acid, as appropriate.

At pH 7.5, degradation followed the trend already observed and presented in Fig. 21: DCR decreased quite rapidly during the first 24 h, then sample was stabilized for some days, until

complete degradation was observed at day 8. On the contrary, for all the other tested pH values, P1-ctr was stable for less than 24 h. This was partially expected, because pH variation accelerated the hydrolytic process. Since tumor environment is slightly more acidic with respect to the blood[62,71,8] and endosomes show pH around 5-6, PLGA NPs able to degrade in these conditions are good candidates for tumor targeting and cytosolic release of their content.

2.2 Stability after freeze drying

Freeze-drying is a widely used procedure for improving the stability of different products including colloidal carriers. However, the process is relatively slow and expensive and its application is limited to products with a high added value[145]. P1-ctr and P1-IgG-488 were selected as candidates to assess if freeze-drying process was able to modulate PLGA NPs degradation. Both the samples were lyophilized with the addition of 5.0% w/v mannitol as cryoprotector.

After resuspension in PBS 0.1 X pH 7.4, both P1-ctr and P1-IgG-488 underwent rapid degradation and DCR after 24 h was too low to complete the DLS analysis. Similar results were observed for PBS at different pH values, namely 6.5 and 5.5, as well as for 0.9% w/v NaCl.

Notably, when degradation experiment (P1-ctr) was performed without rotation, a different profile was observed (Fig. 22). In fact, the sample showed a progressive degradation during time, lasting for three days. The forth day, DCR was too low, therefore no further DLS measurements were performed.

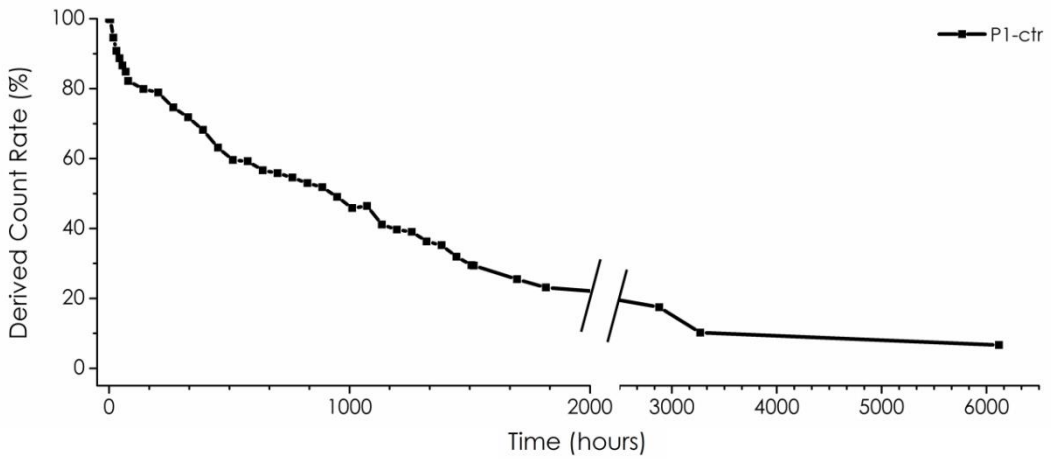

Fig. 22. P1-ctr degradation profile in static conditions. Before the analysis, samples were freeze-dried with 1.0% w/v of D-mannitol as cryoprotectant.

2.3 DLS vs. SPES

Although DLS is an easy-to-use and powerful technique for the rapid characterization of NPs size, it does not provide any qualitative changes in terms of NPs composition and polymer degradation. For a more efficacious monitoring of NPs degradation, an alternative method (single particle optical extinction and scattering, SPES) was tested. To this purpose, NPs were synthesized with 0.2% w/v PVA as surfactant by both OW and WOW emulsion method. Curcumin as hydrophobic molecule was encapsulated in solid (OW) NPs, while IgG1-488 was selected as model biomacromolecule for core-shell (WOW) systems.

Before performing dedicated analyses of degradation, PLGA NPs were thoroughly characterized by DLS. To note, the P0.2-OW-cur exhibited larger size with respect to the control (P0.2-OW-ctr) and the pdI values were low for both samples, indicating a narrow size distribution. The WOW synthesis (P0.2-IgG-488 and its control P0.2-ctr) resulted in NPs having smaller size and higher pdI than samples obtained by OW process. This is possibly due to the fact that ultrasound energy was applied to the systems twice (Table 7).

Sample	**Z-ave (nm)**	**Peak (nm)**	**PdI**	**ζ-potential**
P0.2-OW-cur	594.4	604.8	0.127	-30.8
P0.2-OW-ctr	521.9	520.6	0.188	-30.6
P0.2-IgG-488	475.3	416.0	0.310	-27.0
P0.2-ctr	491.6	455.8	0.264	-24.3

Table 7. The size profile of the tested PLGA NPs obtained by DLS analysis.

Confocal microscopy characterization confirmed the presence of both the fluorophores (Fig. 23). In fact, fluorescence and transmitted light images showed co-localization, thus indicating that either curcumin or IgG1-488 were encapsulated into the PLGA NPs. On the contrary, no fluorescence was observed in the respective controls (P0.2-OW-ctr and P0.2-ctr).

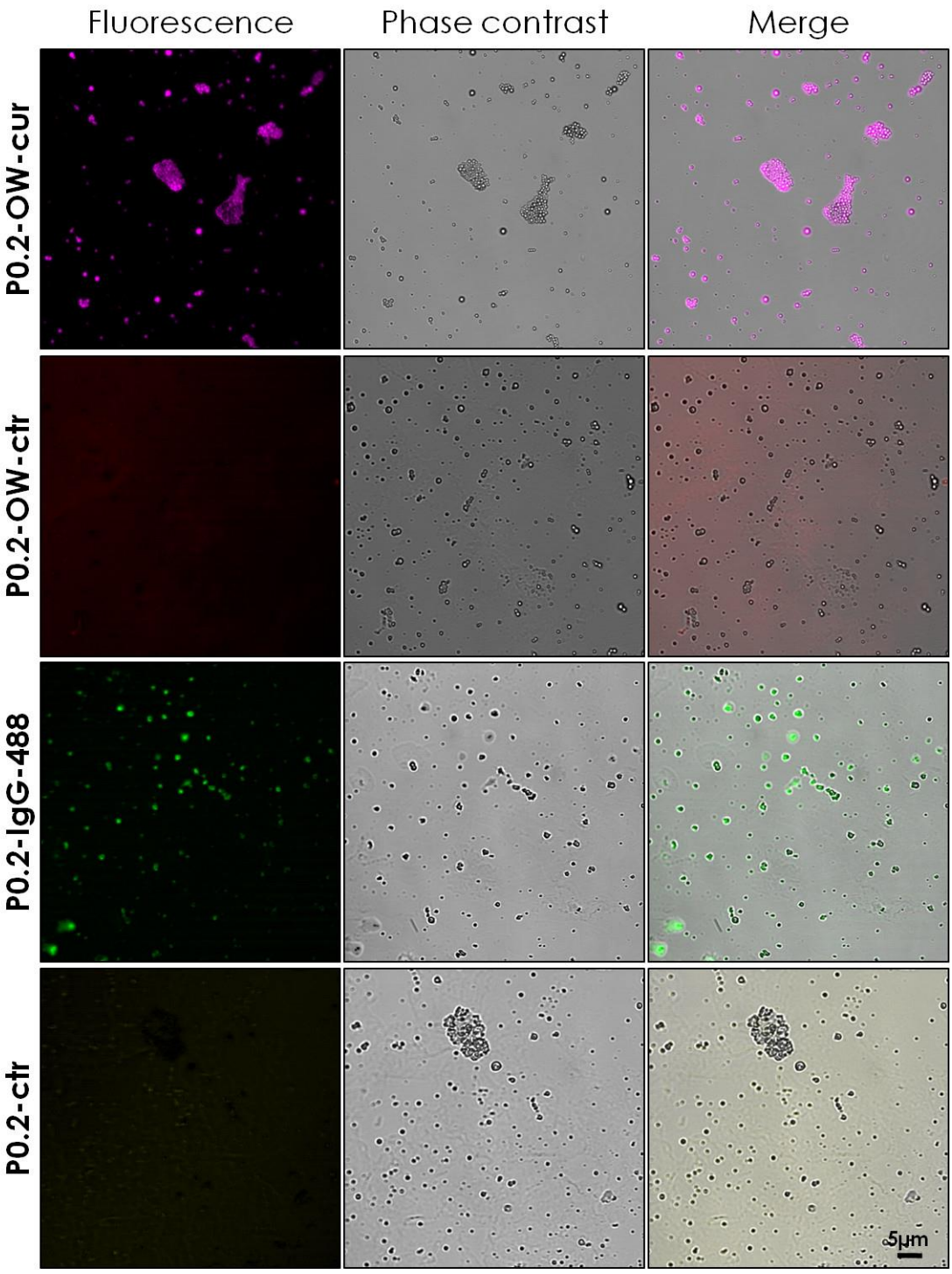

Fig. 23. Confocal microscopy characterization for P0.2-OW-cur, P0.2-OW-ctr, P0.2-IgG-488 and P0.2-ctr. Samples were stabilized with 0.2% w/v of PVA as surfactant. For P0.2-OW-cur and P0.2-IgG-488, fluorescent spots corresponding to curcumin and IgG-488, respectively, were found to co-localize with PLGA NPs observed in contrast phase images. No fluorescence was observed in their respective controls (P0.2-OW-ctr and P0.2-ctr)

In addition, samples morphology was assessed by Scanning Electron Microscopy (SEM) analysis. PLGA NPs was found to be round shape in all the tested samples, as shown in Fig. 24. SEM analysis additionally confirmed higher polydispersity of NPs obtained by WOW method with respect to solid (OW) NPs.

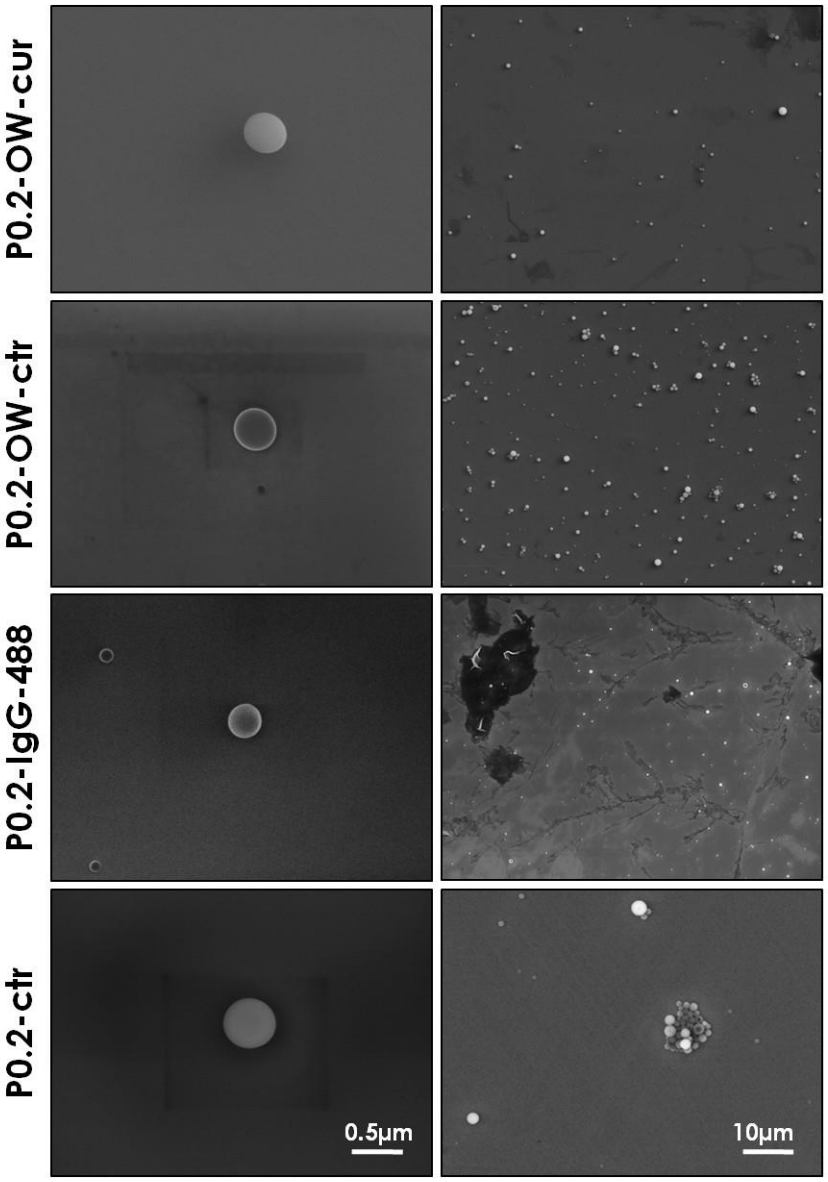

Fig. 24. Scanning Electron Microscopy (SEM) characterization for P0.2-OW-cur, P0.2-OW-ctr, P0.2-IgG-488 and P0.2-ctr. For each synthesis, two different magnifications were reported.

The dimensional distribution analysis on the acquired SEM images was performed using the Image J software. The size distribution (Fig. 25) was found to be slightly different to the one detected by

DLS, as expected because of the different parameter evaluated. In fact, DLS measures hydrodynamic diameter, while SEM analyses are performed on dry samples.

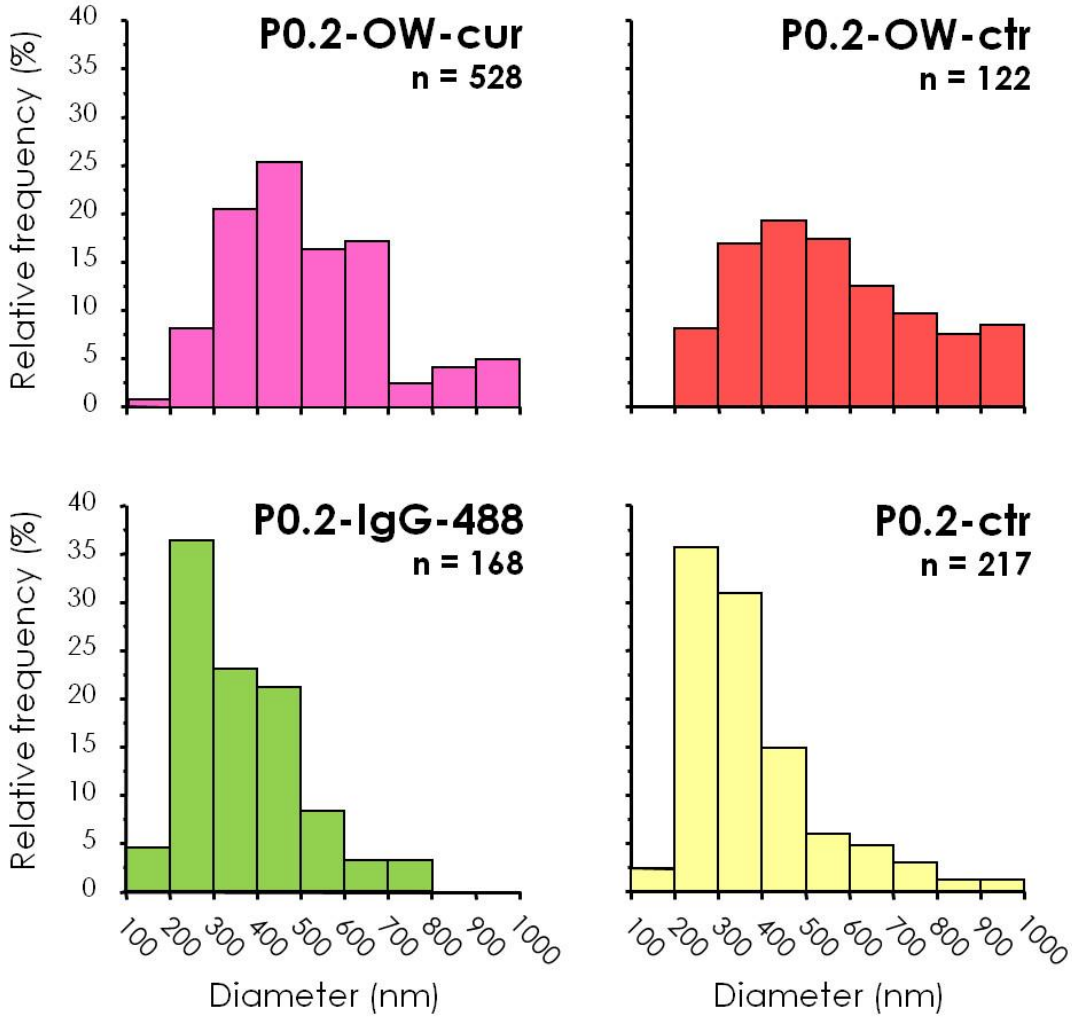

Fig. 25. Dimensional distributions as assess by SEM images. Relative frequency (%) was obtained with Origin software after particle analysis on the SEM images by means of the free available software Image J.

To investigate degradation properties, PLGA NPs were incubated in PBS, pH 7.4 at 37°C under mild rotation. Different conditions were tested, in particular PLGA NPs were freeze-dried with different amounts of either D-mannitol (1.0, 5.0, 10.0% w/v) or trehalose (1.0, 5.0, 10.0%) or a combination

of them (5.0% w/v D-mannitol and 5.0% w/v trehalose). As a control, PLGA NPs were also tested without lyophilization. Despite the variety of the tested conditions, no major differences were found in term of stability. Here the reported data are referred to samples freeze-dried with 1.0% w/v D-mannitol, being this condition representative of all the experimental set.

After 24 h of incubation, DLS measurements indicated degradation of all the tested samples (Fig. 26 and Table8), with particular evidence for core-shell NPs. This was assessed by the decrease in signal intensity, as express by DCR decline. In fact, during PLGA NPs degradation process a reduction of their relative refractive index occurred, thus reducing the total amount of the scattered light on which detection DLS analyses are based.

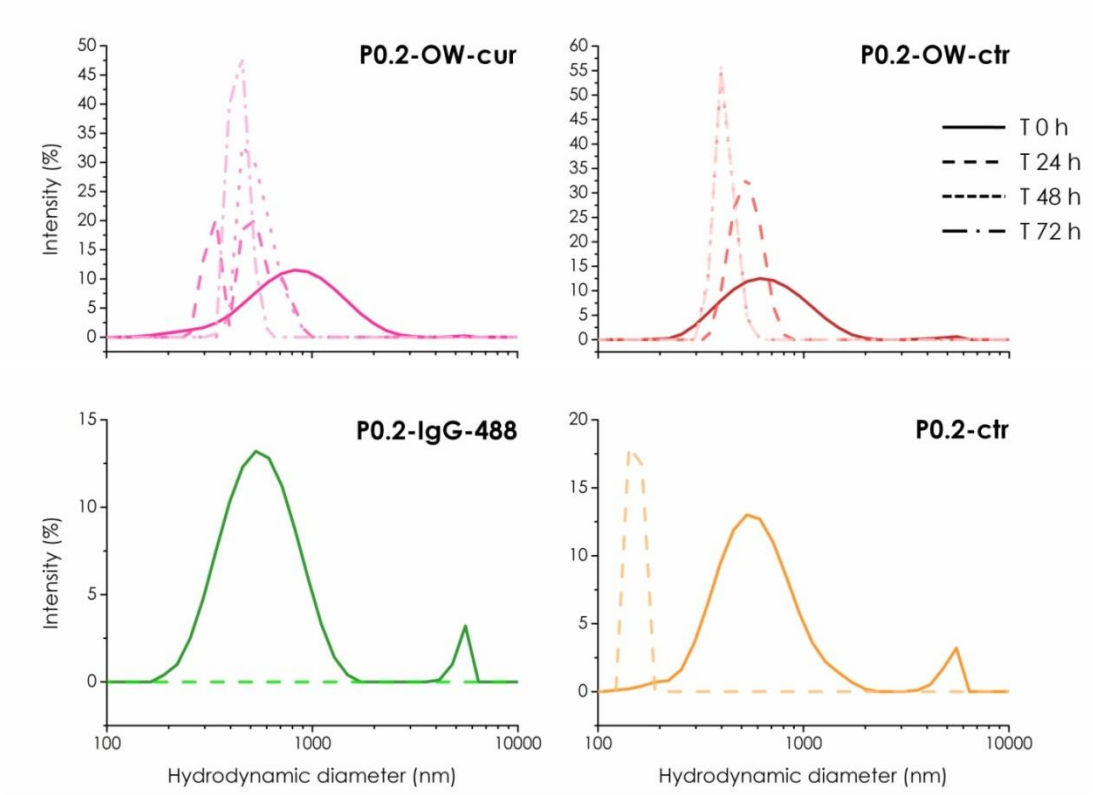

Fig. 26. DLS size distributions for P0.2-OW-cur, P0.2-OW-ctr, P0.2-IgG-488 and P0.2-ctr at different time points. In samples obtained by double emulsion (P0.2-IgG-488 and P0.2-ctr), degradation was complete after 24 hr, therefore time points 48 hr and 72 hr are not reported.

Sample	Time (h)	z-average (nm)	Peak (nm)	PdI	DCR (kcps)
P0.2-OW-ctr	0	599.1	705.8	0.196	1359.2
	24	749.3	529.7	0.408	201.6
	48	1440.0	413.6	0.949	165.8
	72	1240.0	413.7	0.893	218.4
P0.2-OW-cur	0	721.4	909.5	0.243	1062.2
	24	1478.0	571.1	0.780	162.3
	48	1309.0	548.1	0.766	185.6
	72	1228.0	442.5	0.825	179.1
P0.2-ctr	0	624.0	625.4	0.360	738.1
	24	2412.0	78.8	1.000	5.6
P0.2-IgG-488	0	708.0	588.8	0.524	313.8
	24	5560.0	0.0	0.864	3.4

Table8. Main parameters obtained from DLS analysis at different time points. In samples obtained by double emulsion (P0.2-IgG-488 and P0.2-ctr), degradation was complete after 24 hr, therefore time points 48 hr and 72 hr are not reported.

To overcome detection limit of DLS, an alternative approach based on SPES was used to characterize the NPs physical properties solution and their evolution during the degradation process. Details on how the SPES apparatus works can be found in paragraph 6.2 Single Particle Extinction and Scattering (SPES) page 60 of the Materials and methods section, as well as in literature[133–135].

SPES provided results in terms of particle size distribution (PSD) and refractive index distribution (RID). For the latter parameter, the average relative refractive index *m* is given.

PSD (Fig. 27) was found to be similar for all the tested samples. The mode values were 476 nm for P0.2-OW-ctr (panel A), 496 nm for P0.2-OW-cur (panel B), 456 nm for P0.2-ctr (panel C) and 456 nm for P0.2-IgG-488 (panel D), respectively.

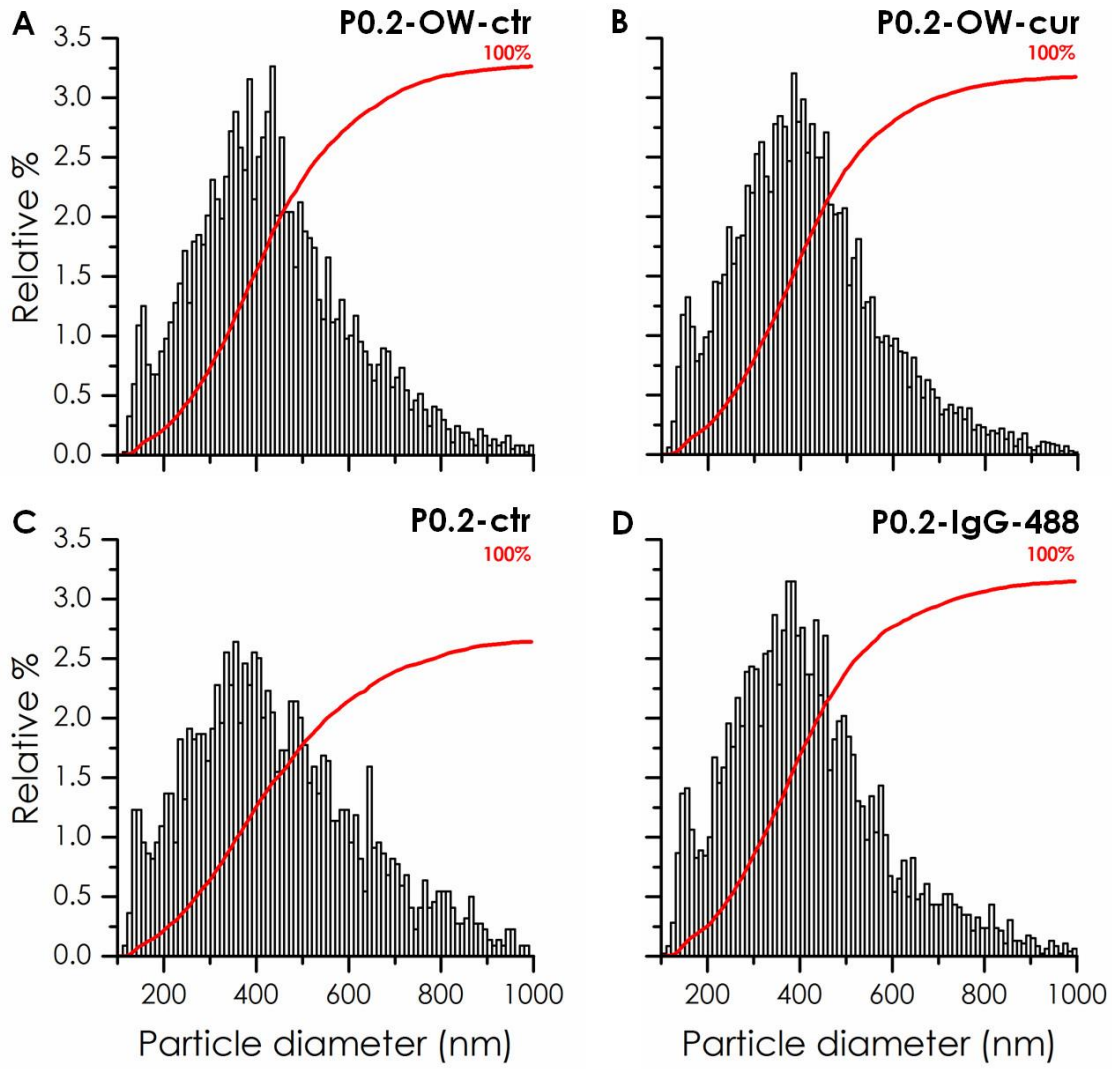

Fig. 27. SPES particle size distribution (PSD) for P0.2-OW-cur, P0.2-OW-ctr, P0.2-IgG-488 and P0.2-ctr. Red lines indicated cumulative distribution.

In a different way, some considerations can be done on the RID (Fig. 28). The red line, reported in all the graphs for comparison purpose, indicated the median value of the distribution for P0.2-OW-ctr, *m* = 1.105. In this sample (panel A), refractive index showed a symmetric distribution, with the exception of a negligible tail at the lowest values. Blue lines in panel B, C and D indicated

the RID median values, namely *m* = 1.12, *m* = 1.085 and *m* = 1.081, for P0.2-OW-cur, P0.2-ctr and P0.2-IgG-488, respectively.

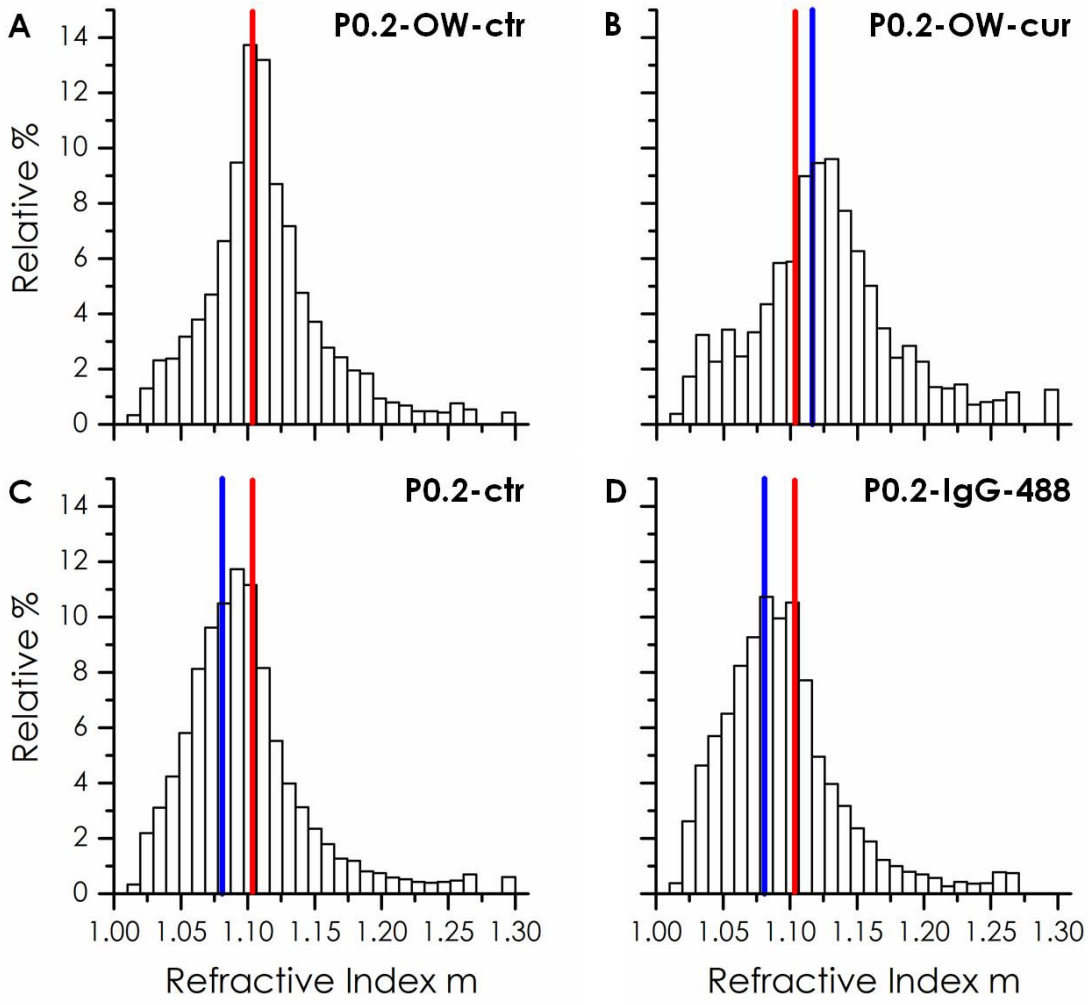

Fig. 28. SPES refractive index distribution (RID) for P0.2-OW-cur, P0.2-OW-ctr, P0.2-IgG-488 and P0.2-ctr. Red lines referred to *m* value for P0.2-OW-ctr, while blue lines indicated *m* for the corresponding sample.

As for P0.2-OW-ctr, also P0.2-OW-cur showed a symmetrical distribution for the refractive index values (panel B). Apparently, curcumin was encapsulated uniformly in all the PLGA NPs, as expected from an OW synthesis, in which the drug is homogeneously mixed with the polymer in the organic phase. Confocal analyses presented in Fig. 23additionally supported the results.

On the contrary, for sample P0.2-ctr (Fig. 28, panel C) RID was found to be shifted to small values. This was compatible with NPs core-shell structure. In fact, the presence of the aqueous inner core reduced the polarizability of the whole NPs, thus determining a reduction of the effective refractive index *m*. Noteworthy, for this sample a pronounced skewness was evident in the RID graph, indicating that the refractive index was spread over a more extended range, associable with the presence of drops with different size inside the NPs.

Samples undergoing degradation in PBS were analyzed to compare SPES and DLS results. Fig. 29 reported RID and PSD for P0.2-OW-ctr after incubation for 24 h. Similar considerations were done for all the other samples.

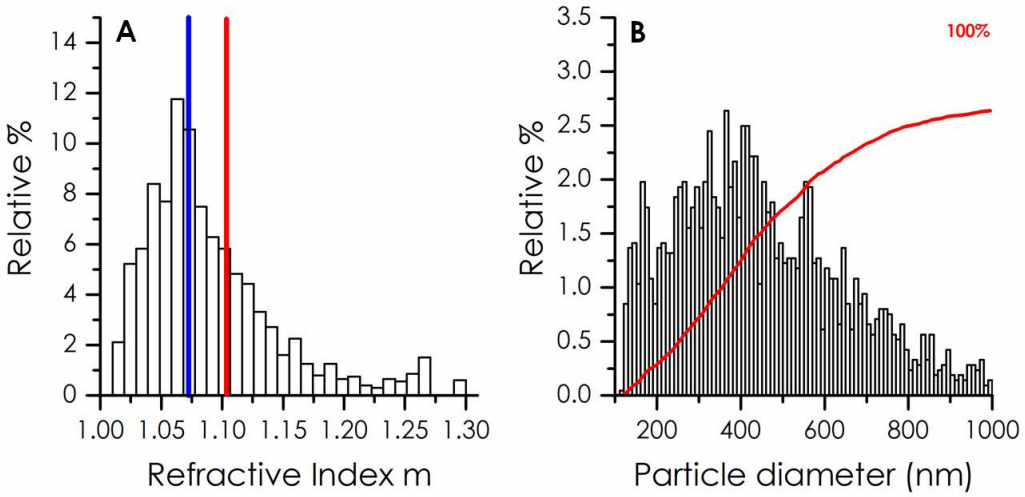

Fig. 29. SPES refractive index distribution (RID) and particle size distribution (PSD) for P0.2-OW-ctr after 24 h degradation. Results obtained for the degradation of P0.2-OW-ctr after 24 h incubation at 37°C with PBS.

Red line in panel A represented the average *m* as detected at time 0, while the blue line referred to the distribution detected after 24 h of the degradation study. As can be seen, *m* was appreciably smaller than that measured before incubation. Graphs also evidenced a skewed distribution, indicating the presence of NPs with different degree of compactness. Moreover, the PSD (panel B) showed an increase in NPs size, as indicated by the 515 nm mode value.

According to these results, the SPES method was found to have a good sensibility to the NPs changes after 24 h thanks to the peculiar forward scattering scheme adopted. During the degradation process, NPs were found to increase their size while reducing their refractive index. For DLS, both these conditions are responsible for the reduction of the scattered light and consequently detrimental on the instrumental performances. On the contrary, the peculiar forward scattering scheme on which the SPES apparatus is based is able to take advantages on the two phenomena and provide valuable results.

3. Amine-modified PVA as a novel surfactant to modulate size and surface charge of PLGA NPs

A major drawback relative to PVA employment in PLGA NPs synthesis is the final negative charge on the NPs surface. In particular, as reported in paragraph 1.6.2 PVA percentage page 75 in the Results and Discussion section, the ζ-potential values ranged from -24.6 to -31.0 mV for PVA synthesized samples. Such values are effective for colloidal stability, because they guarantee PLGA NPs repulsion. However, a negative surface charge prevents the nanoparticles from escaping the endosomes after cell internalization.

3.1 Synthesis and characterization of amino-PVA

By taking advantage of the PVA backbone, a new polymer (amino-PVA) was synthesized starting from two different monomers, vinyl acetate and DMAPMA. The first one, that is the monomer used for the synthesis of PVA, constituted the main chemical structure. By adding DMAPMA as monomer, tertiary amine groups were inserted in the surfactant as side groups. This provided the polymer with a positive charge (+19.5 mV), while avoiding the toxic potential of primary amines. Amino-PVA chemical structure can be seen in Fig. 30.

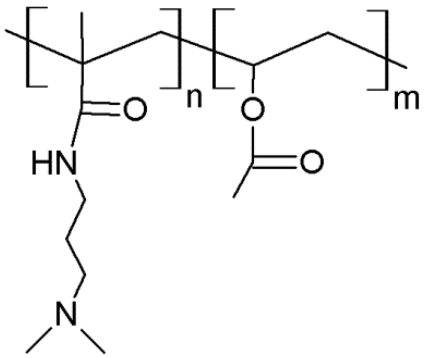

Fig. 30. Chemical structure of the new synthesized polymer, amino-PVA.

In order to assess molecular structure and monomer ratio in the final polymer, chemical characterization was performed by means of ^{1}HNMR and FT-IR spectroscopy (Fig. 31). FT-IR analysis (panel B) showed great similarity between the amino-PVA spectrum and the one of DMAPMA. On the contrary, ^{1}HNMR analysis was more informative. As could be seen in the reported spectrum (panel A), chemical groups peculiar for both the two single starting monomers were present. In particular, a vinyl acetate/DMAPMA molar ratio of 0.26 was calculated, based on peaks at 1.81 ppm and 2.28 ppm which were related to vinyl acetate and DMAPMA, respectively.

This indicated that both the monomer participated at the polymerization process and the product's chemical structure was in good accordance with the hypothesized one.

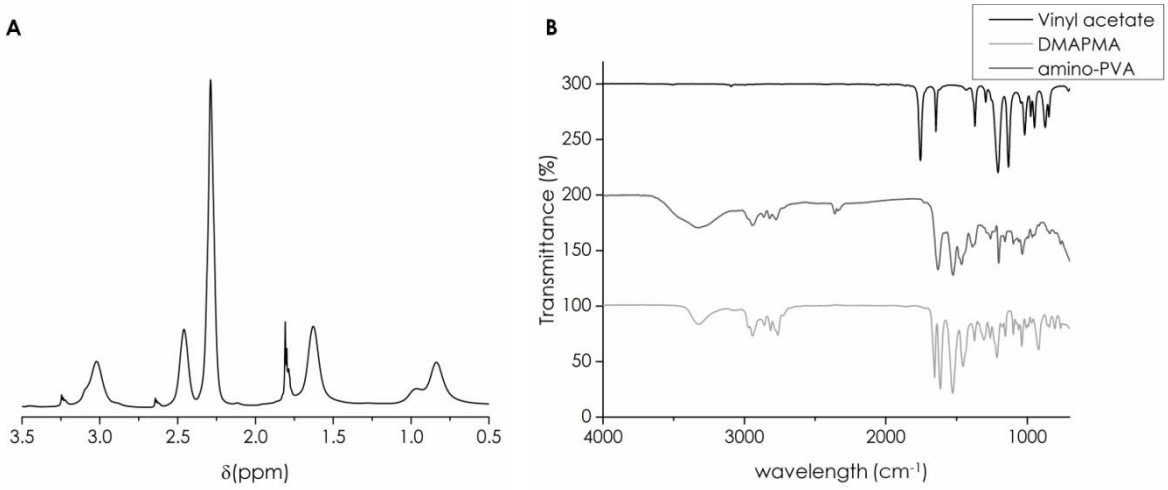

Fig. 31. ^{1}HNMR spectrum (panel A) and FT-IR spectra (panel B) of amino-PVA.

3.2 Synthesis of PLGA nanoparticles with amino-PVA

The potential of amino-PVA as a surfactant alternative to PVA was explored for PLGA NPs synthesis. Different surfactant concentrations were tested (from 1.0 to 5.0%), however micron sized particles were obtained. DLS analyses indicated very polydisperse population, in some cases with more than one NPs peaks. In addition, the surface charge was highly positive (+40.0 mV). This value is considered too high, because anion serum proteins can be strongly adsorbed onto NPs surfaces with consequent risk of opsonization and elimination from the organism.

An effective approach to obtain NPs with reduced size and positive charge consisted in using different combinations of PVA and amino-PVA. Notably, the PVA was found to reduce NPs diameter when used in combination with amino-PVA, although to a lesser extent with respect to PVA alone. In fact, as shown in Table 9, the more PVA was added, the smaller NPs were obtained.

	PVA/amino-PVA	Z-ave (nm)	Main peak (nm)	pdI	ζ-potential
9A	1/0	223.3	236.7	0.072	-29.9
9B	0.975/0.025	259.3	280.3	0.103	20.0
9C	0.95/0.05	314.9	336.2	0.048	38.1
9D	0.9/0.1	377.3	434.2	0.113	32.9
9E	0.7/0.3	552.9	646.8	0.144	45.3
9F	0/1	978.8	1225	0.180	39.4

Table 9. DLS size distribution and ζ-potential of PLGA NPs synthesized by mixing PVA and amino-PVA at different concentrations with OW synthesis. Control experiments were performed by using either PVA or amino-PVA alone.

While the PVA concentration was found to modulate the NPs size, the amino-PVA played an important role in determining the NPs surface properties. In particular, a very small quantity (0.025%) of amino-PVA was sufficient to provide the NPs surface with a mild positive charge (ζ-potential of +20.0 mV). In this way colloidal stability was guaranteed, while avoiding possible toxic effects due to a high positive charge.

3.2.1 Encapsulation of hydrophilic molecules: FITC, fib-647

Similar results in terms of size distribution and ζ-potential were obtained when WOW syntheses were performed. As can be seen in Table 10, NPs size was higher than using the OW procedure (sample 10A *vs.* sample 9A, sample 10C *vs.* sample 9B).

	PVA/amino-PVA	Inner core	Z-ave (nm)	Main peak (nm)	pdI	ζ-potential
10A	1/0	PBS 0.1X	292.2	314.9	0.130	-31.0
10B	1/0	FITC	271.5	314.2	0.126	-20.2
10C	0.975/0.025	PBS 0.1X	286.8	315.1	0.104	+20.1
10D	0.975/0.025	FITC	307.6	338.3	0.154	+19.2
10E	0.975/0.025	Fib-647	345.4	377.1	0.119	+27.0

Table 10. DLS size distribution and ζ-potential of PLGA NPs synthesized by mixing PVA and amino-PVA with WOW synthesis.

To demonstrate the suitability of the developed NPs for the release of hydrophilic drugs, FITC and fib-647 were encapsulated as model molecules. To note, the presence of FITC did not change substantially NPs features in terms of size distribution and polydispersity, as can be seen by comparing samples 10C and 10D with samples 10A and 10B, respectively. On the contrary, when fib-647 was encapsulated, larger NPs were obtained. This could be related to the higher MW of fib-647 if compared with the FITC molecule. In any case, sample 10E showed to be monodisperse and with an acceptable ζ-potential value.

3.2.2 Encapsulation of both hydrophilic and hydrophobic molecules: curcumin and fib-647

WOW synthesis was employed also for the development of a system carrying molecules for multiple drug release, namely fib-647 and curcumin. A-fib-cur was found to have size (z-average 294.3 nm) comparable to that of A-ctr and A-FITC (sample 10C and 10D, respectively). Monodispersity was very good (pdI 0.061), however a ζ-potential of +33.1 mV was found, thus indicating that curcumin influenced the amino-PVA arrangement on NPs surface.

3.3 Degradation studies

Further studies were performed on WOW samples because they represented the most appealing systems for the delivery of hydrophilic drugs. To assess PLGA NPs stability, the formulation obtained by WOW method with the surfactant mix PVA 0.975/amino-PVA 0.025% was selected (sample 10D). The sample 10C was studied as a control. Degradation was performed in PBS, at 37°C, under mild rotation. In these conditions PLGA NPs were found to be stable for at least ten days (Fig. 32). Even if the derived count rate decreased of around 80% in 48 hours, the size distribution of PLGA NPs was maintained, as well as their polydispersity and peak shape.

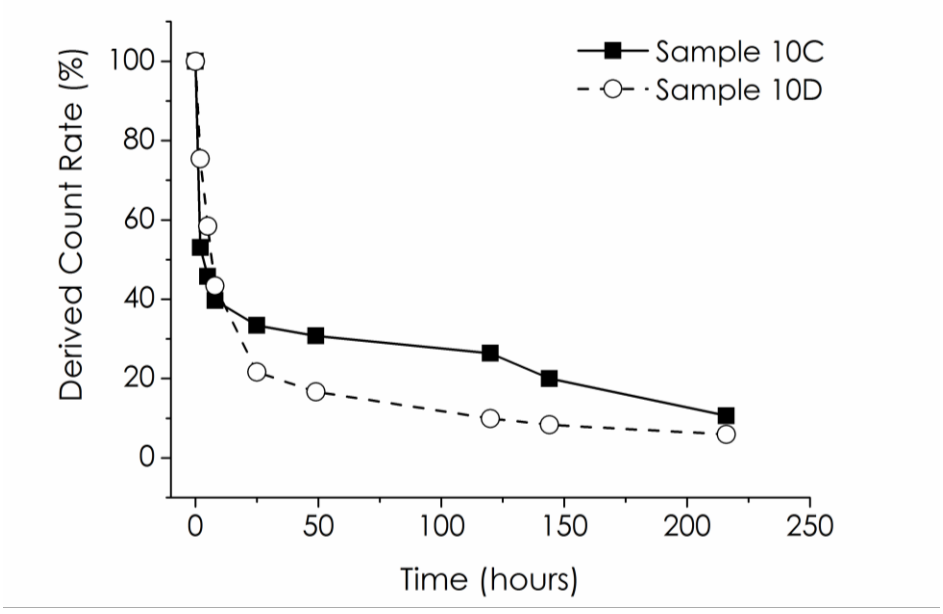

Fig. 32. Degradation profiles for amino-PVA stabilized PLGA NPs. The DLS measurements of WOW formulations with (sample 10D) or without (sample 10C) FITC - obtained with PVA 0.975% and amino-PVA 0.025%- were run over a period of 240 h.

4. Calcium Stearate as an effective alternative to PVA in PLGA nanoparticles synthesis

4.1 Single emulsion synthesis. Optimization of calcium stearate-stabilized PLGA nanoparticles.

PVA has been the favorite emulsifier in the synthesis of PLGA NPs because of its ability to form stable and uniformly distributed NPs[97,108,110–112]. Although amino-PVA was found to be effective in providing NPs with a positive charge, the amino-PVA stabilized NPs were still synthesized by means of 0.975% w/v PVA. Disadvantages in the use of this surfactant may be related to a partial evidence of toxicity and on the high amount of residual PVA that reduced NPs uptake capability[115]. Moreover, PVA is expensive and its employment influences the overall NPs cost.

Calcium stearate (CSt) is a low cost thermal stabilizer already present in innovative medical devices. Its capability to act as a surfactant in PLGA NPs synthesis has not been explored so far. In this dissertation, it was hypothesized that CSt hydrophilic heads can be exposed towards the aqueous environment, while the polar tails embedding in the PLGA matrix. Accordingly, the stabilizing effect of CSt on NPs synthesis has been thoroughly investigated. Notably, investigation on the single parameter influences on PLGA NPs synthesis has been firstly performed on OW synthesis. Being this emulsion method simpler than the double emulsion one, it allowed to assess in an easier way variations induced by each single parameter.

Preliminary synthesis gave evidence of CSt stabilizing effect that guarantees PLGA NPs formation. In fact, by adding CSt 20.0 mg/mL in the organic phase it was possible to obtain NPs with size 205.3 nm (z-average) and a good pdI (0.055) after solvent evaporation. However, this procedure was not suitable for PLGA NPs synthesis, because NPs pellet after centrifugation was impossible to recollect. Apparently, CSt hydrophilic heads did not prevent NPs from sticking one to each other during the purification process. In order to improve NPs stability, an additional couple of surfactants, namely Polysorbate 60 (P60) and Span 60® (S60), were added.

Sorbitan esters (Span®) and polyethoxylated sorbitan esters (Tween® or polysorbate) are two families of mild nonionic surfactants, having long-standing food and pharmaceutical approval,

thanks to their safe history of use. By using combination of Spans with their corresponding Tweens it is possible to prepare a variety of oil-in-water and water-in-oil emulsion systems. In fact, these surfactants present different characteristics in terms of hydrophobicity: polysorbates are hydrophilic while sorbitan esters show high hydrophobicity. Here, P60 and S60 were selected because part of their structure is in common with CSt, namely the stearic tail of the ester (Fig. 33).

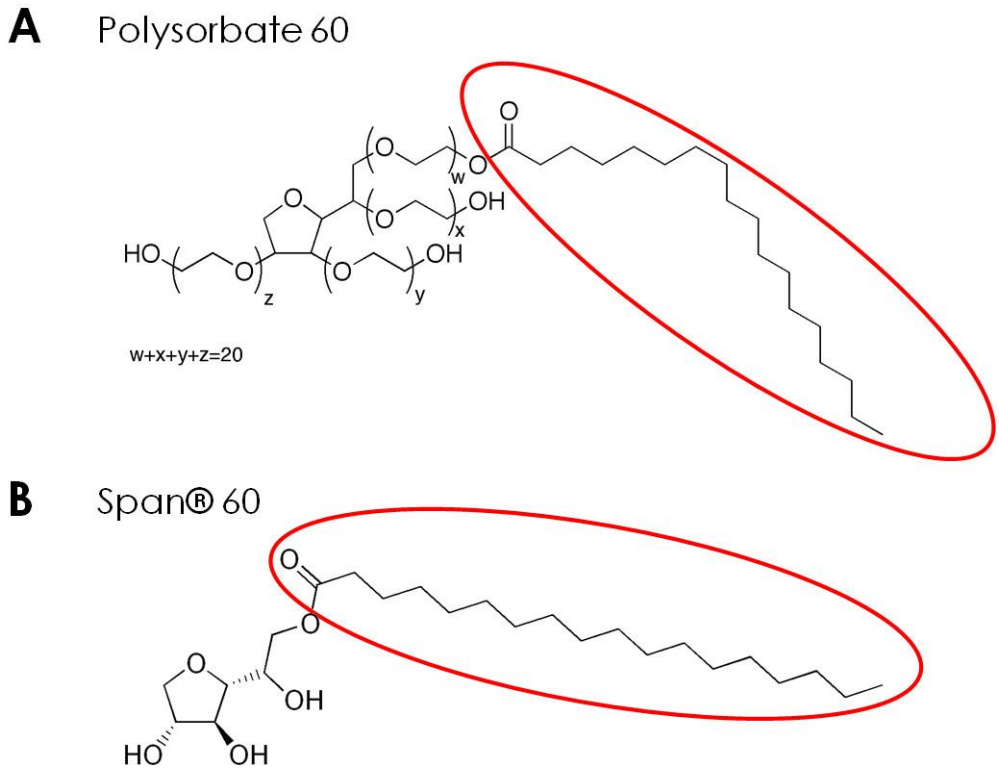

Fig. 33. Chemical structures of Polysorbate 60, P60 (panel A), and Span 60®, S60 (panel B). Red circles evidence the stearic portion of both molecules.

4.1.1 Effect of P60-S60 ratio

First, the P60-S60 optimal ratio was determined. In this regards, the S60 concentration was kept constant at 2.0 mg/mL while increasing the P60 concentration from 2.0 up to 5.0 mg/mL (Table 11). Accordingly, the P60 amount was lower (sample 11B), equal (sample 11C) or higher (sample 11D) than the S60 amount. In all cases, the PLGA NPs size was reduced and ζ-potential increased (resulted less negative) with respect to the synthesis with only CSt (sample 11A).

	S60 (mg/mL)	P60 (mg/mL)		z-average (nm)	Peak (nm)	pdI	ζ-potential (mV)
11A	0	0		295.9	323.0	0.120	-52.0
11B	2.0	2.0	P60<S60	207.3	221.4	0.091	NA
11C	2.0	3.2	P60=S60	242.4	254.4	0.043	NA
11D	2.0	5.0	P60>S60	205.3	216.8	0.055	-25.5

Table 11. PLGA NPs formulations using the P60-S60 couple at different molar ratios. NA, not available

Even if NPs obtained using S60 and P60 at the same molar ratio (sample 11C) showed a size slightly higher than the others two formulations (samples 11B and 11D), the pdI was the lowest and the NPs pellet after centrifugation was resuspended very easily. Therefore, the stoichiometric ratio between S60 and P60 was used in all the following experiments.

In order to minimize the quantity of additional surfactants in PLGA NPs synthesis, a progressive reduction of S60 and P60 concentration was tested. As can be seen in Table 12, PLGA NPs size reduced when S60-P60 quantities were increased, whereas no clear trend was observed by progressively reducing the S60-P60 amounts. Interestingly, the use of S60 and P60 at concentration lower than 1.0 mg/mL and 1.6 mg/mL, respectively (samples 12D, 12E, 12F, 12G), resulted in polydisperse NPs that were very hardly resuspended after centrifugation. Moreover, the DLS analysis of the tested samples 12E and 12F showed more than one peaks, indicating NPs aggregation.

For OW synthesis, S60 1.0 mg/mL and P60 1.6 mg/mL were selected as the best concentrations to employ, being the lowest possible that guaranteed NPs with acceptable size and monodispersity.

	S60 (mg/mL)	P60 (mg/mL)	z-average (nm)	Peak (nm)	pdI
12A	3.0	4.8	228.5	246.1	0.090
12B	2.0	3.2	242.4	254.4	0.043
12C	1.0	1.6	253.9	271.0	0.081
12D	0.75	1.2	343.5	312.6	0.307
12E	0.5	0.8	318.0	239.8+708.5	0.268
12F	0.4	0.6	310.4	237.7+837.8	0.393
12G	0.25	0.4	271.5	244.2	0.288

Table 12. PLGA NPs formulations using the P60-S60 couple at different concentrations. For all of these syntheses, CSt concentration was kept constant at 20.0 mg/mL.

4.1.2 Effect of calcium stearate concentration

After having optimized the P60-S60 ratio in the PLGA NPs synthesis, the CSt role as stabilizer was thoroughly investigated (Table 13). When no CSt was added (sample 13A), samples presented multiple peaks and polydispersity higher than all the other samples. Interestingly, by increasing the CSt concentration from 5.0 to 40.0 mg/mL (samples from 13B to 13F) the NPs size was found to be reduced up to about 290 nm. However, differences were not indicative.

	CSt (mg/mL)	z-average (nm)	Peak (nm)	pdI	Degradation (days)
13A	0	494.8	521.9+5213	0.396	-
13B	5.0	322.5	348.0	0.133	<1 day
13C	10.0	309.9	336.9	0.098	8
13D	20.0	309.7	325.3	0.146	3
13E	30.0	307.0	318.8	0.177	3
13F	40.0	288.2	307.7	0.139	<1

Table 13. PLGA NPs formulations using CSt at different concentrations. For all of these syntheses, P60 and S60 concentrations were kept constant at 1.6 and 1.0 mg/mL, respectively.

Preliminary studies on NPs degradation indicated that PLGA NPs synthesized with CSt 10.0 mg/mL were stable up to eight days in physiological mimicking conditions, while for all the other tested concentrations NPs degraded in less than three days. Apparently, too high concentration of CSt weakens PLGA structure and can interfere with the overall NPs arrangement. On the contrary, low CSt quantity was not sufficient to guarantee NPs resistance during time. Consequently, CSt 10.0 mg/mL was used in all the following experiments.

4.1.3 Encapsulation of hydrophobic molecule: curcumin

PLGA NPs encapsulating curcumin were synthesized and the best curcumin quantity was evaluated. As can be seen from Table 14, curcumin has a role in stabilizing NPs size and size distribution. In fact, when the lowest amount of curcumin was added (2.5 mg/mL, sample 14B), NPs showed a sharp increase in diameter and polydispersity. Similar results were observed using curcumin at the concentration of 10.0 mg/mL (sample 14D). In this case, the presence of aggregates was also detected. Differently, when curcumin was added the tenth with respect to the PLGA polymer (sample 14C), NPs with size comparable to the corresponding sample without encapsulated drug (sample 13C) were obtained. This is in accordance to previous findings in the

literature[129–131]. Consequently, 5.0 mg/mL was selected as optimal drug concentration in the PLGA NPs synthesis.

	Curcumin (mg/mL)	z-average (nm)	Peak (nm)	pdI
14A	0	306.6	327.3	0.127
14B	2.5	408.2	438.6	0.219
14C	5.0	300.2	313.4	0.151
14D	10.0	383.1	386.0+5349	0.343

Table 14. PLGA NPs formulations using curcumin at different concentrations.

Actual encapsulation of the drug in sample 14C was assessed by confocal microscopy. As shown in Fig. 34, colocalization was found between fluorescence signal of curcumin and NPs contrast phase image.

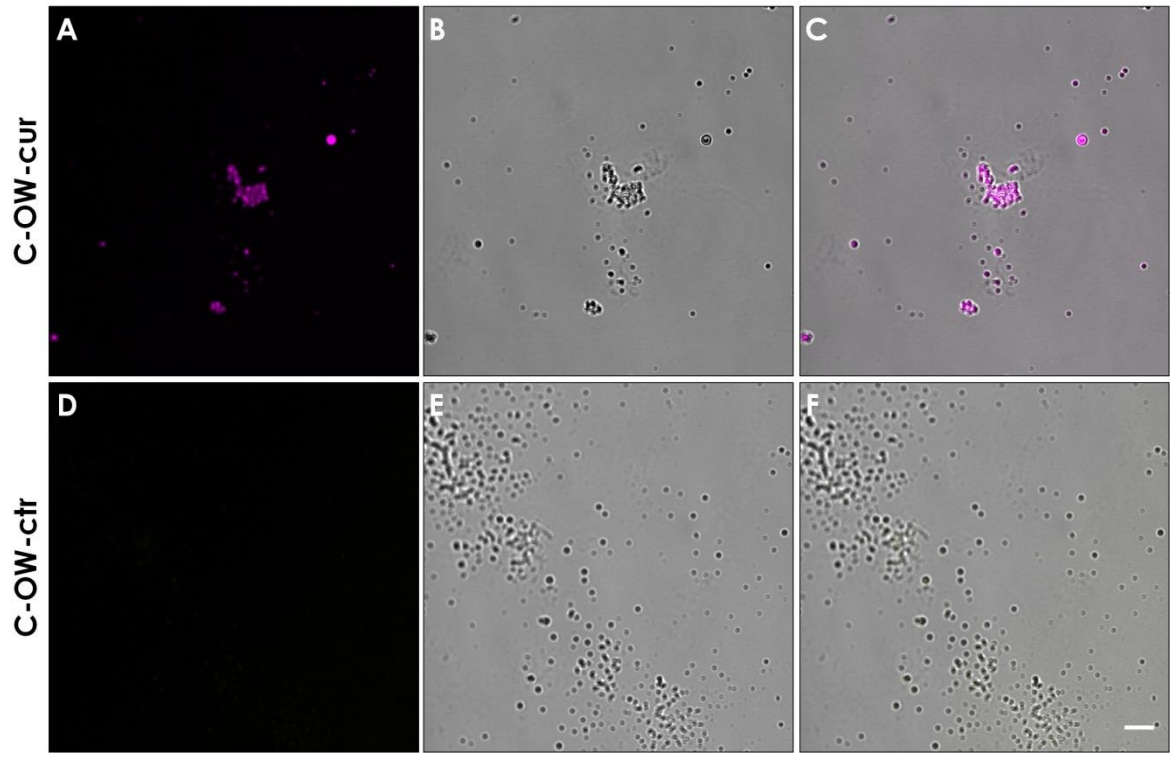

Fig. 34. Confocal characterization of C-OW-cur (panel A, B, C) and its control C-OW-ctr (panel D, E, F). Fluorescence detected in panel A was found to colocalized (panel C) with contrast phase

image (panel B). This was not the case for the control sample (panel D fluorescence channel, panel E contrast phase, panel F merge). Scale bar is 5 μm.

The encapsulation of curcumin into the PLGA NPs (sample 14C) was further investigated by stimulated emission depletion (STED) microscopy, that is characterized by better resolution with respect to confocal microscopy and has shown to be a useful tool in detecting nano-sized systems[132]. Considering the STED image (Fig. 35), two main points can be raised. The NPs spots were less bright than in confocal microscopy images, as expected due to the high power of the laser that resulted in partial fluorophore bleaching. Conversely, STED provided a higher resolution and the homogeneous distribution of curcumin within the NPs was observed.

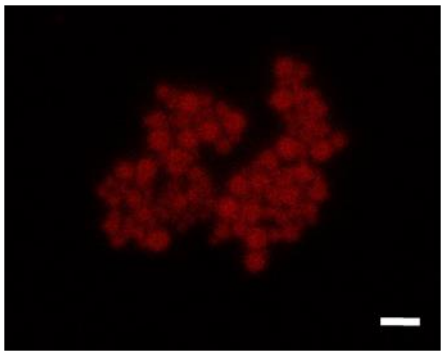

Fig. 35. STED microscopy image of curcumin loaded CSt stabilized PLGA NPs. The scale bar is 1 μm.

4.2 Double emulsion synthesis. Parameter investigation

Similarly to OW synthesis, a systematic analysis was also performed on WOW synthesis. In particular, attention was focused on the surfactants concentration.

Table 15 reported the size and ζ-potential of PLGA NPs synthesized by WOW method. The CSt concentration was fixed at 10.0 mg/mL, whereas the concentration of S60 and P60 was increased while keeping constant their ratio. As in the case of OW synthesis, the P60-S60 surfactants couple

was necessary for reducing NPs size and polydispersity (compare sample 15A *vs*. other samples). When increasing the amount of P60 and S60, NPs size decreased. However, by increasing P60-S60 concentrations from 2.0-3.2 mg/mL to 3.0-4.8 mg/mL only a 10-nm reduction in NPs size was observed (sample 15C *vs.* sample 15D).

Notably, the increase of S60 and P60 concentrations from 1.0-1.6 mg/ml to 2.0-3.2 mg/mL allowed to considerably reduce the NPs size (from 293.9 to 250.9 nm) and improve the NPs stability (ζ-potential was more negative, from -21.7 to -25.5 mV). Therefore, formulation 15C was additionally investigated.

	S60 (mg/mL)	**P60 (mg/mL)**	**z-average (nm)**	**Peak (nm)**	**pdI**	**ζ-potential (mV)**
15A	0	0	409.6	394.9+1971	0.235	-19.6
15B	1.0	1.6	293.9	322.5	0.114	-21.7
15C	2.0	3.2	250.9	270.9	0.074	-25.5
15D	3.0	4.8	243.5	261.8	0.108	-28.9

Table 15. PLGA NPs formulations using P60 and S60 at different concentrations in WOW synthesis. For all of these syntheses, CSt concentration was kept constant at 10.0 mg/mL.

In WOW synthesis, the role of CSt was found to be similar as in OW synthesis (Table 16), being the CSt able to reduce NPs size (samples 16A *vs.* other samples). As a control, NPs were synthesized without CSt and with P60-S60 at the concentration of 1.6-1.0 mg/mL respectively. The obtained NPs were smaller (z-average 469.7 nm, main peak 468.5 nm) than the corresponding ones obtained by OW synthesis (sample 13A), as expected because ultrasounds were applied twice. No main differences were found by adding 10.0, 20.0 or 30.0 mg/mL of CSt in terms of size,

polydispersity and ζ-potential, therefore 10.0 mg/mL CSt was maintained as the optimal amount in all the following syntheses.

	CSt (mg/mL)	z-average (nm)	Peak (nm)	pdI	ζ-potential (mV)
16A	0	303.1	323.5	0.065	-32.6
16B	10.0	250.9	270.9	0.074	-25.5
16C	20.0	266.4	283.8	0.127	-24.6
16D	30.0	256.7	274.6	0.092	-22.9

Table 16. PLGA NPs formulations using CSt at different concentrations. For all of these syntheses, P60 and S60 concentrations were kept constant at 3.2 and 2.0 mg/mL, respectively.

4.2.1 Encapsulation of hydrophilic molecules: fib-647, FITC

In the case of WOW synthesis, fibrinogen-labeled with Alexa 647® (fib-647) (C-fib) was selected as hydrophilic model molecule. C-fib showed higher size (z-average 282.7 nm) than the corresponding control without adding fib-647 (sample 16B, z-average 250.9 nm). Both the samples presented very good monodispersity, with a pdI less than 0.09. This suggested that fib-647 was effectively encapsulated in CSt stabilized PLGA NPs.

Further evidence of the actual fib-647 encapsulation was provided by confocal characterization (Fig. 36).

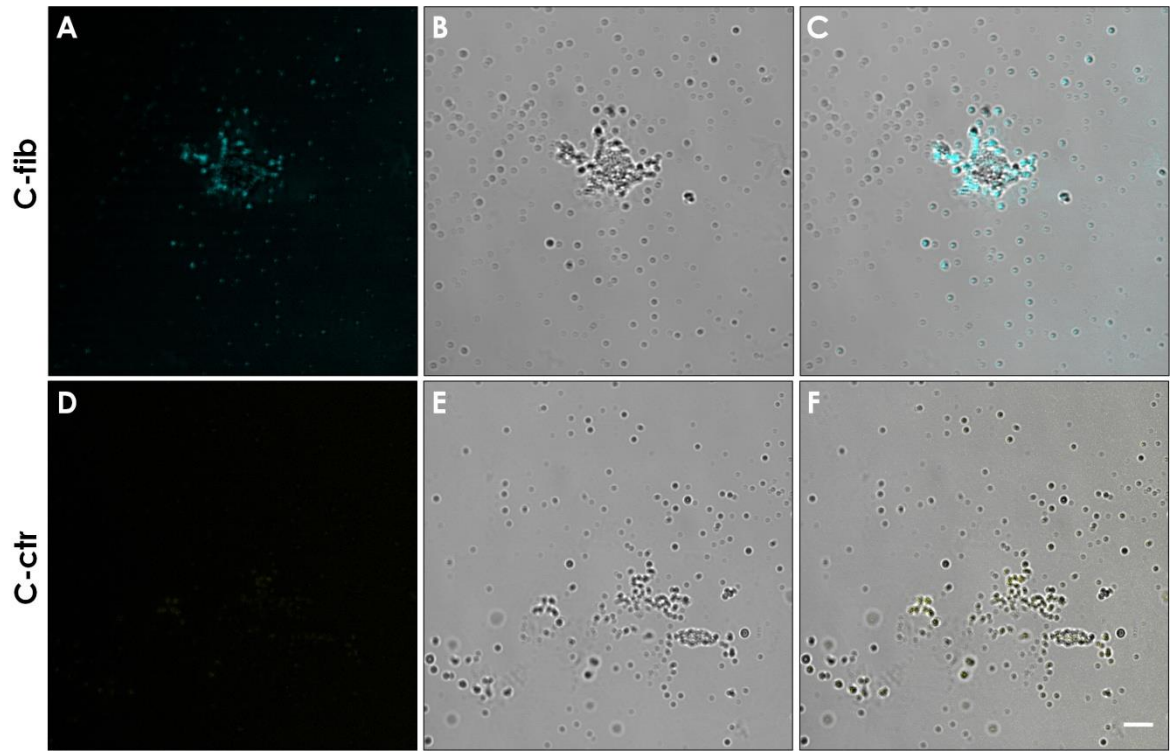

Fig. 36. Confocal characterization of C-fib (panel A, B, C) and its control C-ctr (panel D, E, F). Fluorescence detected in panel A was found to colocalized (panel C) with contrast phase image (panel B). This was not the case for the control sample (panel D fluorescence channel, panel E contrast phase, panel F merge). Scale bar is 5 µm.

In addition, FITC was selected as hydrophilic molecule with low MW and encapsulated during the WOW synthesis. Notably, C-FITC size (z-average 311.8 nm) was higher than C-fib. Apparently, the proteic nature of fibrinogen acted as an additional stabilizer for the double emulsion that resulted in lower particles.

4.2.2 Encapsulation of both hydrophilic and hydrophobic molecules: curcumin and fib-647

In addition, a system encapsulating both curcumin and fib-647 was explored (C-fib-cur) as multiple drug release system. Controls experiments were performed to investigate the influence of either curcumin or fib-647 in determining the overall NPs feature. In particular, NPs were synthesized by WOW encapsulating either curcumin in the polymeric shell (C-cur) or fib-647 in the

aqueous inner core (C-fib, see 4.2.1 Encapsulation of hydrophilic molecules: fib-647, FITC page 105 in the Results and discussion section).

C-fib-cur showed higher size (z-average 292.1 nm) and polydispersity (pdI 0.207) than the corresponding core-shell NPs without curcumin (C-fib). This was expected because of the addition of curcumin in the NPs formulation. Differently, C-fib-cur showed size comparable to that determined for C-cur (z-average 297.4 nm); therefore, these data did not provide clear indication on the effective fib-647 encapsulation.

However, the confocal microscopy analysis (Fig. 37) allowed to evidence that both fib-647 and curcumin were simultaneously incorporated in the CSt stabilized PLGA NPs.

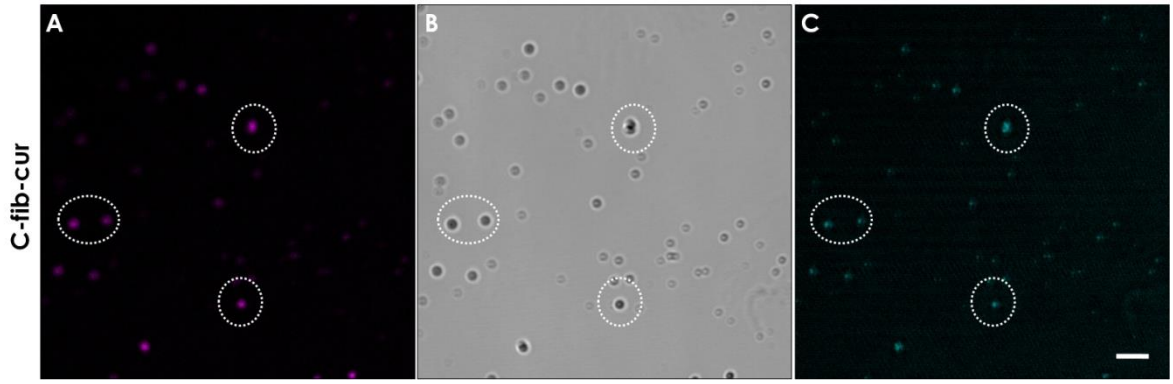

Fig. 37. Confocal characterization of C-fib-cur. Fluorescence was detected for both curcumin (panel A) and fib-647 (panel C) fluorescence channel. To note, the fluorescent spots co-localized between them and the contrast phase (panel B) image (circles). Scale bar is 5 µm.

4.3 Morphology study. SEM

To complete the NPs morphological characterization, SEM analyses was performed. As can be seen in Fig. 38, NPs was round shape and with a narrow polydispersity.

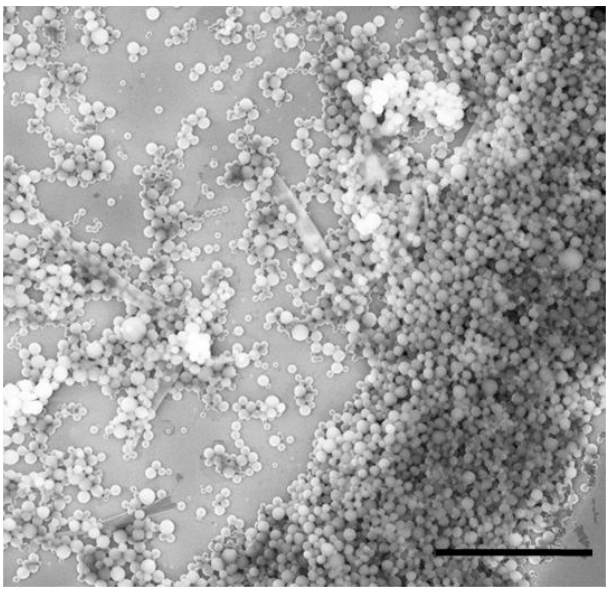

Fig. 38. Scanning Electron Microscopy characterization of C-OW-cur. CSt stabilized NPs were found to be round shape and monodisperse. Scale bar is 5µm.

4.4 Degradation study

The degradation study of CSt stabilized PLGA NPs was performed on the samples reported in Table 17. For comparison purpose, all the syntheses (included the OW ones) were run with CSt 10.0 mg/mL and S60-P60 2.0-3.2 mg/mL. Curcumin was encapsulated as hydrophobic drug in PLGA NPs obtained by both OW (C-OW-cur) and WOW (C-cur) syntheses, while in the aqueous core of core-shell NPs the fib-647 was encapsulated (C-fib). For multiple drug release purpose, PLGA NPs containing both the drugs (C-fib-cur) was investigated. Controls samples for both OW (C-OW-ctr) and WOW (C-ctr) without model molecules were additionally considered. Noteworthy, DLS data reported in Table 17 referred to the means of four different replicates and showed very good reproducibility in terms of both size and size distribution.

	z-average (nm)	pdI
C-OW-ctr	293.1 ± 29.7	0.157 ± 0.071
C-OW-cur	326.1 ± 32.6	0.210 ± 0.045
C-ctr	256.8 ± 15.6	0.083 ± 0.008
C-cur	296.8 ± 28.2	0.208 ± 0.033
C-fib	280.8 ± 13.9	0.118 ± 0.034
C-fib-cur	295.8 ± 8.7	0.206 ± 0.031

Table 17. DLS characterization of CSt stabilized NPs synthesized by OW and WOW methods. DLS data are expressed as mean ± standard deviation (n = 4).

When performing degradation study, it was found that curcumin reduced the PLGA NPs stability. In fact, C-OW-cur, C-cur and C-fib-cur showed a rapid decrease in count rate and were found to be completely degraded in about nine days. On the other hand, samples without curcumin (C-OW-ctr, C-ctr, C-fib) had constant DCR values until day 4. Then the number of detected photons showed a sharp drop, and finally the DCR decreased slowly until complete degradation, that occurred at day 28 (Fig. 39, panel A).

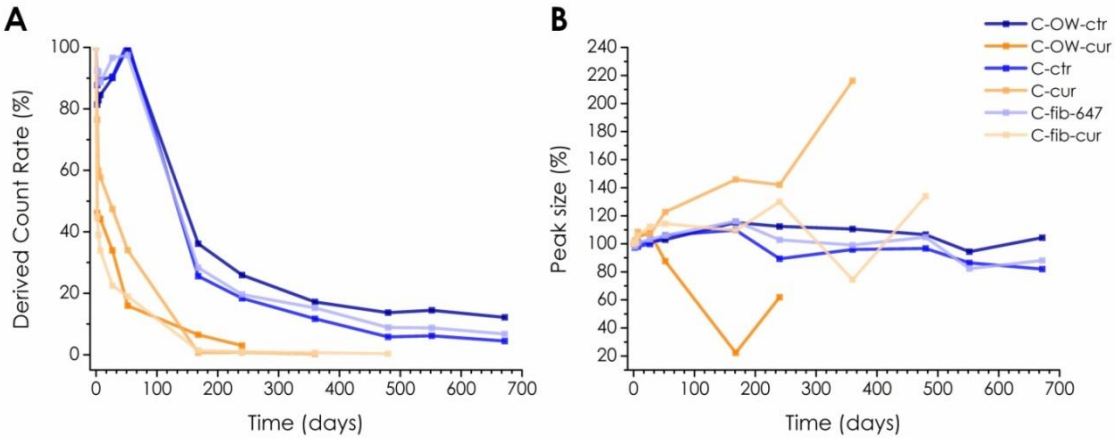

Fig. 39. Degradation studies on CSt PLGA NPs. Panel A reported Derived Count Rate trend, while Panel B referred to peaks size percentage values during time.

Evidently, it was found that the degradation process followed different mechanisms in the presence or absence of curcumin. This was even more clear considering the NPs size (Fig. 39, panel B). In fact, in samples C-OW-ctr, C-ctr and C-fib NPs size was found to be stable during time. On the other hand, for samples encapsulating curcumin, trends were different but in all cases the NPs peak size increased before complete degradation. This behavior is compatible with a release of the drug followed by the NPs matrix swelling. To note, this behavior was accentuated for C-OW-cur, for which it is possible to hypothesize that a higher amount of drug was encapsulated.

4.5 Release study

By taking advantage of the optical properties of the selected model molecules, namely curcumin and fib-647, release studies by the dissolution technique[136] were performed using spectrofluorimetry. Quantification was possible thanks to the calibration curves presented in the Materials and methods section, paragraph 7.1 Calibration curve for curcumin page 63 and 7.2 Calibration curve for fib-647 page 64.

For NPs encapsulating curcumin, a clear trend was found (Fig. 40, panel A). The most majority of the drug was released after 24 h of incubation, but the release was sustained up to day 15, especially for C-OW-cur. Surprisingly, C-cur showed a higher release with respect to C-fib-cur. Apparently, the simultaneous presence of both molecules interfered with the curcumin release.

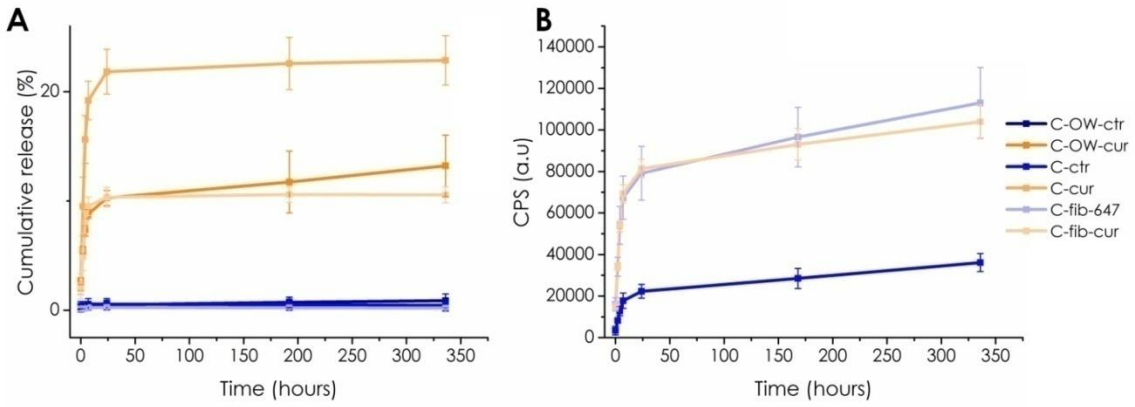

Fig. 40. Cumulative release of curcumin (panel A) and fib (panel B) as assessed by spectrofluorometer.

Unfortunately, the quantification of fib-647 was not possible because of technical issues in assessing the content of encapsulated drug. Accordingly, only a cumulative release as assessed by the relative percentage of collected photon was provided. As can be seen in Fig. 40 (panel B), also in the case of fib-647 a fast release was observed in the first 24 h, followed by a sustained release during the following 15 days for both C-fib and C-fib-cur.

5. D-Mannose and protein corona decorations

5.1 DLS characterization

After having optimized experimental parameters in the synthesis of either amino-PVA or CSt stabilized PLGA NPs, further surface functionalization was investigated for specific TAMs targeting. To this aim, mannose was selected to decorate NPs surface because of the overexpression of the mannose receptor CD206 on TAMs external membrane.

Although a variety of surface functionalization strategies have been developed to provide NPs with specific targeting, recognition properties of these systems are poorly evident *in vitro*[146]. This is mainly due to serum-proteins interactions with the NPs, which could highly affect their fate. Indeed, proteins can physically cover active targeting moieties on the NPs surface or interfere with their specific functions, thus the biological outcomes of NPs can be significantly altered with respect to predicted activity.

In this dissertation, it was hypothesized that the interactions between serum proteins and NPs surface can be exploited as a strategy to prevent the inactivation of NPs targeting moieties.

More specifically, PLGA NPs were incubated in a mixture consisting of 10.0% v/v FBS and 20.0% w/v D-mannose (FBSM). For comparison, also different conditions were tested, namely 10.0% v/v FBS without mannose (FBS), 100% FBS with (100FBSM) and without (100FBS) 20.0% w/v mannose. DLS analyses for size and ζ-potential were performed to evaluate the formation of the NPs protein corona and its effect on the NPs surface properties.

Samples selected for this experimental set included C-fib and C-fib-cur, as well as A-OW-ctr, A-ctr, A-fib and A-fib-cur.

As can be seen in Table 18, in all tested samples the addition of D-mannose in the incubating mixture led to an increase in size (FBSM *vs.* FBS and 100FBSM *vs.* 100FBS), with the exception of C-fib. This can be referred to the actual adsorption of D-mannose on NPs surface.

Notably, for CSt stabilized PLGA NPs the increase in size was also dependent on the protein amount, having samples incubated with 100FBS a higher size than those incubated with FBS. Differently the amino-PVA stabilized NPsdid not change their diameters after incubation with 100FBS but increased up to 138% (A-fib) after incubation with FBS.

Finally, A-ctr did not show substantial variation in size in all the incubation conditions, suggesting that this sample had more stealth properties than the other ones.

Sample	FBSM	FBS	100FBSM	100FBS
C-fib	125.9%	150.7%	253.9%	239.2%
C-fib-cur	148.7%	109.9%	238.2%	188.9%
A-OW-ctr	164.7%	125.2%	194.6%	99.3%
A-ctr	97.0%	93.3%	97.4%	83.5%
A-fib	169.7%	138.4%	162.0%	96.5%
A-fib-cur	184.5%	130.6%	133.8%	96.7%

Table 18. Percentage of increase in PLGA NPs size after incubation with different media (FBSM, FBS, 100FBSM, 100FBS).

Of particular interest were the ζ-potential analyses (Table 19). C-fib did not showed differences in the surface charge values before and after incubation with FBS, at all the tested conditions. In a different way, the FBS concentration affected the overall surface charge of C-fib-cur sample, being ζ-potential more negative using 100FBSM and 100FBS. Considering the amino-PVA stabilized NPs, the positive ζ-potential measured at time 0 became negative for all the incubation conditions. Apparently the cationic surface of the NPs attracted anionic proteins that converted their surface charge, even if NPs size was not substantially affected as in the case of A-ctr. To note, in both CSt and amino-PVA stabilized NPs, D-mannose addition did not substantially change the NPs surface charge, as expected being this molecule without net charge (see chemical structure in Fig.10).

Sample	Time 0	FBSM	FBS	100FBSM	100FBS
C-fib	-26.9	-25.8	-28.4	-25.1	-24.0
C-fib-cur	-24.9	-25.0	-24.8	-32.2	-37.2
A-OW-ctr	+23.6	-22.4	-24.0	-18.7	-22.8
A-ctr	+36.2	-25.6	-26.5	-20.6	-20.0
A-fib	+24.3	-23.5	-23.7	-24.6	-19.9
A-fib-cur	+24.3	-22.4	-23.4	-22.8	-15.4

Table 19. ζ-potential (mV) values after incubation with FBS, FBSM, 100FBS and 100FBSM.

5.2 XPS characterization

An additional analysis with X-ray photoemission spectroscopy (XPS) was performed on a representative sample (A-ctr). In particular, this technique was selected to understand if D-mannose was effectively adsorbed on the NPs surface. To avoid any interference during analysis from proteins component, A-ctr was incubated with 20.0% w/v D-mannose without FBS and carbonium profiles before and after incubation are reported in Fig. 41. In sample treated with D-mannose, NPs surface presented an increased percentage of -C-OH bond. This leaded to a different response in XPS analysis.

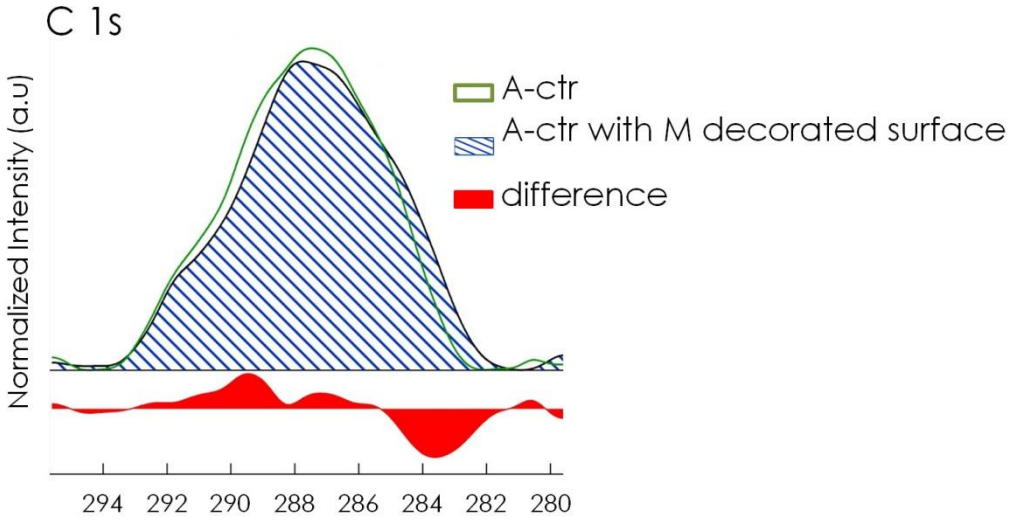

Fig. 41. XPS analysis of NPs after incubation with 20.0% w/v D-mannose.

6. Cytotoxicity studies

The cytocompatibility of the PLGA NPs was assessed by MTT test. Particular focus was done on either CSt or amino-PVAstabilized PLGA NPs encapsulating the hydrophilic model molecule FITC. Accordingly, C-FITC and A-FITC were synthesized by WOW method in sterile conditions, as well as their respective controls without FITC, C-ctr and A-ctr. To evaluate the effect on cytocompatibility of the NPs components as well as the surface decoration for specific TAMs targeting, different conditions were selected. In particular, each sample underwent 24 h incubation in 20% w/v D-mannose (M), or 10% v/v FBS (FBS),or 10% v/v FBS and 20% w/v D-mannose (FBSM). Moreover, non treated NPs were used at two different dilutions, namely 1 to 100 (C-FITC, C-ctr, A-FITC, A-ctr) and 1 to 10 (C-FITC 2, C-ctr 2, A-FITC 2, A-ctr 2) in PBS 1X.

In RAW264.7 culture, CSt stabilized NPs (C-FITC and C-ctr) showed very good cytocompatibility (Fig. 42). Cell viability was higher than 90% for all the tested conditions and no differences were found even at high NPs concentration (C-FITC 2 and C-ctr 2). Surface modification by adsorption of

D-mannose or proteins was found to be as safe as unmodified NPs. Apparently, slightly reduction in cell viability had to be ascribed to the NPs components rather than their surface functionalization. To note, the experimental reliability was confirmed by both positive and negative controls.

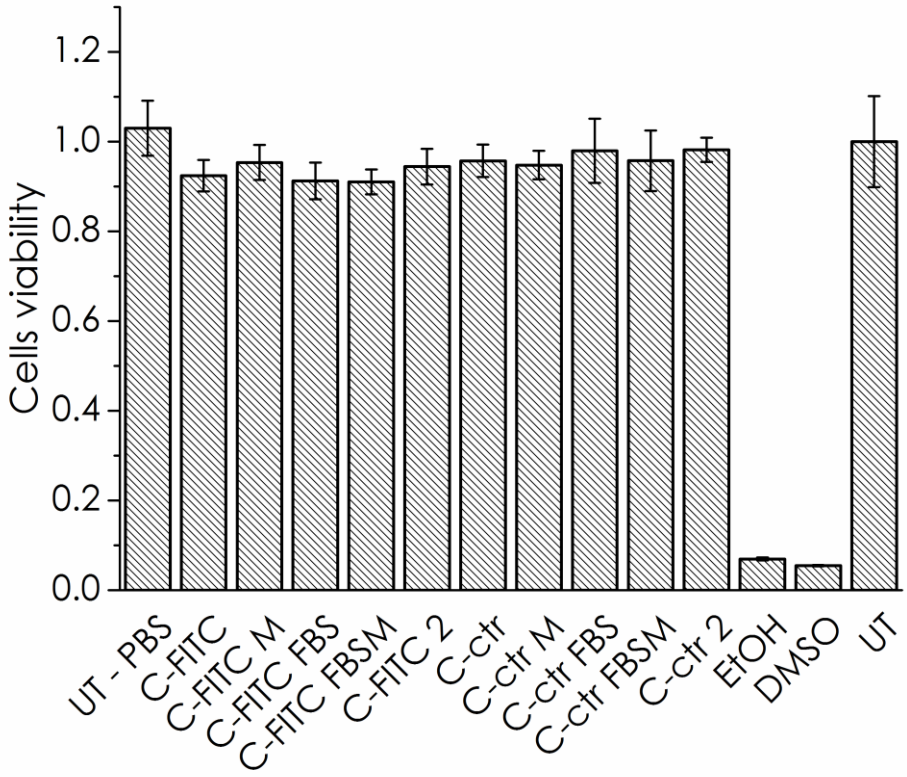

Fig. 42. MTT of CSt PLGA NPs on RAW264.7 culture. MTT test of CSt stabilized PLGA NPs synthesized by WOW. Two formulations were tested, namely with (C-FITC) or without (C-ctr) FITC. Each sample tested after different incubation conditions (M: 20.0% w/v D-mannose; FBS: 10.0% v/v FBS; FBSM: 10.0% v/v FBS and 20.0% w/v D-mannose; 2: dilution 1 to 10 in PBS 1X). Untreated (UT) and PBS treated samples were used as negative controls, while ethanol (EtOH) and DMSO were the positive controls, being cytotoxic agents. NPs were diluted 1 to 100 before 24 hincubation with cells.

The viability ofRAW264.7 after 24 h incubation with amino-PVA stabilized NPs (A-FITC and A-ctr) ranged from 62.2 to 79.8% (Fig. 43). Cytocompatibility was found to be lower than that observed for CSt stabilized samples, as expected because of the presence of cationic charge on the NPs surface. Notably, bioavailabilityin this case was dependent on the surface decoration, being cells treated with non-decorated NPs more viable than all the other conditions.

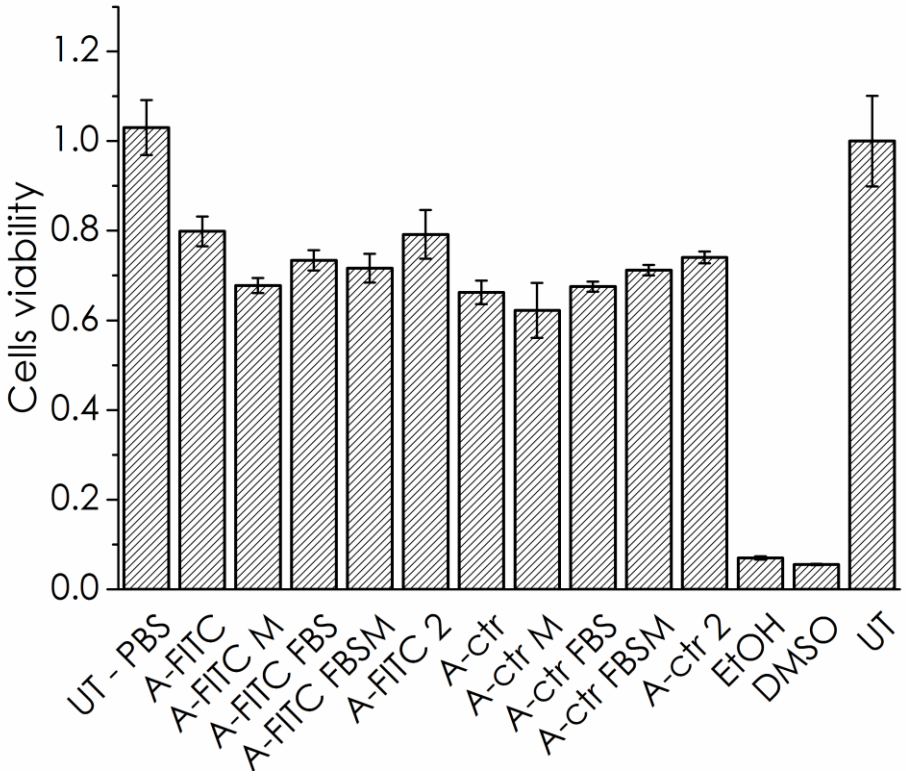

Fig. 43. MTT of amino-PVA PLGA NPs on RAW264.7 culture. MTT test of amino-PVA stabilized PLGA NPs synthesized by WOW. Two formulations were tested, namely with (A-FITC) or without (A-ctr) FITC. Each sample tested after different incubation conditions (M: 20.0% w/v D-mannose; FBS: 10.0% v/v FBS; FBSM: 10.0% v/v FBS and 20.0% w/v D-mannose; 2: dilution 1 to 10 in PBS 1X). Untreated (UT) and PBS treated samples were used as negative controls, while ethanol (EtOH) and DMSO were the positive controls, being cytotoxic agents. NPs were diluted 1 to 100 before 24 h incubation with cells.

Cytotoxicity studies were performed also on a primary culture of mouse bone marrow-derived macrophages. These cells are more sensitive than commercially available cell lines such as RAW264.7, thus representing a model that better mimic *in vivo* conditions. Cytocompatibility of CSt stabilized NPs were found to be lower than in the case of RAW264.7 cell line, as expected because of the higher cells susceptibility (Fig. 44). Moreover, higher error bars as well as reduced effect of cytotoxic agents (EtOH and DMSO) indicated an increased variability in the cellular response. However, cells viability was always higher than 83%, thus indicating good cytocompatibility for CSt stabilized NPs. No major differences were observed between unmodified NPs and NPs decorated under different conditions.

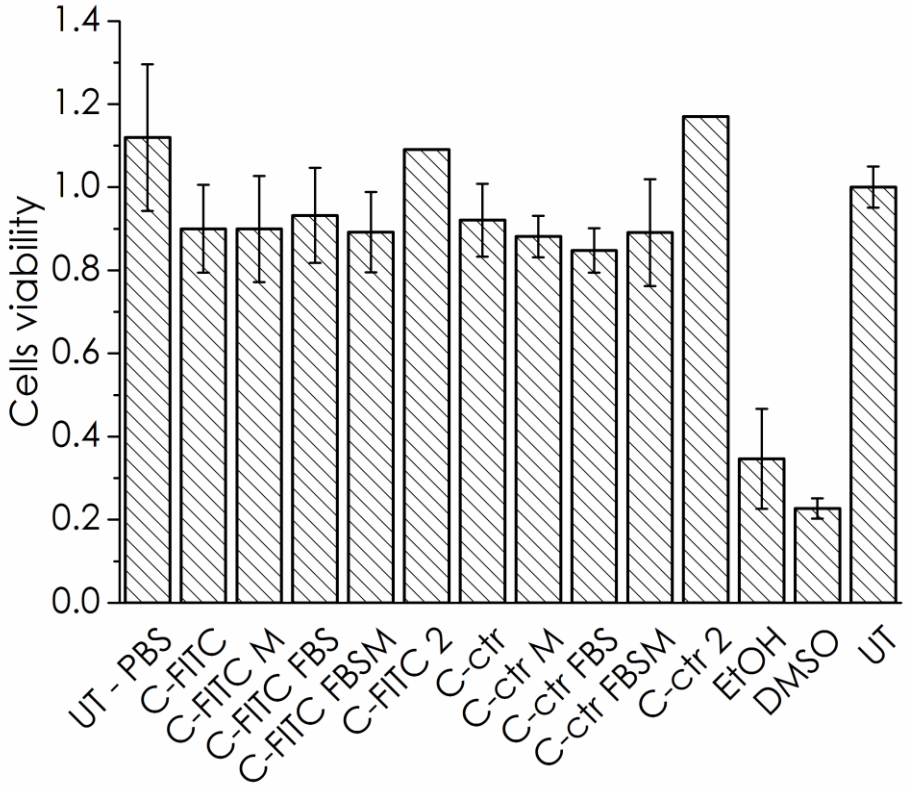

Fig. 44. MTT of CSt PLGA NPs on primary culture of mouse bone marrow-derived macrophages. MTT test of CSt stabilized PLGA NPs synthesized by WOW. Two formulations were tested, namely with (A-FITC) or without (A-ctr) FITC. Each sample tested after different incubation conditions (M: 20.0% w/v D-mannose; FBS: 10.0% v/v FBS; FBSM: 10.0% v/v FBS and 20.0% w/v D-mannose; 2:

dilution 1 to 10 in PBS 1X). Untreated (UT) and PBS treated samples were used as negative controls, while ethanol (EtOH) and DMSO were the positive controls, being cytotoxic agents. NPs were diluted 1 to 100 before 24 h incubation with cells**.**

Finally, amino-PVA stabilized NPs were incubated with primary culture of mouse bone marrow-derived macrophages. As can be seen inFig.45, a high variability was observed especially for A-FITC. For this sample, surface decorated NPs at all the tested conditions were found to be less cytotoxic than the unmodified sample. This was in accordance with data previously reported for RAW267.4 cells. A-ctr showed similar biocompatibility for all the tested conditions (cells viability ranged from 73.4 to 77.6%).

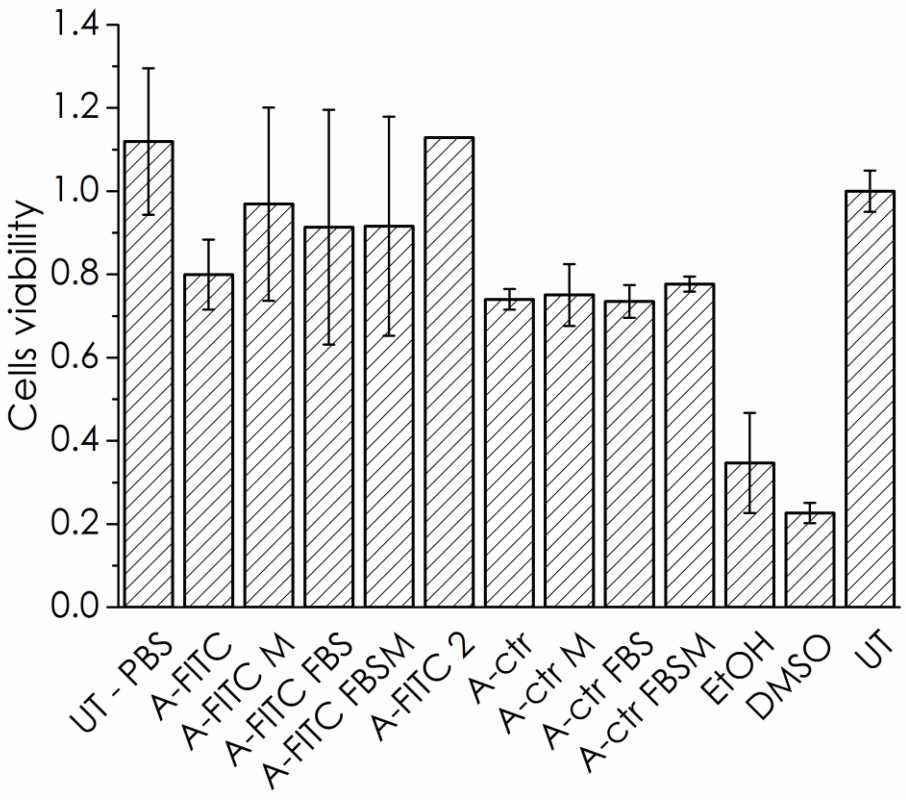

Fig.45. MTT of amino-PVA PLGA NPs on primary culture of mouse bone marrow-derived macrophages. MTT test of amino-PVA stabilized PLGA NPs synthesized by WOW. Two formulations were tested, namely with (A-FITC) or without (A-ctr) FITC. Each sample tested after different incubation conditions (M: 20.0% w/v D-mannose; FBS: 10.0% v/v FBS; FBSM: 10.0% v/v

FBS and 20.0% w/v D-mannose; 2: dilution 1 to 10 in PBS 1X). Untreated (UT) and PBS treated samples were used as negative controls, while ethanol (EtOH) and DMSO were the positive controls, being cytotoxic agents. NPs were diluted 1 to 100 before 24 h incubation with cells.

To note that no major differences were observed between FITC encapsulating systemsand their controls.

These results indicated that the developed PLGA NPs, especially those CSt stabilized, were effectively biocompatible. Further experiments are necessary to confirm NPs biocompatibility even at longer exposition time.

Conclusions

This dissertation was related on the development of polymeric NPs for the specific targeting of Tumor Associated Macrophages (TAMs) as an innovative therapeutic approach for cancer treatment.

Poly (Lactic-co-Glycolic) Acid (PLGA) as safe and versatile material has been used for the development of NPs by single (OW) or double (WOW) emulsion-solvent evaporation method. Different synthetic parameters have been thoroughly investigated, with particular focus on the surfactant role.

The well studied Poly Vinyl Alcohol (PVA) was employed to study the PLGA behavior in both OW and WOW synthesis. Many parameters, including polymer MW and concentration, nature of organic solvent, primary aqueous phase content, ultrasound application, cooling bath temperature and surfactant properties in terms of MW and concentration, have been thoroughly investigated. PVA stabilized NPs underwent also a careful analysis of their degradation properties, with the employment of innovative techniques based on single particle optical extinction and scattering (SPES).

Chemical modification of the PVA structure led to the synthesis of a new polymer, amino-PVA, which has been characterized before its employment as surfactant in PLGA NPs synthesis. The cationic charge presented by amino-PVA is supposedto modulate NPs ability to enter the cells and specially to escape the endosome. Amino-PVA stabilized PLGA NPs synthesis has been optimized and their degradation properties investigated.

Moreover, calcium stearate (CSt) has been presented asan alternative surfactant able to guarantee NPs stability, size and polydispersity similar to PVA, while improving biocompatibility, safety and cost-effectiveness. Parameters involved in CSt stabilized NPs synthesis were thoroughly studied as well as degradation and drug release properties of the developed NPs.

Both amino-PVA and CSt stabilized NPs were found to be able to load curcumin and biomacromolecules, either alone or in combination. Accordingly, the most suitable formulation for drug and gene delivery underwent further investigations.

In order to improve NPs biocompatibility and specific TAMs targeting for both amino-PVA and CSt PLGA NPs, strategies for surface decoration have been investigated. D-mannose as specific molecules to guarantee macrophages recognition was added on the NPs surface in combination with a protein mixture, as a strategy to prevent the inactivation of NPs targeting moieties due the protein corona formation on NPs surface.

Finally, cytocompatibility of the amino-PVA and CSt stabilized NPs have been assessed. All the tested formulations were found to be cytocompatibile for at least 24 h incubation. Further evaluations of their biocompatibility for longer time exposition have to be performed, as well as a careful evaluation of the NPs fate inside the cells after internalization.

This work was possible thanks to the “Fondo per gli Investimenti della Ricerca di Base” (Inflammation and cancer: nanotechnology-based innovative approaches, protocol RBAP11H2R9, year 2010).

Appendix 1

Embedded poly(lactide-co-glycolide) nanoparticles in a micro-pattern collagen scaffold enhanced neuronal tissue regeneration

Limitation in using ethyl acetate as organic solvent was found when monoclonal anti-human CD4-FITC conjugate (CD4-FITC) was encapsulated as model molecule in the NPs inner core (P-CD4-FITC). In this case, NPs synthesized by means of ethyl acetate showed good size (z-average 245.0 nm) and a pdI below 0.15. However too many naked-eye visible aggregates formed during NPs synthesis, leading to a reduction in the final NPs yield. This was probably due to the non ideal condition in the antibody dispersing medium that affected NPs formation. In fact, it was previously reported by Tu F. and Lee D. that the stability of PLGA double emulsions systems depends on the content and the pH of the inner aqueous phase[147].

On the contrary, synthesis by means of DCM and 4.0% w/v PVA (P4-CD4-FITC) were more efficient, even if NPs were slightly bigger (z-average 319.0 nm, pdI 0.199).

These PLGA NPs were tested as candidates for the implementation of collagen-based scaffolds. Thanks to the collaboration with Dr. Laura Blasi (NNL Institute of Nanoscience CNR Lecce, Italy), it was investigated whether collagen-based scaffolds with axially oriented pores, with a pore size suitable for nerve regeneration, can be implemented with PLGA NPs for the sustained and localized release of neurocytokines in the regeneration of long nerve gaps. In the collaborative project, collagen-based scaffolds were synthesized by means of freeze-drying and carbodiimide-based crosslinking. PLGA NPs with a fluorescent antibody were embedded in the scaffold matrix during the freeze drying process. CD4-FITC was selected as encapsulated model molecule to (i) monitor the particles location within the scaffold; (ii) measure the release kinetics of the encapsulated molecule from the scaffold; (iii) verify the molecule's bioactivity in cell culture experiments.

With the aim to prolong PLGA NPs stability during time and allow sustained neurocytokines release, a different monomer ratio was tested: instead of an equal amount of lactic and glycolic monomer (50:50), Lactel® B6001-1P with 65:35 ratio was employed. In fact, lactic acid is more

hydrophobic than glycolic acid. PLGA copolymers containing higher amount of lactide monomer are consequently less hydrophilic, absorb less water, and degrade slower[87]. Moreover, to protect PLGA NPs during the freeze drying process necessary to the scaffold synthesis, D-mannitol was used as cryoprotectant.

Reproducibility was very good: DLS analysis showed NPs with peak size of 328.6±18.4 nm and a pdI of 0.229±0.09 in five different replicates.

The same procedure was used to encapsulate in PLGA NPs a different fluorophore, Cy™3 AffiniPure Goat Anti-Mouse IgG (H+L) (IgG1-Cy3), in order to investigate the system versatility to encapsulate different molecules. P4-IgG-Cy3 NPs showed a 30 nm higher size peak (359.4 nm) with respect to P4-CD4-FITC and an acceptable pdI (0.216).

Confocal microscope analyses were performed before embedded the PLGA NPs in the scaffold, in order to assess effective encapsulation of the model fluorophores. As can be seen in Fig. 46 almost all the NPs showed a fluorescent spot due to the presence of CD4-FITC or IgG-Cy3 in the NPs inner core.

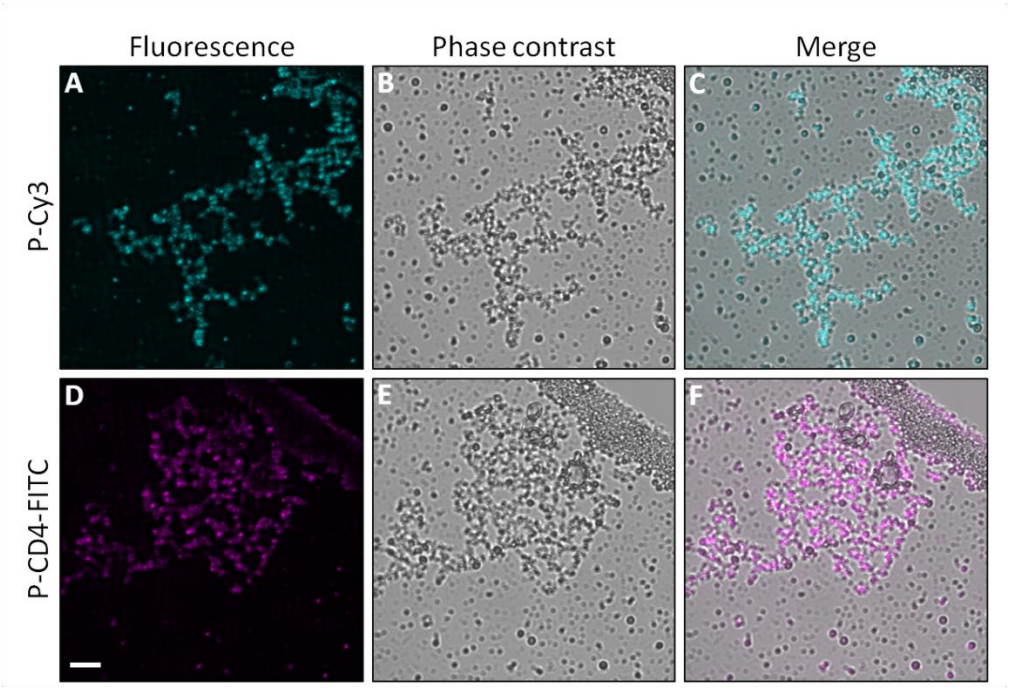

Fig. 46. Confocal microscope analyses for P-CD4-FITC and P-Cy3. By merging (C, F) the phase contrast (B, E) and the fluorescent channels images (A, D), it was possible to note that almost all the NPs actually encapsulated either IgG-Cy3 or CD4-FITC. Scale bar is 5 µm.

Materials and methods

Water-in-oil-in-water (WOW) samples encapsulating Cy™3 AffiniPure Goat Anti-Mouse IgG (H+L) (IgG-Cy3, Jackson Immuno) or monoclonal anti-human CD4-FITC conjugate (CD4-FITC, Sigma Aldrich, a kind gift of Dr. Laura Blasi, from NNL Institute of Nanoscience CNR - Lecce, Italy) were obtained by the use of PLGA 65:35, MW 40-75,000 (Lactel® B6001-1P, ester terminated).

First, 15 µL of 0.1 mg/mL antibody were added at 300 µL of PLGA in dichloromethane (DCM). Primary water-in-oil emulsion was obtained by means of 15 sec ultrasounds at 30% of amplitude in ice bath. Then, 1.2 mL of 4.0%w/v Poly(Vinyl) Alcohol (PVA, Mowiol® 4-88 MW 31,000, 86.7-88.7 mol% hydrolysis) were addition and sonicated using the same protocol described above, thus obtaining the multiple water-in-oil-in-water emulsion. Finally, the WOW emulsion was diluted in 15 mL of dispersing phase (0.4% w/v PVA) and solvent was evaporated via magnetic stirring for 3.5 h.

P-Cy3 and P-CD4-FITC were collected and washed with three cycles of centrifugation at 15,000 g for 20 min at 4°C, in order to remove exciding surfactant, as well as not encapsulated antibodies. Pellets were then resuspended in 1.0 mL of 20% w/v D-mannitol and an additional centrifugation cycle was done before samples stocking.

Samples characterization was performed as described in the paragraph 5. Nanoparticle characterization page 54 of the Materials and methods section of the main text.

Appendix 2 - The Nanotox project

This work has been supported by Fondazione CARIPLO for the project “Toxicology of chronic exposure to engineered silver nanoparticles”, under the Program “Nanoparticles, nanotechnologies and ultrafine particles".

1. A Practical Approach to Assess the Stability of Isolated Silver Nanoparticles in Complex Biological Media

Abstract

The widespread use of engineered silver nanoparticles (AgNPs) in commercial products is currently raising concerns about their potential for adverse health effects in humans and environment. Although an increasing number of studies *in vitro* and *in vivo* are being reported on the toxicity of AgNPs, most of them suffer from incomplete characterization of AgNPs in the tested biological media. Hence the issue of toxicity is an open critical question and the comparison of toxicological data very difficult. Accordingly, the development of a practical and reliable method for assessing correct size and attitude to reactivity of AgNPs under the exposure conditions is urgently required to predict the toxicological effects of AgNPs.

Here we studied the stability of AgNPs in two relevant biological media, namely 10% Fetal Bovine Serum (FBS), which resembles the protein composition of a typical cell medium, and mouse plasma (MP). In this regard, three different techniques (Dynamic Light Scattering, Transmission Electron Microscopy, UV-vis spectroscopy) were tested for their suitability in detecting AgNPs of three different sizes (10, 40 and 100 nm) coated with either citrate or polyvinylpyrrolidone (PVP). Results showed that UV-vis spectroscopy was the most versatile technique to predict the behavior of such a wide range of AgNPs conditions, because of its ability to characterize all the tested AgNPs in both the examined biological media. Finally our discussion provides comprehensive

guidelines to interpret the UV-vis spectra and assess the AgNPs stability in practical experimental settings.

Introduction

Because of their enhanced antiseptic activity, engineered silver nanoparticles (AgNPs) – *i.e.* intentionally produced silver particles with size ranging from 1 to 100 nm- are currently incorporated in an increasing number of consumer products[148–151].

The widespread use of AgNPs and their subsequent disposal in the environment imply that human exposure to AgNPs is expected to increase in the future, therefore the assessment of AgNPs toxicity (*in vitro* and *in vivo*) is urgently needed to guarantee consumer safety[152–154]

AgNPs can entry the body through different routes (ingestion, inhalation, dermal contact) and reach the systemic circulation[155]. It is widely established that AgNPs in biological media such as blood readily interact with surrounding biomolecules (proteins, lipids, etc), leading to the formation on their surface of a protein corona[101,156]. The protein coated AgNPs represent new molecular entities that determine the biological response, including cellular uptake, route of clearance and accumulation in target organs and tissues[102].

AgNPs in biological fluids can also lead to agglomeration (*i.e*. weakly bonded particles), aggregation (*i.e*. strongly bonded or fused particles) as well as release of silver ions, thus their size can be highly different from that reported by the manufacturer[157–160].

To date, an increasing number of studies on the toxicity of AgNPs have been reported[100,161–163]. However, many key questions on the AgNPs toxicity mechanism still remain unanswered. The main reason is the lack of proper characterization of the tested AgNPs under the exposure conditions, which makes difficult to attribute a certain property to the observed toxic effects.

To this purpose, Murdock *et al.* exploited Dynamic Light Scattering (DLS) in conjunction with Transmission Electron Microscopy (TEM) to determine the physicochemical characteristics of a wide range of nanomaterials, including AgNPs, in complex biological media[164]. However, the detection of AgNPs with these techniques suffered from several drawbacks. Interpreting the DLS

data of polydisperse suspensions is troublesome because of interferences due to large or high-refractive-index particles[165]. TEM measurements are time-consuming because a large number of particles need to be analyzed and results are uncertain due to possible artifacts during sample preparation.

Accordingly, there is still the need for a method to determine the environment-dependent size of AgNPs in a reliable and easy to access way. Ideally, this method should satisfy three main requirements: (i) ability to analyze AgNPs of different size/coating; (ii) minimal sample processing before analysis; (iii) employment of facile and affordable equipment.

In addition to DLS[166,167] and TEM[159], other techniques have been explored, such as Field Flow Fractionation[168,169], sedimentation/centrifugation[170]and UV–visible (UV-vis) spectroscopy[171]. In particular, the UV-vis spectroscopy exploits the surface plasmon resonance (SPR) feature of metallic nanoparticles[172]. Although this is a simple and valuable technique, interactions of nanoparticles with ions and biomolecules greatly complicate interpretation of the experimental data.

In this paper, a practical approach and comprehensive guidelines to assess the stability of AgNPs in both in vitro and in vivo conditions are presented. In this regard, AgNPs of three different nominal sizes (10, 40 and 100 nm), coated with either citrate (CT) or polyvinylpyrrolidone (PVP), have been studied in two relevant biological media, namely 10% Fetal Bovine Serum (FBS), which resembles the protein composition of a typical cell medium, and mouse plasma, mimicking the *in vivo* conditions.

Three different techniques, namely UV-vis spectroscopy, DLS and TEM were applied to test their suitability in detecting such a wide range of AgNPs conditions.

The presented study is expected to provide useful insights and practical guidelines to assess the AgNPs stability in the tested experimental conditions, therefore contributing to more reliable *in vitro* and *in vivo* nanotoxicity results. All of this could be of relevance to assess the ability of AgNPs to pass biological barriers as well as to reduce their potential risks for humans and environment.

Materials and methods

Chemicals. Silver Nanoparticles (AgNPs) of 10, 40 and 100 nm in size, coated with either citrate (CT) or polyvinylpyrrolidone (PVP), were purchased from NanoComposix (San Diego, USA) and used as received. In the text, citrate coated AgNPs of 10, 40 and 100 nm were named 10CT, 40CT and 100CT, respectively; the PVP coated AgNPs of 10, 40 and 100 nm were named 10PVP, 40PVP and 100PVP. All the suspensions were provided at the concentration of 1.0 mg/mL. Fetal Bovine Serum (FBS), poly-L-lysine and sodium citrate were purchased from Sigma Aldrich. Grids for electron microscopy characterization were obtained from Pelco. The Mouse Plasma (MP) was kindly provided by Mouse and Animal Pathology Lab, Filarete Foundation. Bidistilled water (MilliQ, Millipore) was employed in all the experiments.

Quality control on commercially available AgNPs. The CT- and PVP-coated AgNPs were diluted with 2.0 mM sodium citrate buffer and MilliQ water, respectively, and carefully resuspended by vigorous shaking. If necessary, samples were sonicated (Elmasonic S 30 H) for up to 30 seconds, in accordance with the manufacturer's instructions. Before use, the AgNPs were characterized by DLS, TEM and UV-vis spectroscopy, in order to check the agreement of AgNPs' size with the manufacturer's stated description. Details on the characterization procedure are reported in the Supplementary Data.

Experiments with biological media. Experiments were run in two different biological media mimicking the *in vitro* and *in vivo* conditions: (i) a typical cell culture medium (fetal bovine serum, FBS, 10% v/v) and (ii) mouse plasma (MP, 100% v/v). Indeed, 10% FBS was a widely used concentration of FBS in cell culture media, whereas mice were the selected models for further *in vivo* toxicity assessment[173].

Experiments with FBS. The AgNPs were suspended in 1.0 mL of 10% FBS at the concentration of 50.0 µg/mL and incubated at 37°C. At fixed time points (5 min, 24 h) samples were characterized by DLS and UV-vis spectroscopy. To check the effect of FBS concentration on the protein corona formation, the same experiments were run in 100% FBS.

Experiments with MP. The experiments were run in the same way as with FBS, with the exception of the overall volume. Indeed, each AgNPs sample was prepared using 50 µL of MP. The AgNPs were suspended in 100% MP at the concentration of 50.0 µg/mL and characterized by DLS and UV-vis spectroscopy at determined time points. To assess the effect of the MP concentration, experiments were also run using 10% MP.

Dynamic Light Scattering (DLS). The hydrodynamic diameter of AgNPs in solution was measured by DLS technique. Measurements were performed with a Malvern Zetasizer ZS90 instrument operating with a light source wavelength of 633 nm and a fixed scattering angle of 90°. In the experiments with FBS and MP, samples were centrifuged (10,000 g, 10 min) at room temperature (RT), to pellet the AgNPs-protein complexes and remove excess proteins. The obtained pellet was washed three times by resuspending in MilliQ water and changes in mean hydrodynamic diameter were measured by DLS. All the measurements were run at RT for at least three times.

Transmission Electron Microscopy (TEM). The protein corona morphology was studied byTEM (FEI Tecnai 200kV). To this aim, Formvar-coated copper grids were previously treated with 0.01% (w/v) poly-L-lysine for 10 min and washed with water. Then the AgNPs-protein corona complexes were fixed with 2.53% (w/v) glutaraldehyde for 1 h and deposited on poly-L-lysine-coated grids. After 15 min, the exceeding samples were removed by washing with water and the grids were left under vacuum overnight.

UV-vis Spectroscopy. The UV-vis spectra were acquired in the 300-800 nm range using a Cary 100 Spectrophotometer (Agilent). In the experiments with FBS and MP, samples were detected without further purification. Since the operating volume in MP experiments was very small, UV-vis spectra were acquired using an ultra-low volume cuvette with a 4 mm path length and a 1x2 mm window. The absence of aggregates was evaluated by considering absorbance in the wavelength range of 600-800 nm. All the measurements were run at RT for at least three times.

Results

In order to achieve standardized results, commercially available AgNPs were used in all the experiments. Since poorly characterized samples can led to confusing or even mis-interpreted results, thorough characterization of AgNPs was performed before any experiment. The results obtained by UV-vis spectroscopy, DLS and TEM indicated narrow size distribution and absence of any aggregates in the AgNPs suspensions (seeSupplementary data page144).

To realistically mimic *in vitro* and *in vivo* conditions, the stability of AgNPs was tested in fetal bovine serum (10% FBS) and mouse plasma (100% MP), being 10% FBS one of the most commonly used concentration of FBS in cell culture media and mice the selected models for *in vivo* toxicity assessment[173].

Experiments with FBS. First, the AgNPs stability was detected by DLS, which represents the most widely used method to measure the hydrodynamic diameter of nanoparticles in suspension[166]. Although DLS allows for fast and reliable size measurements, exceeding proteins heavily affected the analysis. Accordingly, the nanoparticle-protein complexes (Fig. 47 panel A) have to be separated from unbound proteins, usually by centrifugation. The purification process consisting of three-cycles of centrifugation was successful for 100 nm and partly for 40 nm-sized AgNPs. However, the 10 nm AgNPs did not sediment by centrifugation and their DLS results are not reported. Due to partial sedimentation, the DLS data of 40 nm-sized AgNPs require careful examination (see Supplementary data page144).

Instead, the DLS results of 100 nm-sized AgNPs, coated with either citrate (100CT) or PVP (100PVP) provided several insights in understanding the protein corona formation (Fig. 47). Indeed, the hydrodynamic diameter of 100CT (98.5 nm) was found to be higher in 100% FBS (191.0 nm) than in 10% FBS (131.0 nm), whereas no differences were visible after incubating 100PVP (131.0 nm) with either 10% FBS or 100% FBS (205.0 and 208.0 nm, respectively). The behavior of 100PVP could be explained by considering the stealthiness of PVP, which prevented increase in protein adsorption while increasing the protein content of the suspending medium.

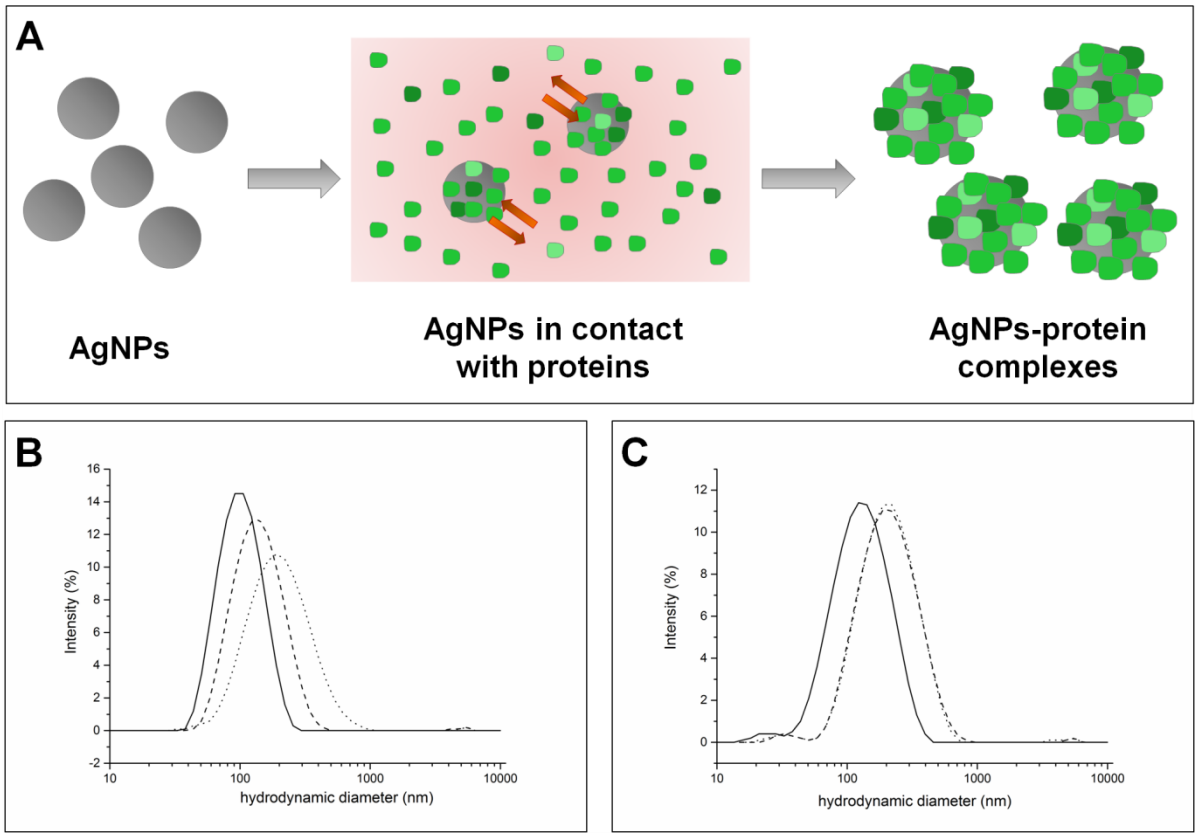

Fig. 47. General scheme of AgNPs-protein complexes formation. (A) Size distributions of 100 CT (B) and 100 PVP (C) before (solid) and after 24h incubation with 10% FBS (dash) and 100% FBS (dot).

To further investigate the nanoparticle-protein interactions, surface charge (ζ-potential) measurements were performed. This parameter is important in determining the biological impact of the nanoparticle–protein corona complexes because surface charge strongly influences interactions with cells and toxicity[174]. Similarly to DLS analysis, samples were processed by three centrifugation cycles to remove excess proteins, which was feasible only for 100 nm and partly 40 nm-sized AgNPs. Due to limitations in the purification process, the 10 nm-sized AgNPs did not provide any affordable result.

To assess the effect of AgNPs coating on the surface charge, ζ-potential measurements were performed on 100CT and 100PVP before and after incubation with 10% FBS and 100% FBS, as shown in Fig. 48.

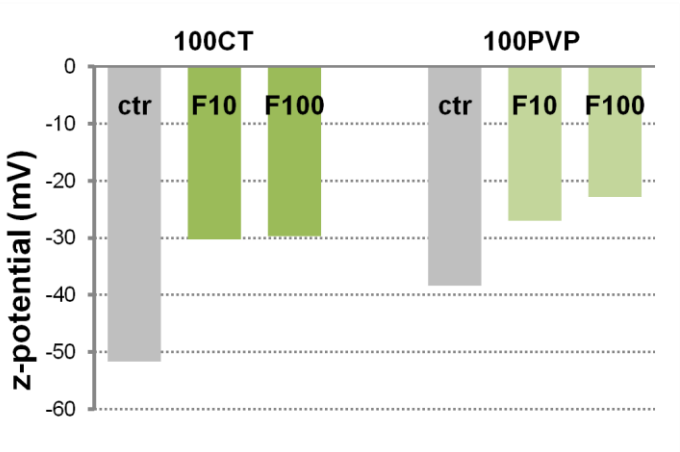

Fig. 48. ζ-potential values of 100 nm-sized AgNPs before (ctr) and after 24h incubation with 10% FBS (F10) and 100% FBS (F100).

Before incubation, the tested AgNPs were negatively charged. This was expected because sodium citrate (CT) and polyvinylpyrrolidone (PVP) as stabilizing agents yield particles with a negative surface charge at physiological pH[175]. After 24 h incubation with either 10% FBS or 100% FBS, the ζ potential of both 100CT and 100PVP underwent a decrease in its absolute value (became less negative). Although proteins adsorbed onto the AgNPs surface reduced the electrostatic repulsions, they were found to stabilize AgNPs and prevent their aggregation[176]. These data suggested that both the most abundant and the most affine proteins were neutral or positively charged at physiological pH.

In order to assess the morphology and size of AgNPs upon incubation with either 10%FBS or 100%FBS, TEM analyses were performed. The protein corona was clearly visible in 40CT and 100CT, since a thin layer all over these samples was detected (Fig. 49 panel d and panel f). The absence of any artifacts was determined by treating AgNPs controls in the same way (*i.e.* incubation with 2.53% glutaraldehyde), as shown in Fig. 49 panelc and panel e. Notably, the protein corona was not observed in 10CT. In particular, besides single NPs, the 10CT showed aggregates of several hundreds of nm (Fig. 49 panel b) that could be due to particle aggregation during sample drying.

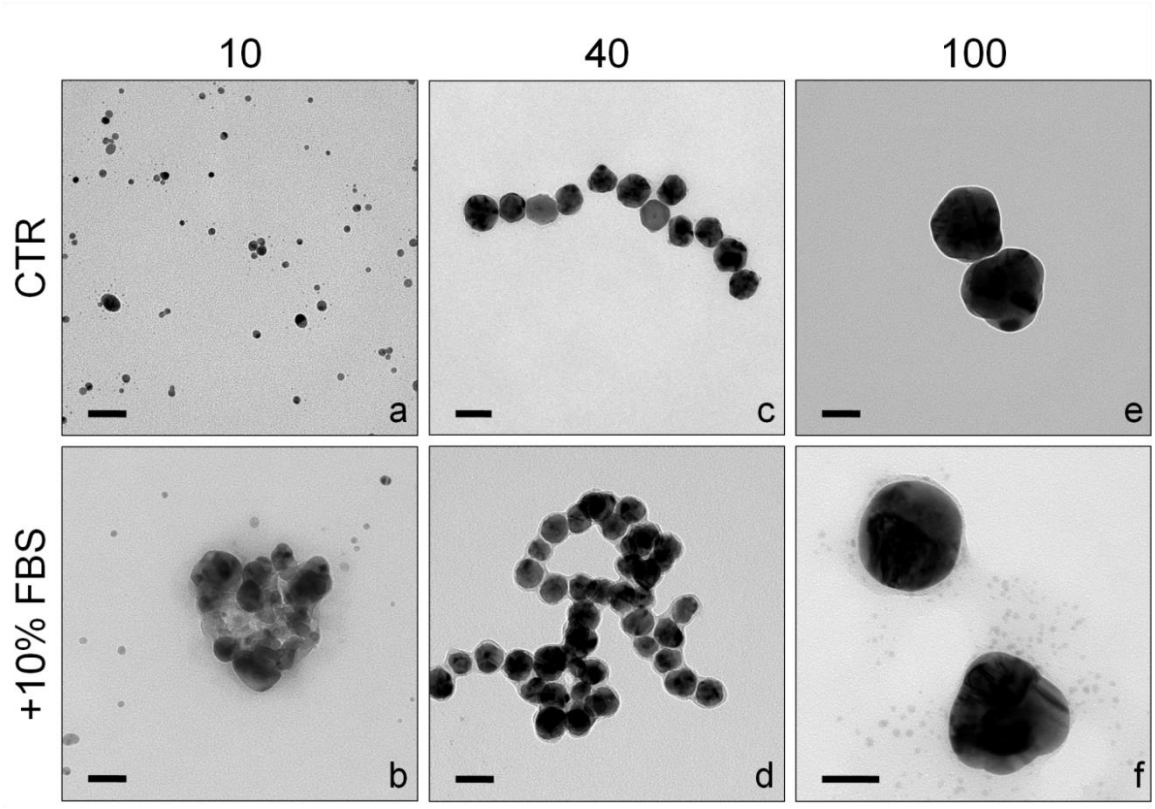

Fig. 49. TEM images of 10 nm (a, b), 40 nm (c, d) and 100 nm sized (e, f) AgNPs coated with citrate. The AgNPs were incubated with 10% FBS for 24 h, then the protein corona was fixed with 2.53% glutaraldehyde (b, d, f). Control AgNPs were also prepared using the same sample processing (a, c, e). Scale bars are 50 nm.

Dealing with the PVP-coated AgNPs, the protein corona was clearly visible in 40PVP and 100PVP, whereas aggregates of several hundreds of nm were observed in the 10PVP (Fig. 50).

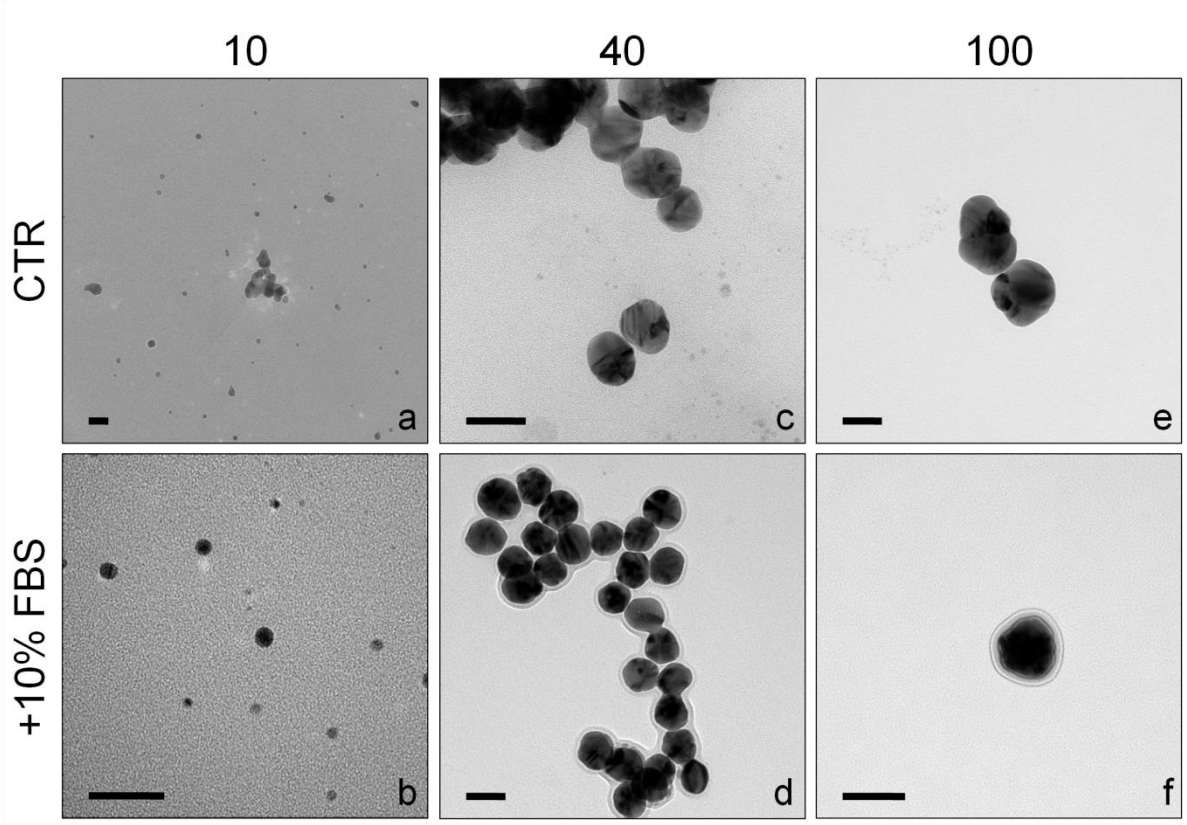

Fig. 50. TEM images of 10 nm (a b), 40 nm (c, d) and 100 nm sized (e, f) AgNPs coated with PVP. The AgNPs were incubated with 10% FBS for 24 h, then the protein corona was fixed with 2.53% glutaraldehyde (b, d, f). Control AgNPs were also prepared using the same sample processing (a, c, e). Scale bars are 50 nm.

Finally, the AgNPs stability in FBS was detected by UV-vis spectroscopy. This is a key technique for optical characterization of AgNPs, since they exhibit a characteristic absorbance maximum in the visible range, *i.e.* the surface plasmon resonance (SPR) peak, describing the collective response of conduction electrons in a metal under electromagnetic excitation. Optical properties of AgNPs are closely related to their size, shape and surface alterations and, furthermore, the SPR is sensitive to the surroundings of the NPs at the molecular level. Thus, inspection of the SPR feature would

allow detecting the presence of aggregates and investigatingchanges in the close environment of the NPs (such as the protein corona).

To assess the effect of FBS concentration on protein corona formation, the UV-vis spectra (Fig. 51) were acquired by suspending the AgNPs in 10% FBS and 100% FBS. The main optical parameters are summarized in Table 20.

	λ_{max}			H_{max}			Red shift	
	ctr	**F10**	**F100**	**ctr**	**F10**	**F100**	**F10**	**F100**
10CT	394	406	403	2.90	2.48	1.25	12	9
40CT	410	418	417	3.27	2.96	2.42	8	7
100CT	482	493	489	0.99	1.03	0.98	11	7
10PVP	397	400	401	1.11	1.14	0.65	3	4
40PVP	409	415	414	2.7	2.68	2.13	6	5
100PVP	492	497	493.5	0.83	0.76	0.70	5	1.5

Table 20. Main optical parameters of AgNPs suspensions in 10%FBS (F10) and 100% FBS (F100). Control samples (ctr) were prepared using 2.0 mM sodium citrate buffer and MilliQ water for CT- and PVP-coated AgNPs, respectively. λ_{max}: maximum wavelength; H_{max}: maximum absorbance.

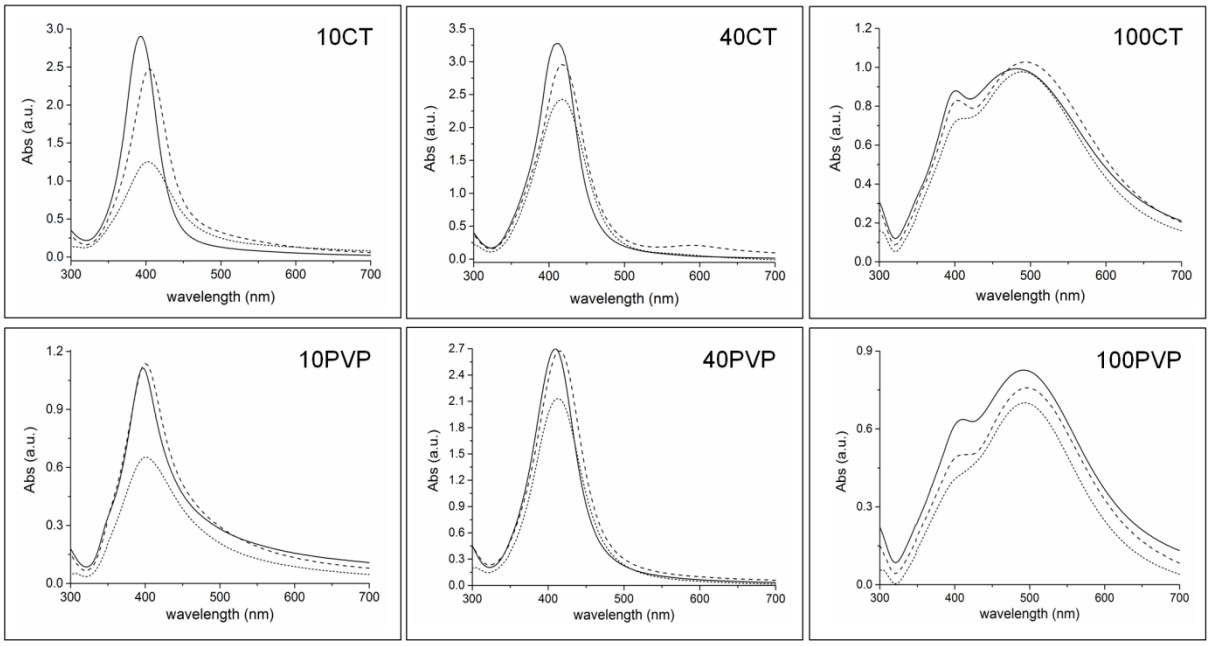

Fig. 51. Absorption peaks of control AgNPs (solid), AgNPs after 24 h incubation with 10% FBS (dash), AgNPs after 24h incubation with 100% FBS (dot). 10CT, 40CT and 100CT are AgNPs of three different sizes (10, 40, and 100 nm respectively), coated with citrate (CT) as capping agent. 10PVP, 40PVP and 100PVP are 10 nm, 40 nm and 100 nm AgNPs coated with polyvinylpyrrolidone (PVP). Slight evidences of aggregation were found only in the 40CT sample incubated with 10% FBS.

After incubation with either 10% FBS or 100% FBS, the spectral position of the maximum wavelength (λ_{max}) of all the tested AgNPs showed a shift towards increasing wavelength values, meaning an energy red shift. In the 100 nm-sized AgNPs, a two-fold peaked wide band was observed, due to the convolution of the broadened plasmonic band with a band centered on 500 nm. Therefore, the λ_{max} of the plasmonic band of 100CT and 100PVP is not reported in Table 20 because the SPR peak feature is lost in these samples.

The SPR peak was found to red-shift much more in the CT-coated AgNPs as compared to the PVP-coated ones. Moreover, the smaller the AgNPs size, the higher was the SPR red-shift, as expected due to the enhanced surface-to-volume ratio.

Further, with the exception of 100 nm-sized AgNPs, a remarkable decrease of the maximum absorbance was observed while increasing the concentration of the biological medium (10% FBS and 100% FBS). For the CT-coated AgNPs, it was found that the lower the size, the more evident was the decrease of H_{max}. In particular, the concentration of FBS seemed not to affect the overall optical properties of 100CT, since both the height and shape of the absorbance peaks after incubation in 10% and 100% FBS medium were pretty similar to the control. However, after incubation with either 10% FBS or 100% FBS, the 10CT and 40CT underwent a relevant decrease in the maximum absorbance by one third and two-thirds, respectively. A similar trend, although less pronounced, was found for the PVP-coated AgNPs.

Notably, the decrease in absorbance value cannot be ascribed to the formation of AgNPs aggregates, whose typical peak in the 600-800 nm range was absent in all the tested samples, with the exception of 40CT sample incubated with 10% FBS. To the best of our knowledge, the observed decrease in absorbance value after interactions with biological media has not been reported so far.

Experiments with MP. Similarly to FBS experiments, AgNPs samples incubated with either 10% or100% MP were characterized by DLS and UV-vis spectroscopy to determine their stability. The DLS data provided further evidences of both the protein corona formation and the stealthiness of PVP-coated AgNPs (see Supplementary data page144). The UV-vis results are shown in Fig. 52. It is worthy to note that MP has a characteristic absorption peak at about 412 nm, which was particularly evident in the 100% MP sample. Accordingly, the absorption peaks reported in Fig. 52 were obtained by subtracting the spectrum of either 10% or 100% MP.

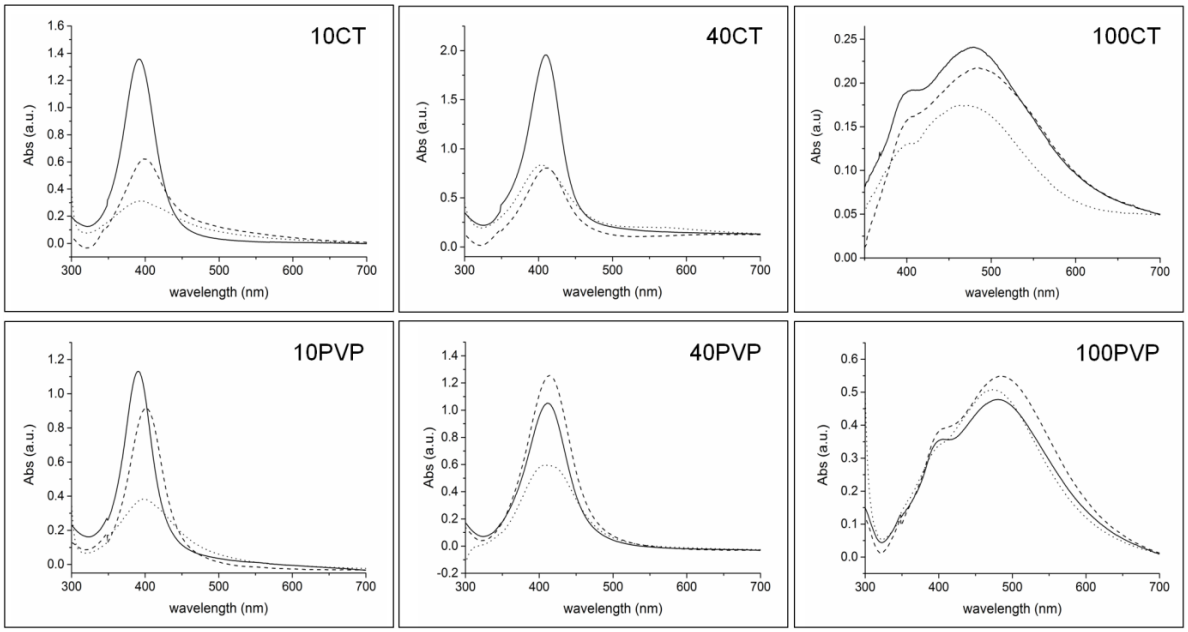

Fig. 52. Absorption peaks of control AgNPs (solid) and AgNPs after 24 h incubation with 10% MP (dash) and 100% MP (dot).

As in the experiments with FBS, the red-shift of the SPR peak (ascribed to changes in the dielectric environment) and the reduction of H_{max} were more evident in AgNPs samples with size of 10 and 40 nm (Table 21). In general, these SPR features in the experiments with MP were found to be more pronounced than after incubation with FBS, as expected because MP had numerous additional components with respect to FBS, including antibodies.

	λ_{max}			**H_{max}**			**Redshift**	
	ctr	**MP10**	**MP100**	**ctr**	**MP10**	**MP100**	**MP10**	**MP100**
10CT	392	399	394	1.357	0.622	0.312	7	2
40CT	410	412	404	1.956	0.805	0.833	2	-6
100CT	480	484	469	0.241	0.217	0.174	4	-11
10PVP	390	402	399	1.131	0.915	0.383	12	9
40PVP	412	414	413	1.051	1.255	0.593	2	1
100PVP	481	486	474	0.478	0.549	0.508	5	-7

Table 21. Main optical parameters of AgNPs suspensions in 10% MP (MP10) and 100% MP (MP100). Control samples (ctr) were prepared using 2.0 mM sodium citrate buffer and MilliQ water for CT- and PVP-coated AgNPs, respectively**.**

Discussion

It is widely accepted that accurate size measurements under the exposure conditions are required to well-design *in vitro* and *in vivo* studies and correctly predict the toxicological effects of AgNPs[163,164]. In this work, in order to develop an effective approach to analyze AgNPs of different size with minimal sample processing, three different techniques have been considered, namely DLS, TEM and UV-vis spectroscopy.

The DLS has been extensively exploited to determine the particle size and surface charge of AgNPs suspended in biological media[164]. Although DLS measurements are fast and reliable, this technique suffers from several limitations. First, it is necessary to separate by centrifugation the nanoparticle-protein complexes from exceeding proteins, to achieve accurate analysis and avoid sample artifacts. Such a purification, besides the possibility to alter the nanoparticle-protein complexes, is critical for small (*i.e.* 10 nm-sized) AgNPs. Moreover, since serum proteins contribute to the scattered light and interfere with signals from AgNPs, the DLS characterization of particles in biological media is very challenging[165].

The TEM analysis provided valuable images on the protein corona and nanoparticle distribution. However, complex sample preparation can profoundly change the nanoparticle-protein complexes and sample artifacts can be formed during sample drying. Therefore, although TEM analysis represents a useful inspection tool to gain general morphological information on AgNPs, its employment to routinely assess the AgNPs stability is limited[165,177].

Differently, the UV-vis spectroscopyallowed for fast and reliable results with minimal sample processing. Since exceeding proteins did not affect the overall optical properties of AgNPs, any purification step was required before sample analysis. Accordingly, the UV-vis spectroscopy was found to be effective in analyzing the 10 nm-sizedAgNPs, which were difficult to be detected by either DLS or TEM. Because of its wide range of applications, the UV-vis spectrophotometer is a commonly available tool in biological laboratories, which are usually not equipped with particle analysis instruments. Therefore, *in situ* analyses to assess the AgNPs stability before either *in vitro* or *in vivo* experiments are feasible.

However, interactions of AgNPs with ions and biomolecules in the tested medium may greatly complicate the understanding of the UV-vis data, therefore comprehensive guidelines to assess the AgNPs stability are demanding. In this work, main criteria for interpreting the UV-vis spectra are provided (Table 22).

	λ_{max}	H_{max}	**Notes**
Protein corona formation	↑	↓	The lower the AgNPs size, the more accentuated are these changes
Aggregation	-	↓	Absorbance in the 600-800 nm range Multiple Abs peaks
Agglomeration	-	-	No substantial changes in optical properties

Table 22. Summary of optical changes observed after protein corona formation, agglomeration and aggregation of AgNPs.

The simultaneous increase of the λ_{max} value (namely a red shift) and the reduction of the H_{max} value are associated to the protein corona formation, thus indicating that nanoparticles are well suspended in the tested medium. Notably, the smaller the AgNPs size, the more evident are these changes.

The appearance of multiple absorption peaks, especially in the 600-800 nm range indicate the formation of aggregates in terms of fused or strongly bonded AgNPs. Since aggregates do not exhibit the SPR absorption peak, under these conditions the H_{max} value is reduced. Both the appearance of additional absorption peaks and the decrease of H_{max} value indicate that nanoparticles in the tested media are irreversibly modified. Therefore, any affordable biological experiment can be run under these conditions.

Finally, the absence of substantial changes in optical properties suggests that AgNPs in the medium formed agglomerates, namely weakly bonded particles. An additional evidence of agglomeration is provided by the appearance of larger peaks in the DLS analysis. Hence, vigorous shaking is sufficient to enable further processing and experiments.

In summary, here we deeply discuss guidelines for assessing the AgNPs fate under the exposure conditions in *in vivo* and *in vitro* experiments. AgNPs of three different size (10, 40 and 100 nm), coated with either citrate (CT) or polyvinylpyrrolidone (PVP) were tested in two different biological media (FBS and MP). Practical drawbacks of Dynamic Light Scattering (DLS) and Transmission Electron Microscopy (TEM) in detecting AgNPs were considered and discussed. Instead, the UV-vis spectroscopy was found to be the most versatile technique to predict the behavior of the wide range of AgNPs conditions. The UV-vis results suggested that the AgNPs' stability was highly dependent on both the size and coating of AgNPs. Indeed, changes were more evident in CT- than in PVP-coated AgNPs, in accordance with the current knowledge about PVP, which is able to induce stealth behavior and to extend the persistence of nanoparticles inside the body. Further, the lower the size of AgNPs, the more pronounced were the optical changes due to the protein corona formation and the influence of the suspending biological medium. Finally, the increase in nanoparticle hydrodynamic diameter was much higher in the MP than in 10% FBS, as expected because of the higher concentration of proteins in MP.

Overall, the proposed approach based on UV-vis spectroscopy is expected to provide biological researchers with useful insights to easily assess the stability of AgNPsin *in vitro/in vivo* experiments, thus contributing to more reliable nanotoxicity results.

Supplementary data

Supplementary methods

Quality control of silver nanoparticles (AgNPs).

In order to prevent contamination, measurements were run using disposable plastic cuvettes. The AgNPs were tested immediately after their delivery.

Dynamic Light Scattering (DLS). The actual size of AgNPs in dispersion was measured by DLS. All the nanoparticles were diluted 1:100 with the exception of 10 nm-sized AgNPs. Indeed, due to their small size, the 10 nm AgNPs presented increased absorption and lower scattering intensity compared to 40 nm and 100 nm AgNPs. Accordingly, the 10 nm AgNPs were diluted 1:50. All measurements were run at room temperature for at least three times.

UV-visible (UV-vis) Spectrophotometry. The UV-Vis spectra were acquired in the 300-800 nm range using a Cary 100 (Agilent) spectrophotometer. All the nanoparticles were diluted 1:100 with the exception of 10 nm AgNPs, which were diluted 1:200 because of their increased UV-Vis absorbance with respect to larger nanoparticles. All measurements were run at room temperature for at least three times.

Transmission Electron Microscopy (TEM). Formvar coated copper TEM grids (cod. PE1GC300, Pelco) were pre-treated with 20 µl of poly-L-lysine 0.01% (w/v) (Sigma Aldrich) for 15 minutes. After washing twice with MilliQ water, 3 µL of AgNPs suspensions were deposited onto the grid for 5 minutes and then rinsed with 3 µL of 2-propanol (Sigma Aldrich). According to the manufacturer's advice, 100 and 40 nm AgNPs were used at the concentration of 1.0 mg/mL, while 10 nm AgNPs were diluted up to 0.1 mg/mL before use. The grids were allowed to dry overnight at room temperature in a covered crystallizing dish. TEM (FEI Tecnai G2, Eindhoven) images were analyzed with the Image J software to obtain the nanoparticles dimensional distribution. In particular, small objects due to background and overlapping nanoparticles were omitted by using proper cut-off filters and Feret diameter (intended as the larger diameter of the NP projection)

was used to evaluate the size of the particles. For each sample, a minimum of about 250 nanoparticles was considered.

TEM measurements

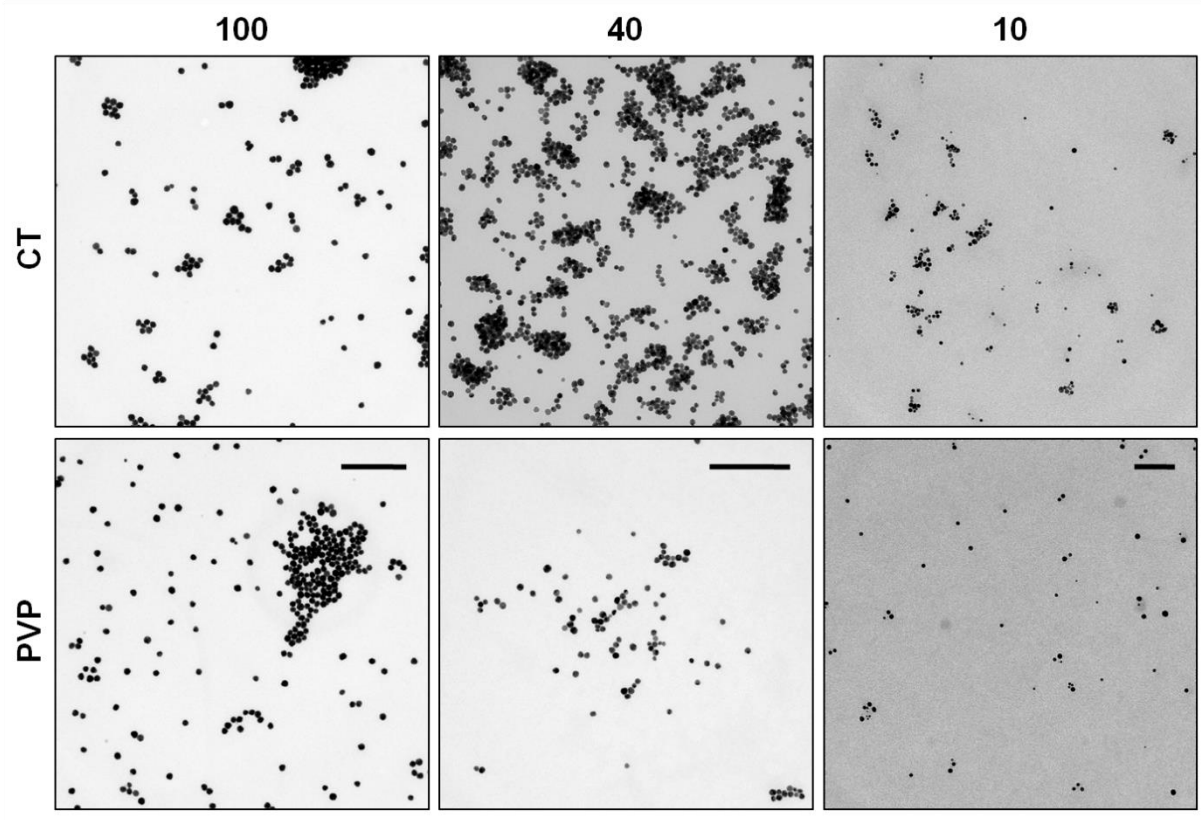

Fig. 53. TEM images of 10 nm, 40 nm and 100 nm-sized AgNPs coated with citrate(CT) and polyvinylpyrrolidone (PVP) for quality control. Scale bars are: 1µm for 100 nm-sized AgNPs; 500 nm for 40 nm-sized AgNPs; 100 nm for 10 nm-sized AgNPs.

Particle size analysis

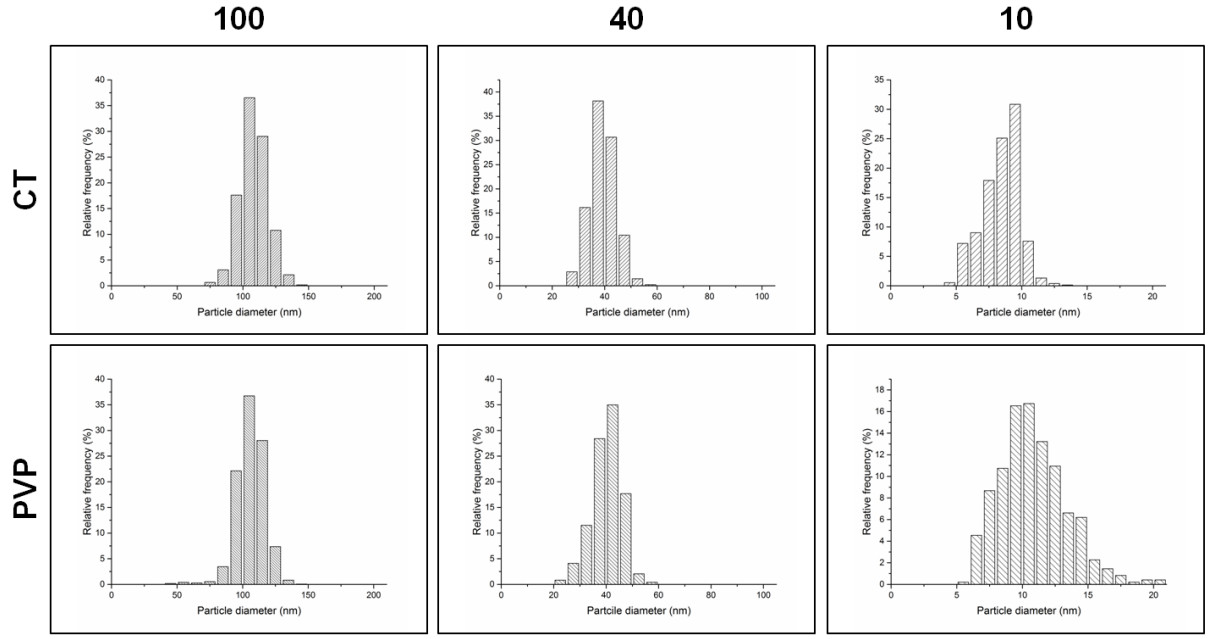

Fig. 54. Feret diameter distributions of 10, 40, 100 nm-sized AgNPs coated with CT or PVP.

Table 23.

	DLS		**UV-vis**	
	z-average	**pdI**	**H_{max}**	**λ_{max}**
10CT	na	na	145.5	392
40CT	38.79	0.153	174.8	409
100CT	88.96	0.184	49.3	484
10PVP	na	na	175.8	391
40PVP	50.60	0.236	135.5	411
100PVP	104.4	0.137	46	490

Table 23. DLS and UV-vis results after quality control. DLS data for 10 nm-sized AgNPs were not available (na). The H_{max}values were calculated considering the AgNPs dilutions.

The effect of mouse plasma (MP) concentration on 100 and 40nm AgNPs samples: DLS results.

Except the 40PVP sample, the higher the MP content in the suspending medium, the higher was the increase in the hydrodynamic diameter, as shown in Fig. 55.

Overall, the increase in diameter of CT-coated AgNPs was found to be higher than PVP-coated ones, further confirming that AgNPs after PVP coating were stealth.

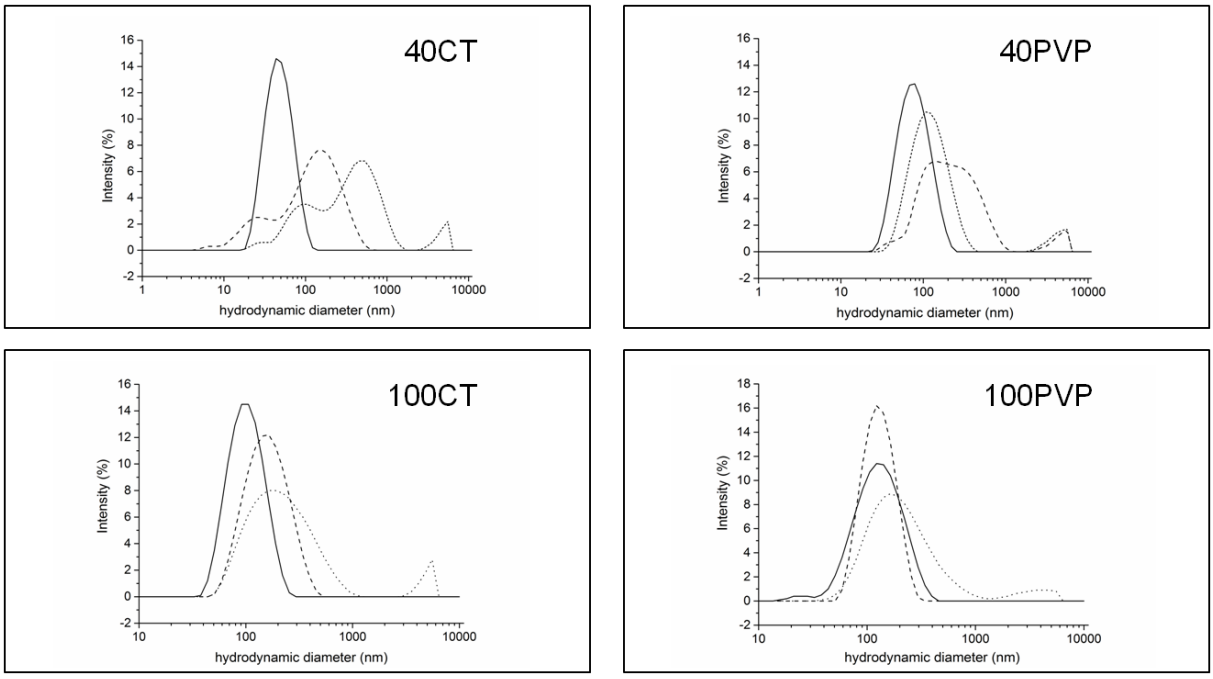

Fig. 55. Size distributions of 40 and 100 nm-sized AgNPs, coated with either CT or PVP after 24h incubation with 10% MP (dash) and 100% MP (dot). The concentration of AgNPs was 50.0 µg/mL. Controls are reported as solid line.

2. Tissue distribution and acute toxicity of silver after single intravenous administration in mice: nano-specific and size-dependent effects

Physicochemical characterization of silver nanoparticles

Commercial AgNPs with a nominal size of 10, 40 and 100 nm were tested in this study. Citrate (CT)- and polyvinylpyrrolidone (PVP)-coated AgNPs were investigated to probe the effect of surface stabilizing agents. Details provided by the manufacturer on the physic-chemical properties of the studied AgNPs are reported in Table 24 page 153. The particles were thoroughly characterized before the investigation of their toxicological effects *in vivo* and their accordance to manufacturer's specifications assessed. A rigorous characterization of the test dispersions is prerequisite to produce data that can help provide scientific answers to regulatory issues, which are impelling for a widely used nanomaterial type such as AgNPs.

Three different techniques were employed, namely Dynamic Light Scattering (DLS), UV-visible (UV-Vis) spectroscopy, and Transmission Electron Microscopy (TEM). First, the hydrodynamic diameter of the particles and their possible aggregation when suspended in the testing medium were evaluated by DLS. The results are summarized Table 25 page 154. Monomodal distributions were observed for 40 nm and 100 nm AgNPs, coated with both CT and PVP. The 10 nm AgNP-CT and 10 nm AgNP-PVP suspensions showed multimodal distributions. In particular, the peaks at 18.1 and 19.6 nm were indicative of isolated nanoparticles in 10 nm AgNP-CT and 10 nm AgNP-PVP, respectively, while larger peaks in both samples suggested the possible presence of aggregates with variable dimensions. However, these large peaks were still detected by DLS even after filtration (0.22 µm pore size), thus indicating their dynamic nature.

To further investigate the intrinsic features of the putative aggregates detected in 10 nm AgNPs, UV-vis spectroscopy measurements were performed. AgNPs exhibit a characteristic absorbance maximum in the visible range due to the surface plasmon resonance (SPR) effect[172]. Notably, optical properties of AgNPs are closely related to their morphology, therefore UV-vis spectroscopy is able to detect any change in size/shape as well as the presence of aggregates. The UV-vis results are shown in Table 25 page 154. The correspondence between the optical properties given by the

manufacturer and those measured in our laboratory appeared satisfactory; in particular, no decrease in the maximum absorbance value (H_{max}) was observed, indicating absence of aggregates. Then, full absorbance spectra of all samples were considered (Figure 56). The optical density in the 600-800 nm range, which is typical for aggregate absorption, was not detected in 10 nm AgNP-CT and 10 nm AgNP-PVP, further demonstrating that the presence of stable aggregates in these samples could be excluded[178].

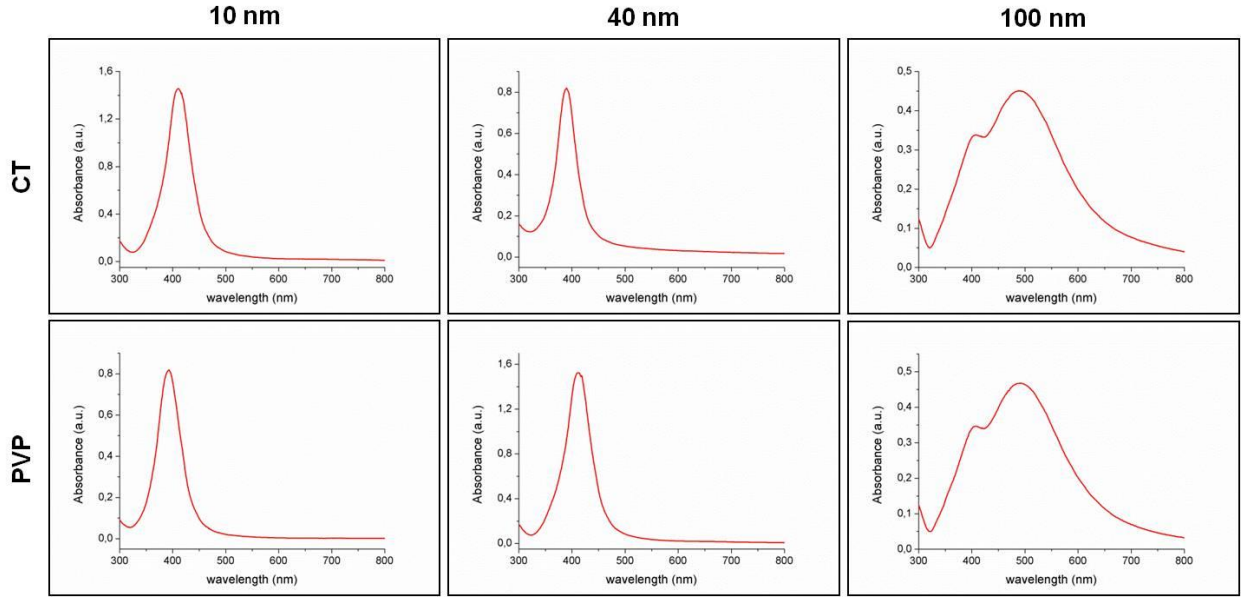

Figure 56. Particle characterization by UV-vis spectroscopy: full absorbance spectra of the tested silver nanoparticles. The optical density in the 600-800 nm range, which is typical for aggregate absorption, was not detected in any of tested AgNPs, indicating the absence of stable aggregates in these samples.

Eventually, TEM analysis was performed to assess the shape and primary size distribution of tested AgNPs. All the tested AgNPs were spherical in shape (Figure 57), and their Feret diameter distributions were in good accordance with data reported by the manufacturer ($p > 0.05$ in all cases) (Table 25 page 154).

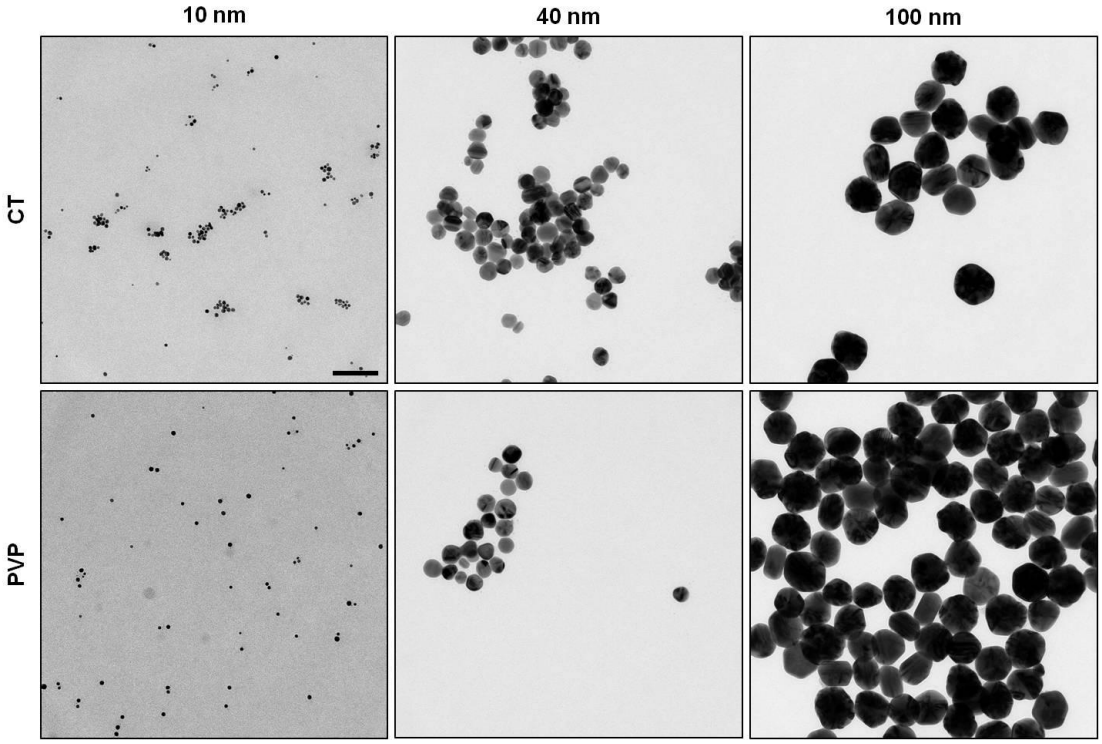

Figure 57. TEM of silver nanoparticles. Representative transmission electron micrographs of tested 10, 40, 100 nm AgNPs,CT- and PVP-coated. All purchased particles were spherical in shape, and no stable aggregates were visible (scale bar is 100 nm).

According to these analyses, both the 10 nm AgNP-CT and the 10 nm AgNP-PVP gave questionable DLS results, since peaks by far larger than 10 nm were detected. Similar findings were recently reported for AgNPs with size lower than 20 nm and 15 nm[163]. Here, the absorbance spectra clearly confirmed the absence of any stable aggregate, since neither the H_{max} decrease nor the absorbance in the 600-800 nm range were visible. TEM analysis further confirmed the absence of aggregates. Therefore, the large peaks detected in the DLS analyses of 10 nm AgNPs were ascribed to dynamic aggregates, which are unstable and do not represent a problem for *in vivo* experiments. In conclusion, the characterization by DLS, UV-vis spectroscopy, and TEM of purchased AgNPs suspensions confirmed the data certified by the manufacturer and their suitability for *in vivo* administration.

Characterization of silver nanoparticles. Suspensions of BioPure™ Silver Nanoparticles (AgNPs) of 10, 40 and 100 nm in size, coated with either citrate (CT) or polyvinylpyrrolidone (PVP), were purchased from NanoComposix (San Diego, USA). All the suspensions were supplied at a concentration of about 1.0 mg/mL. BioPure™ AgNPs were chosen because they were guaranteed to be sterile and with an endotoxin level lower or equal to 2.5 EU/mL. Before use, the CT and PVP-coated AgNPs were diluted with 2.0 mM sodium citrate (cod. W302600, Sigma-Aldrich) buffer and MilliQ water (Millipore), respectively. When necessary, samples were sonicated (Elmasonic S 30 H) for up to 30 seconds, in accordance with the manufacturer's instructions. In order to prevent contamination, measurements were run using disposable plastic cuvettes. The AgNPs were tested immediately after their delivery and *in vivo* experiments were run in the following week. In the meanwhile, the AgNPs were stored at +4°C, according to manufacturer's instructions.

Dynamic Light Scattering (DLS). The actual size of AgNPs in dispersion was measured by DLS. Measurements were performed with a Malvern Zetasizer Nano ZS90 instrument operating with a light source wavelength of 633 nm and a fixed scattering angle of 90°. All the nanoparticles were diluted 1:100 with the exception of 10 nm-sized AgNPs. Indeed, due to their small size, the 10 nm AgNPs presented increased absorption and lower scattering intensity compared to 40 nm and 100 nm AgNPs. Accordingly, the 10 nm AgNPs were diluted 1:50. All measurements were run at room temperature for at least three times.

UV-Visible (UV-Vis) Spectrophotometry. The UV-Vis spectra were acquired in the 300-800 nm range using a DU730 Beckman Coulter Spectrophotometer. All the nanoparticles were diluted 1:100 with the exception of 10 nm AgNPs, which were diluted 1:200 because of their increased UV-Vis absorbance with respect to larger nanoparticles. All measurements were run at room temperature for at least three times.

Transmission Electron Microscopy (TEM). Formvar coated copper TEM grids (cod. PE1GC300, Pelco) were pre-treated with 20 µL of poly-L-lysine 0.01% (w/v) (Sigma Aldrich) for 15 minutes. After washing twice with MilliQ water, 3 µL of AgNPs suspensions were deposited onto the grid

for 5 minutes and then rinsed with 3 µL of 2-propanol (Sigma Aldrich). According to the manufacturer's advice, 100 and 40 nm AgNPs were used at the concentration of 1.0 mg/mL, while 10 nm AgNPs were diluted up to 0.1 mg/mL before use. The grids were allowed to dry overnight at room temperature in a covered crystallizing dish. TEM (FEI Tecnai G2, Eindhoven) images were analyzed with the ImageJ software (http://imagej.nih.gov/ij/) to obtain the nanoparticles dimensional distribution. In particular, small objects due to background and overlapping nanoparticles were omitted by using proper cut-off filters and Feret diameter (intended as the larger diameter of the NP projection) was used to evaluate the size of the particles. For each sample, a minimum of about 250 nanoparticles was considered.

Table 24. Main physicochemical properties of tested AgNPs provided by the manufacturer and reported in the datasheet.

	DLS	UV-Vis		TEM					
Biopure™ Silver nanoparticle	Mean hydrodynamic diameter (nm)	λmax (nm)	Hmax (a.u.)	Diameter (mean±SD) (nm)	Variation coefficient (%)	Mass concentration (mg/ml)	Particle concentration (n° of particles/ml)	Solvent	pH of solution
10 nm AgNP-CT	na	388	164.9	8.8±1.7	19.6	1.03	$3.5*10^{14}$	2.0 mM citrate MilliQ water	7.3
10 nm AgNP-PVP	21.3	389	160.2	9.5±1.9	7.5	1.1	$2.2*10^{14}$	2.0 mM citrate MilliQ water	6.9
40 nm AgNP-CT	53.7	411	151.1	40.6±3.0	7.0	1.12	$2.7*10^{12}$	2.0 mM citrate MilliQ water	7.6
40 nm AgNP-PVP	49.3	411	148.2	40.7±4.1	20.2	1.1	$2.7*10^{12}$	2.0 mM citrate MilliQ water	6.7
100 nm AgNP-CT	99.8	495	49.2	99.4±7.0	10.0	1.0	$1.9*10^{11}$	2.0 mM citrate MilliQ water	7.3
100 nm AgNP-PVP	117.0	492	48.2	99.0±5.7	5.8	1.07	$1.9*10^{11}$	2.0 mM citrate MilliQ water	5.9

CT = sodium citrate; PVP = polyvinylpyrrolidone. na = not available (not reported in the datasheet).

Table 25. Physicochemical characterization of tested AgNPs. The main findings in AgNPs characterization are reported for each tested sample. For DLS analyses, the mean size of AgNPs is expressed in terms of hydrodynamic diameter, however this parameter is fully informative only for samples with monomodal distributions. Accordingly, the maximum intensity peaks were also reported to describe more comprehensively samples having multimodal distributions (*i.e.* 10 nm AgNP-CT and 10 nm AgNP-PVP). The pdI provides a measure of particles uniformity. For UV-Vis analyses, the maximum wavelength (λ_{max}, *i.e.* the wavelength corresponding to the highest absorbance of AgNPs) and the maximum absorbance value (H_{max}) are reported. The λ_{max} and H_{max} values were expressed in nanometer (nm) and arbitrary units (a.u.), respectively. Finally, AgNPs size distributions expressed as Feret diameter (mean ± SD, nm) and variation coefficient (%) were obtained from TEM analysis.

Biopure™ Silver nanoparticle	DLS			UV-Vis		TEM	
	Mean hydrodynamic diameter (nm)	Max intensity peaks (nm)	pdI	λ_{max} (nm)	H_{max} (a.u.)	Diameter (mean±SD, nm)	Variation coefficient (%)
10 nm AgNP-CT	np	18.1-4046	0.258	392	163.5	8.4±1.5	25.4
10 nm AgNP-PVP	np	19.6–111–4292	0.343	389	163.6	10.8±2.6	24.0
40 nm AgNP-CT	40.1	49.8	0.213	412	152.6	39.3±4.8	12.3
40 nm AgNP-PVP	51.8	67.6	0.251	410	145.7	40.3±5.6	13.9
100 nm AgNP-CT	87.6	102.9	0.148	490	45.1	107.7±10.5	9.8
100 nm AgNP-PVP	104.1	119.4	0.124	491	46.8	105.5±10.9	10.4

np = not provided for samples with multimodal distributions

3. Fill the gap in the nanomaterials legislation: determination of the partition coefficient of silver nanoparticles

Abstract

Partition coefficient (P) is a key parameter in safety assessment, being predictive for membrane permeability, bioaccumulation and biomagnification. However, to date legislation of nanomaterials has poorly considered this parameter to assess their safety and no protocols using P are reported. In general few studies are present in literature to determine P value of nanomaterials. Since silver nanoparticles (AgNPs) represent one of the most used nanomaterials in commercial products, a novel method based on shake flask principle is here presented to assess their P value. AgNPs having 100 nm in size and citrate (CT-AgNPs) or PolyVinylPyrrolidone (PVP-AgNPs) as surface coating were selected and the influence of different parameters (shaking time, pH and proteins interaction) on P evaluation was investigated.

First, after three hours shaking the partition equilibrium was reached for both CT- and PVP-AgNPs; however the water-octanol distribution was different, being the PVP-AgNPs completely moved in the organic phase, while the CT-AgNPs still remained in the aqueous one. Nevertheless this distribution was dependent on pH and ionic strength of the aqueous phase: the higher the pH the more AgNPs preferred the aqueous phase, both for CT and PVP coating. Finally, the formation on purpose of a protein corona around each single AgNPs minimized differences in phase distribution since both CT- and PVP-AgNPs were stabilized in the aqueous phase at each pH tested.

Introduction

The partition coefficient (P) is defined as the ratio of the equilibrium concentrations of a dissolved substance in a two-phase system, composed by immiscible solvents, commonly water and n-octanol[179]. Undoubtedly, P is a measure of hydrophobicity and, since several biological processes are driven by this property, P assessment is potentially predictive of materials behavior when interacting with biosystems[180,181]. For instance, P can be considered an indirect measurement of

permeability being directly correlated to passive diffusion through biological membrane by the Fick's second Law[182]. In addition, the accumulation capacity of a substance in lipids is commonly assumed to be identical to that in n-octanol[183]. This means that P can help predicting the accumulation of a determined substance in the adipose tissues but also its bioaccumulation factor in the food chain[184]. Moreover, P evaluation is fundamental in ecotoxicology, since hydrophobicity may also influence soil sorption[180,184].

As far as chemicals are concerned, P have been thoroughly studied in the nineteenth and twentieth century[185] and it is nowadays required as mandatory parameter to be reported in different legislation and guidelines from both Europe and United States, such as "Registration, Evaluation, Authorization, and Restriction of Chemicals" (REACH), "Organization for Economic co-operation and Development"(OECD), and "Toxic Substances Control Act" (TSCA). In addition, relationships between P and organic carbon content, toxicity and bioaccumulation factor have been thoroughly studied and nowadays software are available to predict chemicals fate, especially in the environment[183].

When nanomaterials (NMs) are taken into account, the importance of P is still on debate. In fact, in the OECD "Guidance manual for the testing of manufactured nanomaterials (NMs)" edited in 2009[186], P was considered mandatory as parameter when technical dossiers should be provided. In addition, reviews are available[187,188] on the importance of P as hydrophobicity index for toxicity and fate protocols, also for nano-sized materials. However, very recently the same OECD commission[189] expressed the opinion that P evaluation is irrelevant, being the test available for P assessment not suitable to investigate a distribution mechanism peculiar for NMs. The task is challenging and debated. Actually, it is well-known that NMs behave differently with respect to their bulk form[52] but strict protocols on how to evaluate NMs physical-chemical characteristics are not available yet. One of the major hurdle in this area is the lack of standardized methods[187] to assess NMs properties, including surface area, charge, size, shape, and morphology[183]. In particular, hydrophobicity assessment in NMs is one of the most tricky task because of NMs

interference in interfacial phenomena[188]. In the literature very few data are available on P assessment on NMs and the most majority were obtained with not standardized materials[187].

In answer to the call for protocol harmonization in the physical-chemical characteristics of NMs, the present work was aimed at exploring the potential of the classical shake-flask method[179] to evaluate P for NMs. Shake-flask is the preferred method in P evaluation for chemicals due to its simplicity and robustness but no evidences are available for its suitability also for NMs. In this study, attention was focused on silver nanoparticles (AgNPs). In fact, they represent the most widely commercialized NMs in industry thanks to their antiseptic activity and potential for adverse effects in humans is very high. However, very few studies are present in the literature assessing AgNPs physical-chemical properties, including P. Moreover, these studies often employed AgNPs without a complete characterization in term of size and size distribution. To overcome these limitations, commercial AgNPs (Biopure, Nanocomposix, San Diego, US) having a mean size of 100 nm and with two different coatings, namely citrate (CT) and PolyVinylPyrrolidone (PVP), were investigated. Additionally, different parameters were considered in the experimental setup, including shaking time, temperature, aqueous medium pH and ionic strength. Finally, the interaction of proteins with AgNPs to form a "protein corona" and its impact in P assessment were evaluated. Easy-to-manage techniques, such as UV-Visible spectroscopy (UV-Vis, Cary 100, Agilent) and Dynamic Light Scattering (DLS, Zetasizer NanoZS, Malvern Instruments) were used to determine AgNPs concentration and morphology, respectively.

Materials and methods

Materials

Silver Nanoparticles (AgNPs) of 100 nm in size, coated with either citrate (CT-AgNPs) or polyvinylpyrrolidone (PVP-AgNPs), were purchased from NanoComposix (San Diego, USA) and used as received. All the suspensions were provided at the concentration of 1.0 mg/mL. 1-octanol, Fetal Bovine Serum (FBS), sodium citrate, sodium chloride, potassium chloride, sodium phosphate, potassium phosphate, hydrochloric acid and sodium hydroxide were purchased from

Sigma Aldrich. MilliQ water was used in all the experiments. Experiments were run at the concentration of 15.0 µg/mL. However, since AgNPs can partially degrade in stock conditions, their nominal concentration was always assessed before starting the experiments.

Adapted shake-flask method experiments. To reproduce the shake-flask method, 500 µL of 1-octanol were added to 500 µL of aqueous AgNPs solution (15.0 µg/mL) in a glass vial. Different aqueous phases were considered. In particular, citrate 2 mM was used to set the experimental parameters, whereas Phosphate Buffer Saline (PBS) 0.1X was selected to mimic physiological conditions. By properly adding concentrated HCl or NaOH, three PBS buffer having different pH values were obtained, namely, 3.0 to mimic the gastric compartment, 5.5 for the epidermis and 8.0 for the large intestine. Samples were let under constant rotation. After the appropriate timing, the formed emulsions were left at room temperature (RT) until a complete separation of the two immiscible phases was reached. The upper organic phase was removed and the aqueous one was analyzed by both Dynamic Light Scattering and UV-Vis spectroscopy.

Dynamic Light Scattering (DLS). The hydrodynamic diameter of AgNPs in solution was measured by DLS technique. Measurements were performed with a Malvern Zetasizer ZS90 instrument operating with a light source wavelength of 633 nm and a fixed scattering angle of 90°. All the measurements were run at RT for at least three times.

UV-Vis Spectroscopy. The UV-Vis spectra were acquired in the 300-700 nm range using a Cary 100 Spectrophotometer (Agilent). All the measurements were run at RT for at least three times. AgNPs concentrations before and after the partition experiments were calculated by means of calibration curves. AgNPs were diluted in citrate 2mM at the concentrations of: 0.0 - 2.5 – 7.5 – 12.5 – 17.5 – 22.0 µg/mL. At least five curves were constructed by taking into account the maximum wavelength of absorbance, 480 nm for CT-coated and 490 nm for PVP-coated AgNPs, respectively. From a linear regression calculation, equations used for AgNPs concentration evaluation were:

Y = 0.054 x (Pearson 0.9998) for CT-coated AgNPs

Y = 0.041 x -0.002 (Pearson 0.9987) for PVP-coated AgNPs

Experiments with protein corona. In order to better mimic a biological exposition, the AgNPs were suspended in FBS at the concentration of 30.0 µg/mL and incubated at 37°C. After 24 hours, samples were purified by centrifugation (10,000g, 10 minutes, RT, thrice). The final pellets were resuspended in the appropriate aqueous medium (citrate 2 mM, PBS 0.1X pH 3, PBS 0.1X pH 5.5 and PBS 0.1X pH 8), and the nominal starting concentration of 15.0 µg/mL was restored. Protein corona formation was assessed by the increase in the hydrodynamic diameter by DLS analyses. At least three samples were prepared for each experiment.

Partition coefficient calculation. P was calculated as the logarithm of the ratio between the aqueous and the organic phase concentration, the latter one obtained as the difference between initial and final concentration in the aqueous phase[179].

Conclusions

In this study, shake-flask method was applied to determine P for commercial 100nm AgNPs, with two different coatings, citrate and PVP. In a standardized setting, with citrate 2 mM as aqueous phase, the water-octanol distribution was found to be dependent on the AgNPs coating. Being the AgNP-PVP partitioned preferentially in the organic phase, they resulted potentially more hydrophobic and toxic than the AgNP-CT. The partition experiments and the AgNPs stability were not affected by temperature but resulted strongly dependent on the aqueous phase pH. In fact, CT-AgNPs stability was higher at higher pH, also for the controls. In this context, the potential toxicity of AgNP-PVP was found to be higher at pH 3. Finally, protein corona formation was investigated. The variability in the AgNPs partitioning and the potential toxicity of both CT- and PVP-AgNPs were found to be reduced at all the tested pH. In particular, PVP-AgNPs was more hydrophilic than CT-AgNPs. Evidently, the different composition in the protein corona attributed new characteristics at the AgNPs surface.

List of publications

Data presented in this dissertation are or will be included in the following articles:

Main thesis text

Single particle optical extinction and scattering allows real time quantitative characterization of drug payload and degradation of polymeric nanoparticles

Marco Potenza, Tiziano Sanvito, Simona Argentiere, Claudia Cella, Bruno Paroli, Cristina Lenardi, Paolo Milani

Scientific reports, 2015 Dec 15;5:18228. doi: 10.1038/srep18228

Amine-modified Poly(vinyl alcohol) as a novel surfactant to modulate size and surface charge of Poly-Lactic-co-Glycolic Acid nanoparticles

Claudia Cella, Federico Martello, Serena Ghisletti, Cristina Lenardi, Paolo Milani, Simona Argentiere

Polymer International, under revision

Calcium Stearate as an effective alternative to Poly(vinyl alcohol) in Poly-Lactic-co-Glycolic Acid nanoparticles synthesis

Claudia Cella, Irini Gerges, Cristina Lenardi, Paolo Milani, Simona Argentiere

Biomacromolecules, to be submitted

Appendix 1

Embedded poly(lactide-co-glycolide) nanoparticles in a micro-pattern collagen scaffold enhanced neuronal tissue regeneration

Lucia Giampetruzzi, Laura Blasi, Marta Madaghiele, Luca Salvatore, Simona Argentiere,Claudia Cella, Alessandro Sannino

Journal of controlled release, to be submitted

Appendix 2

A Practical Approach to Assess the Fate of Isolated Silver Nanoparticles in Complex Biological Media

Simona Argentiere, Claudia Cella, Maura Cesaria, Paolo Milani, Cristina Lenardi

Journal of nanoparticles research, submitted

Tissue distribution and acute toxicity of silver after single intravenous administration in mice: nano-specific and size-dependent effects

Camilla Recordati, Marcella De Maglie, Silvia Bianchessi, Simona Argentiere, Claudia Cella, Silvana Mattiello, Francesco Cubadda, Federica Aureli, Marilena D'Amato, Andrea Raggi, Cristina Lenardi, Paolo Milani, Eugenio Scanziani

Particle and fiber toxicology, under revision

Fill the gap in the nanomaterials legislation: determination of the partition coefficient of silver nanoparticles

Claudia Cella, Simona Argentiere, Chiara Marotta, Paolo Milani, Cristina Lenardi

To be submitted

ACKNOWLEDGMENTS

“Dicono che è vero che ad ogni entusiasmo corrisponde stessa quantità di frustrazione

Dicono che è vero sì ma anche fosse vero non sarebbe giustificazione

per non farlo più, per non farlo più”

(Credits: Lorenzo Cherubini Jovanotti)

My sincere first thanks is for my post-doc Simona Argentiere. Without her scientific support, her competence, her energy, her patience and especially her friendship, nothing of what I presented in this thesis would ever been possible.

Thanks to my supervisor, professor Cristina Lenardi, for having trusted me and given me the opportunity to serenely complete my PhD course in the Advance Biomaterials Platform, Fondazione Filarete. Thanks for her guidance and her help, especially in paper writing and relationship with collaborators. Many thanks also to my internal advisor, professor Paolo Milani, for following with interest my work and my progress. I am also grateful to professor Simon Richardson (University of Greenwich), my external advisor, for his approval of my scientific work, for valuable suggestion and for allowing me to live a very nice experience in his lab, even for few days.

My grateful thanks are extended to all the scientists I met during these years and that were wonderful co-author in different papers.

First, I have to mention professor Marco Potenza, from the Physics department (University of Milan) and Tiziano Sanvito from EOS s.r.l. for the experiments related to the SPES technique. In particular, thanks to Tiziano for being so patient in explaining to me over and over again how the techniques works, for tolerantly listening my presentation and for valuable suggestions. I am also grateful to Marco and Tiziano for the big opportunity they gave me and for the exciting experience we are now living together in EOS.

For the amino-PVA synthesis, thanks to Federico Martello (Tensive s.r.l., former Advanced Biomaterial Platform) for introducing me in the polymeric synthesis word and thanks to Marco Ortenzi (Polystar) for the chemical characterization necessary to complete the relative paper.

The idea of using calcium stearate as surfactant derived from fruitful scientific discussion with Irini Gerges (Tensive s.r.l., former Advanced Biomaterial Platform).

I am grateful to Serena Ghisletti (European Institute of Oncology, IEO) for providing me macrophages for the cytotoxicity experiments, for allowing me to work in her lab and for teaching me how to deal with cells. Thanks also to Agnese Collino (European Institute of Oncology, IEO) for the nice afternoon we spent together mounting glasses.

For the microscopy characterization, I am grateful to Davide Marchesi (Imaging Platform, Fondazione Filarete) for SEM and TEM images, and to Simona Rodighiero (Imaging Platform, Fondazione Filarete) for help in confocal acquisitions.

XPS experiments were performed by Patrizia Rosa (Cimaina, University of Milan).

I want to thanks Laura Blasi and other people from University of Salento (Lecce) for the fruitful collaboration and the very nice paper we wrote together.

For the Nanotox project, special thanks to MapLab (Fondazione Filarete, under the direction of professor Scanziani), in particular many thanks to Camilla Recordati, Silvia Bianchessi and Marcella De Maglie, because working together was really a pleasure.

I am grateful also to Maura Cesaria (University of Lecce) for support in the physical interpretation of UV-Vis spectra.

Thanks to my (former) master thesis student Chiara Marotta for practically perform partitioning experiments.

Many thanks for all the other people involved in the Nanotox project.

During these years as a PhD student in the European School of Molecular Medicine, I met very nice students that was very helpful for psychological support. My thanks to Marco, Yungson, Augusto and Alexandra. Many thanks also to Francesca Fiore and Veronica Viscardi, for being so patient and so invaluable.

Many many many thanks to all the people that were part of the Advance Biomaterials Platform in Filarete: Eleonora, Chantal, Marco, Elisa, Chiara, Martino, Smbat, Laura, Federico, Alessandro, Irini, Margherita, Rossella, Erika, Valentina. Each of you, at different levels and in different ways, was really important in this adventure. We shared office, labs, coffee machine, happy hours, dinners, lunches (a lot of food actually), laughs, hysterics, science… We grew up together... and it was fun…

Special and separated thanks to Maria Vittoria, for being not only a wonderful lab mate, but also a wonderful friend. And thanks for sharing with me Florence and the CRS experience in Pieve Tesino, with Marco, Maria Flora and Olta…

As a promise, thanks to Peppa Pig (she knows why)!

Thanks to my cousin and flat mate, Emanuela, because in the last months I think it was a nightmare to live with me, and special thanks for being a great cook.

Finally, I want to thanks my family, especially my mum and dad, for allowing me to reach this result, for always trusting me and supporting my choices, for bearing with my sadness and for sharing my happiness, for having patiently wait until “I finally started to work”. For being present, always. Thanks.

My last special thanks are for my future husband Paolo. His support was fundamental to get to the end of my PhD course. He was (and is) always listening to me, if I’m talking nonsense about some crazy experiment or if I’m complaining about everything. He was wonderful, especially during the weekends when outside was so shiny, and he waited patiently that I completed my thesis writing, instead of going out for a ride in the mountains. He was wonderful when he check and double check spelling error and number of pages. He is wonderful in our everyday life. And he is my new great adventure.

References

1. Liguori, M., Solinas, G., Germano, G., Mantovani, A. & Allavena, P. Tumor-associated macrophages as incessant builders and destroyers of the cancer stroma. *Cancers (Basel).***3,** 3740–61 (2011).

2. Sica, A. & Mantovani, A. Macrophage plasticity and polarization: in vivo veritas. *J. Clin. Invest.***122,** 787–795 (2012).

3. Biswas, S. K. & Mantovani, A. Macrophage plasticity and interaction with lymphocyte subsets: cancer as a paradigm. *Nat. Immunol.***11,** 889–896 (2010).

4. Lewis, M. Tumor-Associated Macrophages, Inflammation and Pathogenesis of Hepatocellular Carcinoma. *J. Mol. Genet. Med.***08,** (2014).

5. Patel, S. K. & Janjic, J. M. Macrophage targeted theranostics as personalized nanomedicine strategies for inflammatory diseases. *Theranostics***5,** 150–172 (2015).

6. Sica, A., Schioppa, T., Mantovani, A. & Allavena, P. Tumour-associated macrophages are a distinct M2 polarised population promoting tumour progression: Potential targets of anti-cancer therapy. *Eur. J. Cancer***42,** 717–727 (2006).

7. Quail, D. F. & Joyce, J. A. Microenvironmental regulation of tumor progression and metastasis. *Nat. Med.***19,** 1423–1437 (2013).

8. Dewitte, H., Verbeke, R., Breckpot, K., De Smedt, S. C. & Lentacker, I. Nanoparticle design to induce tumor immunity and challenge the suppressive tumor microenvironment. *Nano Today***9,** 1–16 (2014).

9. Mantovani, A. *et al.* Cancer-related inflammation. *Nature***454,** 436–44 (2008).

10. Qian, B.-Z. *et al.* CCL2 recruits inflammatory monocytes to facilitate breast-tumour metastasis. *Nature***475,** 222–225 (2011).

11. Mantovani, A., Bottazzi, B., Colotta, F., Sozzani, S. & Ruco, L. The origin and function of tumor-associated macrophages. *Immunol. Today***13,** 265–270 (1992).

12. Steidl, C. *et al.* Tumor-associated macrophages and survival in classic Hodgkin's lymphoma. *N. Engl. J. Med.***362,** 875–885 (2010).

13. Chen, J. *et al.* CCL18 from tumor-associated macrophages promotes breast cancer metastasis via PITPNM3. *Cancer Cell***19,** 541–55 (2011).

14. Qian, B.-Z. & Pollard, J. W. Macrophage diversity enhances tumor progression and metastasis. *Cell***141,** 39–51 (2010).

15. De Nardo, D. G. *et al.* Leukocyte Complexity Predicts Breast Cancer Survival and Functionally Regulates Response to Chemotherapy. *Cancer Discov.***1,** 54–67 (2011).

16. De Palma, M. & Lewis, C. E. Macrophage Regulation of Tumor Responses to Anticancer Therapies. *Cancer Cell***23,** 277–286 (2013).

17. D'Incalci, M. & Galmarini, C. M. A review of trabectedin (ET-743): a unique mechanism of action. *Mol. Cancer Ther.***9,** 2157–2163 (2010).

18. Luo, Y. *et al.* Targeting tumor-associated macrophages as a novel strategy against breast cancer. **116,** (2006).

19. Condeelis, J. & Pollard, J. W. Macrophages: Obligate Partners for Tumor Cell Migration, Invasion, and Metastasis. *Cell***124,** 263–266 (2006).

20. Grosso, F. *et al.* Efficacy of trabectedin (ecteinascidin-743) in advanced pretreated myxoid liposarcomas: a retrospective study. *Lancet. Oncol.***8,** 595–602 (2007).

21. Sessa, C. Trabectedin for Women With Ovarian Carcinoma After Treatment With Platinum and Taxanes Fails. *J. Clin. Oncol.***23,** 1867–1874 (2005).

22. Sessa, C. *et al.* Phase I clinical and pharmacokinetic study of trabectedin and doxorubicin in advanced soft tissue sarcoma and breast cancer. *Eur. J. Cancer***45,** 1153–61 (2009).

23. Guest, J. F., Panca, M., Sladkevicius, E., Gough, N. & Linch, M. Cost Effectiveness of First-Line Treatment with Doxorubicin / Ifosfamide Compared to Trabectedin Monotherapy in the Management of Advanced Soft Tissue Sarcoma in Italy , Spain , and Sweden. *Sarcoma***2013,** (2013).

24. Goel, A., Kunnumakkara, A. B. & Aggarwal, B. B. Curcumin as 'Curecumin': From kitchen to clinic. *Biochem. Pharmacol.***75,** 787–809 (2008).

25. Jagetia, G. C. & Aggarwal, B. B. 'Spicing Up' of the Immune System by Curcumin. *J. Clin. Immunol.***27,** 19–35 (2007).

26. Holy, J. M. Curcumin disrupts mitotic spindle structure and induces micronucleation in MCF-7 breast cancer cells. *Mutat. Res. Toxicol. Environ. Mutagen.***518,** 71–84 (2002).

27. Aggarwal, B. B. & Harikumar, K. B. Potential therapeutic effects of curcumin, the anti-inflammatory agent, against neurodegenerative, cardiovascular, pulmonary, metabolic, autoimmune and neoplastic diseases. *Int. J. Biochem. Cell Biol.***41,** 40–59 (2009).

28. Singh, S. & Aggarwal, B. B. Activation of transcription factor NF-kappa B is suppressed by curcumin (diferuloylmethane) [corrected]. *J. Biol. Chem.***270,** 24995–25000 (1995).

29. Shishodia, S., Chaturvedi, M. M. & Aggarwal, B. B. Role of curcumin in cancer therapy. *Curr. Probl. Cancer***31,** 243–305 (2007).

30. Tu, S. P. *et al.* Curcumin Induces the Differentiation of Myeloid-Derived Suppressor Cells and Inhibits Their Interaction with Cancer Cells and Related Tumor Growth. *Cancer Prev. Res.***5,** 205–215 (2012).

31. Brouet, I. & Ohshima, H. 1-s2.0-S0006291X85710765-main.pdf. *Biochem. Biophys. Res. Commun.***206,** 533–540 (1995).

32. Aggarwal, B. B., Kumar, A. & Bharti, A. C. Anticancer Potential of Curcumin Preclinical and Clinical Studies. *Anticancer Res.***23,** 363–398 (2003).

33. Fire, A. *et al.* Potent and specific genetic interference by double-stranded RNA in Caenorhabditis elegans. *Nature***391,** 806–811 (1998).

34. Carthew, Richard W. and Sontheimer, E. J. Origins and Mechanisms of miRNAs and siRNAs. *Cell***136,** 642–655 (2009).

35. Pecot, C. V., Calin, G. A., Coleman, R. L., Lopez-Berestein, G. & Sood, A. K. RNA interference in the clinic: challenges and future directions. *Nat. Rev. Cancer***11,** 59–67 (2011).

36. Hannon, G. J. & Rossi, J. J. Unlocking the potential of the human genome with RNA interference. *Group***431,** (2004).

37. Meister, G. & Tuschl, T. Mechanisms of gene silencing by double-stranded RNA. *Nature***431,** 343–349 (2004).

38. Martinez, J., Patkaniowska, A., Urlaub, H., Lührmann, R. & Tuschl, T. Single-stranded antisense siRNAs guide target RNA cleavage in RNAi. *Cell***110,** 563–574 (2002).

39. Gottesman, M. M., Fojo, T. & Bates, S. E. Multidrug resistance in cancer: role of ATP-dependent transporters. *Nat Rev Cancer***2,** 48–58 (2002).

40. Wang, Y. *et al.* A novel multiple drug release system in vitro based on adjusting swelling core of emulsion electrospun nanofibers with core–sheath structure. *Mater. Sci. Eng. C***44,** 109–116 (2014).

41. Kolishetti, N. *et al.* Engineering of self-assembled nanoparticle platform for precisely controlled combination drug therapy. *Proc. Natl. Acad. Sci.***107,** 17939–17944 (2010).

42. Anand, P., Kunnumakkara, A. B., Newman, R. A. & Aggarwal, B. B. reviews Bioavailability of Curcumin : Problems and Promises. *Mol. Pharm.***4,** 807–818 (2007).

43. Sharma, R. A., Gescher, A. J. & Steward, W. P. Curcumin: The story so far. *Eur. J. Cancer***41,** 1955–1968 (2005).

44. Whitehead, K. a, Langer, R. & Anderson, D. G. Knocking down barriers: advances in siRNA delivery. *Nat. Rev. Drug Discov.***8,** 129–138 (2009).

45. Nielsen, C., Kjems, J., Sørensen, K. R., Engelholm, L. H. & Behrendt, N. Advances in targeted delivery of small interfering RNA using simple bioconjugates. *Expert Opin. Drug Deliv.***11,** 791–822 (2014).

46. Devalapally, H., Chakilam, A. & Amiji, M. Role of Nanotechnology in Pharmaceutical Product Development. *J. Pharm. Sci.***96,** 2547–2565 (1997).

47. Krebs, M. D. & Alsberg, E. Localized, targeted, and sustained siRNA delivery. *Chem. - A Eur. J.***17,** 3054–3062 (2011).

48. Nguyen, J. & Szoka, F. C. Nucleic acid delivery: The missing pieces of the puzzle? *Acc. Chem. Res.***45,** 1153–1162 (2012).

49. Gupta, B., Levchenko, T. S. & Torchilin, V. P. Intracellular delivery of large molecules and small particles by cell-penetrating proteins and peptides. *Adv. Drug Deliv. Rev.***57,** 637–651 (2005).

50. Rossi, M. *et al.* Scientific basis of nanotechnology, implications for the food sector and future trends. *Trends Food Sci. Technol.***40,** 127–148 (2014).

51. Riehemann, K. *et al.* Nanomedicine--challenge and perspectives. *Angew. Chem. Int. Ed. Engl.***48,** 872–97 (2009).

52. Roduner, E. Size matters: why nanomaterials are different. *Chem. Soc. Rev.***35,** 583–592 (2006).

53. Gao, W., Liu, W., Christensen, T., Zalutsky, M. R. & Chilkoti, A. In situ growth of a PEG-like polymer from the C terminus of an intein fusion protein improves pharmacokinetics and tumor accumulation. *Proc. Natl. Acad. Sci. U. S. A.***107,** 16432–7 (2010).

54. Schellenberger, V. *et al.* A recombinant polypeptide extends the in vivo half-life of peptides and proteins in a tunable manner. *Nat. Biotechnol.***27,** 1186–1190 (2009).

55. Jia, L. NIH Public Access. **1,** 237–243 (2009).

56. Zhen, Z. *et al.* Tumor vasculature targeted photodynamic therapy for enhanced delivery of nanoparticles. *ACS Nano***8,** 6004–6013 (2014).

57. Bae, K. H., Chung, H. J. & Park, T. G. Nanomaterials for cancer therapy and imaging. *Mol. Cells***31,** 295–302 (2011).

58. Peters, D. *et al.* Targeting atherosclerosis by using modular, multifunctional micelles. *Proc. Natl. Acad. Sci. U. S. A.***106,** 9815–9819 (2009).

59. Prapainop, K., Witter, D. P. & Wentworth, P. A chemical approach for cell-specific targeting of nanomaterials: small-molecule-initiated misfolding of nanoparticle corona proteins. *J. Am. Chem. Soc.***134,** 4100–3 (2012).

60. Weissleder, R., Kelly, K., Sun, E. Y., Shtatland, T. & Josephson, L. Cell-specific targeting of nanoparticles by multivalent attachment of small molecules. *Nat. Biotechnol.***23,** 1418–1423 (2005).

61. Davis, M. E. *et al.* Evidence of RNAi in humans from systemically administered siRNA via targeted nanoparticles. *Nature***464,** 1067–1070 (2010).

62. Hubbel, J. A. & Chikoti, A. Nanomaterials for drug delivery. *Science (80-.).***337,** 303–305 (2012).

63. Singh, R. & Lillard, J. W. Nanoparticle-based targeted drug delivery. *Exp. Mol. Pathol.***86,** 215–223 (2009).

64. Uhrich, K. E., Cannizzaro, S. M., Langer, R. S. & Shakesheff, K. M. Polymeric systems for controlled drug release. *Chem. Rev.***99,** 3181–98 (1999).

65. Desai, M. P., Labhasetwar, V., Walter, E., Levy, R. J. & Amidon, G. L. The mechanism of uptake of biodegradable microparticles in Caco-2 cells is size dependent. *Pharmaceutical Research***14,** 1568–1573 (1997).

66. Panyam, J., Sahoo, S. K., Prabha, S., Bargar, T. & Labhasetwar, V. Fluorescence and electron microscopy probes for cellular and tissue uptake of poly(d,l-lactide-co-glycolide) nanoparticles. *Int. J. Pharm.***262,** 1–11 (2003).

67. Panyam, J. & Labhasetwar, V. Biodegradable nanoparticles for drug and gene delivery to cells and tissue. *Adv. Drug Deliv. Rev.***55,** 329–347 (2003).

68. Mahapatro, A. & Singh, D. K. Biodegradable nanoparticles are excellent vehicle for site directed in-vivo delivery of drugs and vaccines. *J. Nanobiotechnology***9,** 55 (2011).

69. Ai, H., Jones, S. a & Lvov, Y. M. Biomedical applications of electrostatic layer-by-layer nano-assembly of polymers, enzymes, and nanoparticles. *Cell Biochem. Biophys.***39,** 23–43 (2003).

70. Jin, H., Huang, W., Zhu, X., Zhou, Y. & Yan, D. Biocompatible or biodegradable hyperbranched polymers: from self-assembly to cytomimetic applications. *Chem. Soc. Rev.***41,** 5986 (2012).

71. Brigger, I., Dubernet, C. & Couvreur, P. Nanoparticles in cancer therapy and diagnosis. *Adv. Drug Deliv. Rev.***54,** 631–651 (2002).

72. Sahoo, S. K. & Labhasetwar, V. Nanotech approaches to drug delivery and imaging. *Drug Discov. Today***8,** 1112–1120 (2003).

73. Rao, J. P. & Geckeler, K. E. Polymer nanoparticles: Preparation techniques and size-control parameters. *Prog. Polym. Sci.***36,** 887–913 (2011).

74. Lockman, P. R., Mumper, R. J., Khan, M. a & Allen, D. D. Nanoparticle technology for drug delivery across the blood-brain barrier. *Drug Dev. Ind. Pharm.***28,** 1–13 (2002).

75. Pinto Reis, C., Neufeld, R. J., Ribeiro, A. J. & Veiga, F. Nanoencapsulation I. Methods for preparation of drug-loaded polymeric nanoparticles. *Nanomedicine Nanotechnology, Biol. Med.***2,** 8–21 (2006).

76. Safra, T. *et al.* Original article patients reaching or exceeding cumulative doses of 500 mg / m 2. *Ann. Intern. Med.* 1029–1033 (2000).

77. Heidel, J. D. & Davis, M. E. Clinical developments in nanotechnology for cancer therapy. *Pharm. Res.***28,** 187–99 (2011).

78. Dinarvand, R., Sepehri, N., Manoochehri, S., Rouhani, H. & Atyabi, F. Polylactide-co-glycolide nanoparticles for controlled delivery of anticancer agents. *Int. J. Nanomedicine***6,** 877–895 (2011).

79. Acharya, S. & Sahoo, S. K. PLGA nanoparticles containing various anticancer agents and tumour delivery by EPR effect. *Adv. Drug Deliv. Rev.***63,** 170–183 (2011).

80. Langer, R. & Tirrell, D. a. Designing materials for biology and medicine. *Nature***428,** 487–492 (2004).

81. Crespy, D. & Landfester, K. Anionic Polymerization of e-Caprolactam in Miniemulsion: Synthesis and Characterization of Polyamide-6 Nanoparticles. *Macromolecules***38,** 6882–6887 (2005).

82. General, S. & Thünemann, A. F. pH-sensitive nanoparticles of poly(amino acid) dodecanoate complexes. *Int. J. Pharm.***230,** 11–24 (2001).

83. Lee, J., Lee, S. J., Choi, J. Y., Yoo, J. Y. & Ahn, C. H. Amphiphilic amino acid copolymers as stabilizers for the preparation of nanocrystal dispersion. *Eur. J. Pharm. Sci.***24,** 441–449 (2005).

84. Simeonova, M., Velichkova, R., Ivanova, G., Enchev, V. & Abrahams, I. Poly(butylcyanoacrylate) nanoparticles for topical delivery of 5-fluorouracil. *Int. J. Pharm.***263,** 133–140 (2003).

85. Huang, C. Y. & Lee, Y. Der. Core-shell type of nanoparticles composed of poly[(n-butyl cyanoacrylate)-co-(2-octyl cyanoacrylate)] copolymers for drug delivery application: Synthesis, characterization and in vitro degradation. *Int. J. Pharm.***325,** 132–139 (2006).

86. Anderson, J. M. & Shive, M. S. Biodegradation and biocompatibility of PLA and PLGA microspheres. *Adv. Drug Deliv. Rev.***64,** 72–82 (2012).

87. Jain, R. a. The manufacturing techniques of various drug loaded biodegradable poly(lactide-co-glycolide) (PLGA) devices. *Biomaterials***21,** 2475–2490 (2000).

88. Heller, J., Barr, J., Ng, S. Y., Abdellauoi, K. S. & Gurny, R. Poly(ortho esters): Synthesis, characterization, properties and uses. *Adv. Drug Deliv. Rev.***54,** 1015–1039 (2002).

89. Zanetti-Ramos, B. G. *et al.*Polyurethane nanoparticles from a natural polyol via miniemulsion technique. *Polymer (Guildf).***47,** 8080–8087 (2006).

90. Bouchemal, K. *et al.* Synthesis and characterization of polyurethane and poly(ether urethane) nanocapsules using a new technique of interfacial polycondensation combined to spontaneous emulsification. *Int. J. Pharm.***269,** 89–100 (2004).

91. Sun, H., Scharff-Poulsen, A. M., Gu, H. & Almdal, K. Synthesis and characterization of ratiometric, pH sensing nanoparticles with covalently attached fluorescent dyes. *Chem. Mater.***18,** 3381 (2006).

92. Chaw, C. S. *et al.* Thermally responsive core-shell nanoparticles self-assembled from cholesteryl end-capped and grafted polyacrylamides: Drug incorporation and in vitro release. *Biomaterials***25,** 4297–4308 (2004).

93. Makadia, H. K. & Siegel, S. J. Poly Lactic-co-Glycolic Acid (PLGA) as Biodegradable Controlled Drug Delivery Carrier. *Polymers (Basel).***3,** 1377–1397 (2011).

94. Danhier, F. *et al.* PLGA-based nanoparticles: An overview of biomedical applications. *J. Control. Release***161,** 505–522 (2012).

95. Wacker, M. Nanocarriers for intravenous injection--the long hard road to the market. *Int. J. Pharm.***457,** 50–62 (2013).

96. Prokop, A. & Davidson, J. M. Nanovehicular intracellular delivery systems. *J. Pharm. Sci.***97,** 3518–3590 (2008).

97. Hans, M. L. & Lowman, A. M. Biodegradable nanoparticles for drug delivery and targeting. *Curr. Opin. Solid State Mater. Sci.***6,** 319–327 (2002).

98. Zhang, H., Cui, W., Bei, J. & Wang, S. Preparation of poly(lactide-co-glycolide-co-caprolactone) nanoparticles and their degradation behaviour in aqueous solution. *Polym. Degrad. Stab.***91,** 1929–1936 (2006).

99. Verma, A. & Stellacci, F. Effect of surface properties on nanoparticle-cell interactions. *Small***6,** 12–21 (2010).

100. Lundqvist, M. *et al.* Nanoparticle size and surface properties determine the protein corona with possible implications for biological impacts. *Proc. Natl. Acad. Sci. U. S. A.***105,** 14265–14270 (2008).

101. Walczyk, D., Bombelli, F. B., Monopoli, M. P., Lynch, I. & Dawson, K. a. What the cell 'sees' in bionanoscience. *J. Am. Chem. Soc.***132,** 5761–5768 (2010).

102. Treuel, L., Jiang, X. & Nienhaus, G. U. New views on cellular uptake and trafficking of manufactured nanoparticles New views on cellular uptake and trafficking of manufactured nanoparticles. (2013).

103. Hansiri, G. A. C., Yons, R. O. T. L., Atel, M. A. V. P. & Em, S. T. L. H. Effect of Surface Charge on the Stability of Oil / Water Emulsions during Steam Sterilization. *J. Pharm. Sci.***88,** 3–7 (1999).

104. Feng, S. S. & Huang, G. Effects of emulsifiers on the controlled release of paclitaxel (Taxol®) from nanospheres of biodegradable polymers. *J. Control. Release***71,** 53–69 (2001).

105. Ravi Kumar, M. N. V, Bakowsky, U. & Lehr, C. M. Preparation and characterization of cationic PLGA nanospheres as DNA carriers. *Biomaterials***25,** 1771–1777 (2004).

106. Duncan, R. & Richardson, S. C. W. Endocytosis and intracellular trafficking as gateways for nanomedicine delivery: Opportunities and challenges. *Mol. Pharm.***9,** 2380–2402 (2012).

107. Martens, T. F., Remaut, K., Demeester, J., De Smedt, S. C. & Braeckmans, K. Intracellular delivery of nanomaterials: How to catch endosomal escape in the act. *Nano Today***9,** 344–364 (2014).

108. Astete, C. E. & Sabliov, C. M. Synthesis and characterization of PLGA nanoparticles. *J. Biomater. Sci. Polym. Ed.***17,** 247–289 (2006).

109. Li, Y. P. *et al.*PEGylated PLGA nanoparticles as protein carriers: Synthesis, preparation and biodistribution in rats. *J. Control. Release***71,** 203–211 (2001).

110. Jain, A. K., Swarnakar, N. K., Godugu, C., Singh, R. P. & Jain, S. The effect of the oral administration of polymeric nanoparticles on the efficacy and toxicity of tamoxifen. *Biomaterials***32,** 503–515 (2011).

111. Tsai, Y. M., Chien, C. F., Lin, L. C. & Tsai, T. H. Curcumin and its nano-formulation: The kinetics of tissue distribution and blood-brain barrier penetration. *Int. J. Pharm.***416,** 331–338 (2011).

112. Feczkó, T., Tóth, J. & Gyenis, J. Comparison of the preparation of PLGA-BSA nano- and microparticles by PVA, poloxamer and PVP. *Colloids Surfaces A Physicochem. Eng. Asp.***319,** 188–195 (2008).

113. Zambaux, M. F. *et al.* Influence of experimental parameters on the characteristics of poly(lactic acid) nanoparticles prepared by a double emulsion method. *J. Control. Release***50,** 31–40 (1998).

114. Shakesheff, K. M., Evora, C., Soriano, I. & Anger, R. O. L. The Adsorption of Poly (vinyl alcohol) to Biodegradable Microparticles Studied by X-Ray Photoelectron Spectroscopy (XPS). *J. Colloid Interface Sci.***547,** 538–547 (1997).

115. Sahoo, S. K., Panyam, J., Prabha, S. & Labhasetwar, V. Residual polyvinyl alcohol associated with poly (,-lactide-co-glycolide) nanoparticles affects their physical properties and cellular uptake. *J. Control. Release***82,** 105–114 (2002).

116. Peetla, C. & Labhasetwar, V. Effect of molecular structure of cationic surfactants on biophysical interactions of surfactant-modified nanoparticles with a model membrane and cellular uptake. *Langmuir***25,** 2369–2377 (2009).

117. Panyam, J., Zhou, W.-Z., Prabha, S., Sahoo, S. K. & Labhasetwar, V. Rapid endo-lysosomal escape of poly(DL-lactide-co-glycolide) nanoparticles: implications for drug and gene delivery. *FASEB J.***16,** 1217–1226 (2002).

118. Nguyen, J., Steele, T. W. J., Merkel, O., Reul, R. & Kissel, T. Fast degrading polyesters as siRNA nano-carriers for pulmonary gene therapy. *J. Control. Release***132,** 243–251 (2008).

119. Wittmar, M., Unger, F. & Kissel, T. Biodegradable brushlike branched polyesters containing a charge-modified poly (vinyl alcohol) backbone as a platform for drug delivery systems: Synthesis and characterization. *Macromolecules***39,** 1417–1424 (2006).

120. Ortega, R. a *et al.* Biocompatible mannosylated endosomal-escape nanoparticles enhance selective delivery of short nucleotide sequences to tumor associated macrophages. *Nanoscale* 500–510 (2015). doi:10.1039/C4NR03962A

121. Yu, S. S. *et al.* Macrophage-specific RNA interference targeting via 'click', mannosylated polymeric micelles. *Mol. Pharm.***10,** 975–987 (2013).

122. Menon, J. U. *et al.*Effects of surfactants on the properties of PLGA nanoparticles. *J. Biomed. Mater. Res. - Part A***100 A,** 1998–2005 (2012).

123. Richardson, S. Potential of low molecular mass chitosan as a DNA delivery system: biocompatibility, body distribution and ability to complex and protect DNA. *Int. J. Pharm.***178,** 231–243 (1999).

124. Caracciolo, G. *et al.* Stealth Effect of Biomolecular Corona on Nanoparticle Uptake by Immune Cells. *Langmuir***31,** 10764–10773 (2015).

125. Caracciolo, G. Liposome-protein corona in a physiological environment: Challenges and opportunities for targeted delivery of nanomedicines. *Nanomedicine***11,** 543–557 (2015).

126. Allavena, P. *et al.* Engagement of the Mannose Receptor by Tumoral Mucins Activates an Immune Suppressive Phenotype in Human Tumor-Associated Macrophages. *Clin. Dev. Immunol.***2010,** 1–10 (2010).

127. East, L. & Isacke, C. M. The mannose receptor family. *Biochim. Biophys. Acta***1572,** 364–386 (2002).

128. Jain, A. *et al.* Mannosylated solid lipid nanoparticles as vectors for site-specific delivery of an anti-cancer drug. *J. Control. Release***148,** 359–367 (2010).

129. Chereddy, K. K. *et al.* Combined effect of PLGA and curcumin on wound healing activity. *J. Control. Release***171,** 208–15 (2013).

130. Verderio, P., Bonetti, P., Colombo, M., Pandolfi, L. & Prosperi, D. Intracellular drug release from curcumin-loaded PLGA nanoparticles induces G2/M block in breast cancer cells. *Biomacromolecules***14,** 672–682 (2013).

131. Das, M. & Sahoo, S. K. Folate decorated dual drug loaded nanoparticle: role of curcumin in enhancing therapeutic potential of nutlin-3a by reversing multidrug resistance. *PLoS One***7,** e32920 (2012).

132. Willig, K. I., Keller, J., Bossi, M. & Hell, S. W. STED microscopy resolves nanoparticle assemblies. *New J. Phys.***8,** 106–106 (2006).

133. Potenza, M. A. C., Sanvito, T. & Pullia, A. Accurate sizing of ceria oxide nanoparticles in slurries by the analysis of the optical forward-scattered field. *J. Nanoparticle Res.***17,** 110 (2015).

134. Potenza, M. A. C., Sabareesh, K. P. V., Carpineti, M., Alaimo, M. D. & Giglio, M. How to Measure the Optical Thickness of Scattering Particles from the Phase Delay of Scattered Waves: Application to Turbid Samples. *Phys. Rev. Lett.***105,** 193901 (2010).

135. Potenza, M. & Milani, P. Free nanoparticle characterization by optical scattered field analysis: opportunities and perspectives. *J. Nanoparticle Res.***16,** 2680 (2014).

136. D'Souza, S. S. & DeLuca, P. P. Methods to Assess in Vitro Drug Release from Injectable Polymeric Particulate Systems. *Pharm. Res.***23,** 460–474 (2006).

137. link fda. at <http://www.accessdata.fda.gov/scripts/cdrh/cfdocs/cfcfr/CFRSearch.cfm?fr=173.228>

138. Alfonsi, K. *et al.* Green chemistry tools to influence a medicinal chemistry and research chemistry based organisation. *Green Chem.***10,** 31–36 (2008).

139. Meng, F. T., Ma, G. H., Qiu, W. & Su, Z. G. W/O/W double emulsion technique using ethyl acetate as organic solvent: Effects of its diffusion rate on the characteristics of microparticles. *J. Control. Release***91,** 407–416 (2003).

140. Clariant tecnical report on Mowiol(R). *Clariant*.

141. Nafee, N., Taetz, S., Schneider, M., Schaefer, U. F. & Lehr, C. M. Chitosan-coated PLGA nanoparticles for DNA/RNA delivery: effect of the formulation parameters on complexation and transfection of antisense oligonucleotides. *Nanomedicine Nanotechnology, Biol. Med.***3,** 173–183 (2007).

142. Mainardes, R. M. & Evangelista, R. C. PLGA nanoparticles containing praziquantel: Effect of formulation variables on size distribution. *Int. J. Pharm.***290,** 137–144 (2005).

143. Song, X. *et al.* PLGA nanoparticles simultaneously loaded with vincristine sulfate and verapamil hydrochloride: Systematic study of particle size and drug entrapment efficiency. *Int. J. Pharm.***350,** 320–329 (2008).

144. Vandervoort, J. & Ludwig, A. Biocompatible stabilizers in the preparation of PLGA\nnanoparticles: a factorial design study. *Int. J. Pharm.***238,** 77–92 (2002).

145. ABDELWAHED, W., DEGOBERT, G., STAINMESSE, S. & FESSI, H. Freeze-drying of nanoparticles: Formulation, process and storage considerations☆. *Adv. Drug Deliv. Rev.***58,** 1688–1713 (2006).

146. Mirshafiee, V., Mahmoudi, M., Lou, K., Cheng, J. & Kraft, M. L. Protein corona significantly reduces active targeting yield. *Chem. Commun.***49,** 2557 (2013).

147. Tu, F. & Lee, D. Controlling the stability and size of double-emulsion-templated poly(lactic-co-glycolic) acid microcapsules. *Langmuir***28,** 9944–52 (2012).

148. Chen, X. & Schluesener, H. J. Nanosilver: A nanoproduct in medical application. *Toxicol. Lett.***176,** 1–12 (2008).

149. Edwards-Jones, V. The benefits of silver in hygiene, personal care and healthcare. *Lett. Appl. Microbiol.***49,** 147–152 (2009).

150. MacCuspie, R. I. Colloidal stability of silver nanoparticles in biologically relevant conditions. *J. Nanoparticle Res.***13,** 2893–2908 (2011).

151. Wijnhoven, S. W. P. *et al.* Nano-silver – a review of available data and knowledge gaps in human and environmental risk assessment. *Nanotoxicology***3,** 109–138 (2009).

152. Liu, J., Sonshine, D. a., Shervani, S. & Hurt, R. H. Controlled release of biologically active silver from nanosilver surfaces. *ACS Nano***4,** 6903–6913 (2010).

153. Liu, J., Wang, Z., Liu, F. D., Kane, A. B. & Hurt, R. H. Chemical transformations of nanosilver in biological environments. *ACS Nano***6,** 9887–9899 (2012).

154. Elsaesser, A. & Howard, C. V. Toxicology of nanoparticles. *Adv. Drug Deliv. Rev.***64,** 129–137 (2012).

155. Ahamed, M., AlSalhi, M. S. & Siddiqui, M. K. J. Silver nanoparticle applications and human health. *Clin. Chim. Acta***411,** 1841–1848 (2010).

156. Mahmoudi, M. *et al.* The Protein Corona Mediates the Impact of Nanomaterials and Slows Amyloid Beta Fibrillation. *ChemBioChem***14,** 568–572 (2013).

157. Loza, K. *et al.* The dissolution and biological effects of silver nanoparticles in biological media. *J. Mater. Chem. B***2,** 1634 (2014).

158. Reidy, B., Haase, A., Luch, A., Dawson, K. & Lynch, I. Mechanisms of Silver Nanoparticle Release, Transformation and Toxicity: A Critical Review of Current Knowledge and Recommendations for Future Studies and Applications. *Materials (Basel).***6,** 2295–2350 (2013).

159. Stebounova, L. V., Guio, E. & Grassian, V. H. Silver nanoparticles in simulated biological media: a study of aggregation, sedimentation, and dissolution. *J. Nanoparticle Res.***13,** 233–244 (2011).

160. Tiede, K. *et al.* Detection and characterization of engineered nanoparticles in food and the environment. *Food Addit. Contam. Part A***25,** 795–821 (2008).

161. Casals, E., Pfaller, T., Duschl, A., Oostingh, G. J. & Puntes, V. Time evolution of the nanoparticle protein corona. *ACS Nano***4,** 3623–3632 (2010).

162. Tenzer, S. *et al.* Nanoparticle size is a critical physicochemical determinant of the human blood plasma corona: A comprehensive quantitative proteomic analysis. *ACS Nano***5,** 7155–7167 (2011).

163. Van Der Zande, M. *et al.* Distribution, elimination, and toxicity of silver nanoparticles and silver ions in rats after 28-day oral exposure. *ACS Nano***6,** 7427–7442 (2012).

164. Murdock, R. C., Braydich-Stolle, L., Schrand, a. M., Schlager, J. J. & Hussain, S. M. Characterization of Nanomaterial Dispersion in Solution Prior to In Vitro Exposure Using Dynamic Light Scattering Technique. *Toxicol. Sci.***101,** 239–253 (2008).

165. Treuel, L. *et al.* Physicochemical characterization of nanoparticles and their behavior in the biological environment. *Phys. Chem. Chem. Phys.***16,** 15053–67 (2014).

166. Kato, H. *et al.* Reliable size determination of nanoparticles using dynamic light scattering method for in vitro toxicology assessment. *Toxicol. Vitr.***23,** 927–934 (2009).

167. Montes-Burgos, I. *et al.* Characterisation of nanoparticle size and state prior to nanotoxicological studies. *J. Nanoparticle Res.***12,** 47–53 (2010).

168. Poda A, R. Characterization of silver nanoparticles usingf low-field flow fractionation interfaced to inductively coupled plasma mass spectrometry. *J. Chromatogr. A* (2010). doi:10.1016/j.chroma.2010.12.076

169. Kammer, F. Von Der, Legros, S., Hofmann, T., Larsen, E. H. & Loeschner, K. Separation and characterization of nanoparticles in complex food and environmental samples by field-flow fractionation. *TrAC Trends Anal. Chem.***30,** 425–436 (2011).

170. Dawson, K. a., Anguissola, S. & Lynch, I. characterisation in nanosafety assessment: funded transnational access via the QNano research infrastructure. *Nanotoxicology***7,** 1–4 (2012).

171. Hagendorfer, H. *et al.* Characterization of Silver Nanoparticle Products Using Asymmetric Flow Field Flow Fractionation with a Multidetector Approach − a Comparison to Transmission Electron Microscopy and Batch Dynamic Light Scattering. (2012).

172. Kelly, K. L. *et al.* The Optical Properties of Metal Nanoparticles: The Influence of Size, Shape, and Dielectric Environment. *J. Phys. Chem. B***107,** 668–677 (2003).

173. Priya Prakash Karmali, D. S. Interactions of nanoparticle with plasma proteins: implication on clearance and toxicity of drug delivery systems. *Expert Opin. Drug Deliv.***8,** 343–357 (2011).

174. Zhang, Y. *et al.* Zeta potential: A surface electrical characteristic to probe the interaction of nanoparticles with normal and cancer human breast epithelial cells. *Biomed. Microdevices***10,** 321–328 (2008).

175. Tolaymat, T. M. *et al.* An evidence-based environmental perspective of manufactured silver nanoparticle in syntheses and applications: A systematic review and critical appraisal of peer-reviewed scientific papers. *Sci. Total Environ.***408,** 999–1006 (2010).

176. Gebauer, J. S. *et al.* Impact of the nanoparticle-protein corona on colloidal stability and protein structure. *Langmuir***28,** 9673–9 (2012).

177. Lopez-Serrano, A., Olivas, R. M., Landaluze, J. S. & Camara, C. Nanoparticles: a global vision. Characterization, separation, and quantification methods. Potential environmental and health impact. *Anal. Methods***6,** 38–56 (2014).

178. Izquierdo-Lorenzo, I. *et al.* Linking Ag nanoparticles by aliphatic dithiols: A study of the aggregation and formation of interparticle hot spots. *J. Phys. Chem. C***117,** 16203–16212 (2013).

179. Oecd. OECD guideline for the testing of chemicals: partition coefficient (n-octanol/water): share flask method. *Guidance***107,** 1–4 (1995).

180. Hermens, J. L. M., de Bruijn, J. H. M. & Brooke, D. N. The octanol-water partition coefficient: strengths and limitations. *Environ. Toxicol. Chem.***32,** 732–3 (2013).

181. Xiao, Y. & Wiesner, M. R. Characterization of surface hydrophobicity of engineered nanoparticles. *J. Hazard. Mater.* (2012). doi:10.1016/j.jhazmat.2012.02.043

182. Lodish, H. *et al.* Molecular Cell Biology. (2000). at <http://www.ncbi.nlm.nih.gov/books/NBK21475/>

183. Hristovski, K. D., Westerhoff, P. K. & Posner, J. D. Octanol-water distribution of engineered nanomaterials. *J. Environ. Sci. Health. A. Tox. Hazard. Subst. Environ. Eng.***46,** 636–47 (2011).

184. Borgå, K. *et al.* Trophic magnification factors: Considerations of ecology, ecosystems, and study design. *Integr. Environ. Assess. Manag.***8,** 64–84 (2012).

185. Leo, A., Hansch, C. & Elkins, D. PARTITION COEFFICIENTS AND THEIR USES. (1971).

186. Oecd. GUIDANCE MANUAL FOR THE TESTING OF MANUFACTURED NANOMATERIALS: OECD's SPONSORSHIP PROGRAMME; FIRST REVISION. *Development* 1–92 (2010).

187. Westerhoff, P. & Nowack, B. Searching for global descriptors of engineered nanomaterial fate and transport in the environment. *Acc. Chem. Res.***46,** 844–853 (2013).

188. Nel, A. E. *et al.* Understanding biophysicochemical interactions at the nano-bio interface. *Nat. Mater.***8,** 543–557 (2009).

189. Oecd. Report of the Oecd Expert Meeting on the Physical Chemical Properties of Manufactured Nanomaterials and Test Guidelines. 56 (2014). at <http://www.oecd.org/officialdocuments/displaydocument/?cote=env/jm/mono(2014)15&doclanguage=en>